Interner Bericht
DESY F41-70/2
April 1970

Modulation Spectroscopy of Semiconductors

Manuel Cardona

DESY-Bibliothek
15. Apr. 19..

Modulation Spectroscopy of Semiconductors[+]

Manuel Cardona[++]

Deutsches Elektronen-Synchrotron, Hamburg

[+] Paper to be presented at the meeting of the German Physical Society, Freudenstadt, April 4 - 11, 1970

[++] John Simon Guggenheim Memorial Foundation fellow, on sabbatical leave from Brown University, Providence, Rhode Island, USA

INTRODUCTION

The idea underlying modulation spectroscopy is a very general principle of experimental physics. Instead of directly measuring an optical spectrum, the derivative of this spectrum with respect to some parameter is measured. This can be easily accomplished by applying the parameter as a small perturbation in a periodic fashion and measuring the corresponding change in the optical properties with phase sensitive detection (i. e. with a lock-in amplifier). Structure in the conventional optical spectra is considerably enhanced in the derivative spectra and flat structureless backgrounds are eliminated. Weak structure superimposed on a large background is sometimes difficult to resolve due to statistical noise of the background. Its resolution becomes easier in a modulation measurement since the structureless background is eliminated.

The modulation techniques can be classified into two categories: internal and external. In the internal modulation techniques, a parameter of the monochromatic optical beam, such as the wavelength or the degree of polarization, is modulated. In the external techniques an independent modulation parameter (e. g. a stress, an electric field, etc.) is applied to the sample. The internal techniques are simpler from the point of view of the theoretical interpretation of the results, since their theory involves only the optical properties of an unpertubed solid. The interpretation of an external modulation spectrum involves the rather formidable problem of the theory of the optical properties in the presence of a perturbation. Fortunately, one may sometimes make considerable progress without completely solving this problem, especially if one is only

interested in the position and selection rules of sharp structure and not in the detailed line shapes. External modulation is simpler than internal modulation from the experimental point of view. In an internal modulation experiment the spectral distribution of the intensity and polarization properties of the incident beam produces spurious signals which must be corrected for. Such correction requires the use of complicated and not too accurate double beam systems.

The external modulation methods can be subdivided into two categories according to the nature of the perturbation. Some perturbations (e.g. stress) preserve the translational symmetry of the solid. In this case the line shape of structure associated with energy gaps is very similar to that observed in a wavelength modulation spectrum: the stress simply shifts the energy gap, which is in turn equivalent to a shift in the wavelength scale. Other perturbations partially destroy the translational invariance (e. g. electric field, magnetic field) giving rise to complicated line shapes not directly related to the wavelength derivative of the conventional spectrum. Some external parameters (e. g. uniaxial stress, electric field, magnetic field) may lower the symmetry of the solid and hence introduce additional anisotropy in the corresponding modulation spectra. These anisotropies are usually very helpful in the idenfication of the symmetry of the transitions responsible for the observed structure.

While optical modulation had been occasionally used previously[1,2], the enormous amount of activity in the field within the past few years started with the discovery of electroreflectance (modulation of the reflectivity by an electric field) by Seraphin and Hess[3]. As shown by these authors, modulation techniques are particularly useful for detecting weak structure in the reflection spectrum above the fundamental absorption edge. After the original work of Seraphin and Hess, the techniques of stress modulation (piezoreflectance, piezoabsorption)[4], temperature modulation (thermoreflectance, thermoabsorption)[5], modulation by an external light beam (photoreflectance)[6] and others, appeared in quick succession. Electric field modulation, however, has remained to this date the most popular technique because of its experimental simplicity and the sharpness of the spectra obtained. These modulation techniques have also become very useful for studying the effect on the optical properties of static perturbations such as alloying[7], large stresses (piezo-electroreflectance), and strong magnetic fields (magneto-piezoreflectance[8], magneto-electroreflectance[9]).

A number of extensive review articles covering the work on modulation spectroscopy published up to 1968 have been written[10-13]. We shall confine ourselves in this paper to the discussion of work published after the closing date of Ref. 12, Dec. 1967. The present work emphasizes the application of existing modulation techniques to new problems, the development of new modulation techniques, and the theoretical understanding of the line shapes obtained in modulation spectroscopy, especially in electroreflectance.

ELECTROREFLECTANCE

a) Experimental Techniques

As is well known, electroreflectance measurements in conducting samples must be performed with the modulating field confined to the space-charge region near the surface. Two main techniques are used: the dry sandwich method[3] and the electrolyte technique[14]. A very convenient type of dry sandwich has been recently described[15,16]. The insulating layer is a thin ($\sim$ 200 Å) Al_2O_3 film prepared by evaporation with an electron gun. The modulating electrode is a semitransparent nickel film vacuum-deposited on the Al_2O_3 layer. Surface fields as high as 10^6 V/cm are easily obtained with this method, which can be used at low temperatures and for photon energies as high as 6.5 eV.

Considerable effort has been devoted recently to performing both dry sandwich[17,18] and electrolyte measurements[19] under well-controlled conditions and with simultaneous auxiliary measurements of the surface fields. The purpose of this work was a quantitative comparison of the line shapes with existing theories of the electro-optic effect. It was pointed out by Hamakawa et al.[20] that it is possible to obtain quantitatively reproducible results with the electrolyte technique by using an electrolyte buffered to a given pH and gettered with crushed germanium. Under these conditions it is usually possible to vary the quiescent surface potential by varying the dc bias (unless these precautions are taken, the quiescent surface potential is often clamped and cannot be varied). This technique permits modulation of the surface field between zero (flat bands) and the desired value: a convenient feature for comparison of the

experimental results with the theory. It is desirable to use square waves for the modulation so as to avoid unnecessary field averaging which would complicate comparison with the results, strongly non-linear in the field, obtained theoretically.

A number of methods can be used for the determination of the surface field. Seraphin[21] used standard field-effect conductance measurements, but this method suffers from the uncertainties associated with our knowledge of the surface mobility. In order to remedy this situation Frova and Aspnes[18] used simultaneous measurements of field effect conductance and Hall effect: the changes in the conductivity and in the Hall effect produced by the modulating electric field were measured with a dry sandwich field effect package. This method permits simultaneous determination of two variables, the surface mobility and the surface carrier concentration, from which the surface field can be obtained.

It was found that for intrinsic germanium treated appropriately (electropolishing on soft cloth) the quiescent surface potential adjusts itself so as to give nearly flat bands for the maximum negative voltage applied to the modulating electrode. This feature makes external adjustment of the modulating voltage so as to reach flat bands (zero surface field) in one of the modulating half cycles unnecessary.

Aspnes and Frova have recently performed extremely careful electrolytic electroreflectance measurements on intrinsic germanium with simultaneous measurements of the fast photovoltage and of surface layer capacitance to determine the flat band position and the surface carrier concentration[19].

The experimental setup is shown in Fig. 1. Other than the conventional electronics for the measurement of electroreflectance, this setup contains a potentiostat for controlling the quiescent surface potential of the sample and applying the modulating voltage and a capacitive voltage divider with a high-frequency probe to determine the capacitance at the germanium-electrolyte interface. In addition to the components shown in Fig. 1, a 1 mW laser with a phased-locked mechanical chopper was used to perform the fast photovoltage measurements.

The modulating voltage is applied to the platinum electrode by the potentiostat composed of two operational amplifiers: a buffer amplifier, receiving the signal from the calomel electrode, and a driving amplifier, feeding into the platinum electrode. Variable time response is provided by an RC feedback circuit. The high-frequency capacitive divider is composed of the capacitor C and the platinum probe grid, completed by the semiconductor-electrolyte interface. It permits capacitance measurements within a microsecond time interval by measuring on the scope the signal produced by the square-wave generator as sensed by the probe. The same scope and probe is used to measure the fast photovoltage produced by the laser.

The fast photovoltage is the sum of the change in Dember potential and the surface barrier potential ϕ_{so}. It has been shown by Aspnes that it vanishes whenever

$$\phi_{so} = k\,T \ln \frac{\mu_n}{\mu_p}\,, \tag{1}$$

where μ_n and μ_p are electron and hole mobilities respectively. Thus if one determines the surface potential which produces zero photovoltage, one has determined the position of the flat band since ϕ_{so} is referred to the flat band. The determination of the surface potential which gives a minimum in the interface capacitance yields, once the flat band position is known, the flat-band carrier concentration at the surface. From these parameters the surface field is easily found.

The non-uniform nature of the surface field must be taken into account when the experimental results are compared with the uniform field theory. This spatial non-uniformity produces a smearing of the slowly decaying theoretical Franz-Keldysh oscillations. Aspnes and Frova[22] have considered theoretically the problem of the reflection of electromagnetic waves at a surface with a normal gradient in the optical constants, such as that produced by the non-uniform field of space charge layers. For a field with a small penetration depth (compared to that of light) the results are similar to those predicted by the uniform field theory (with the appropriate field averaging) except that $\Delta\varepsilon_r$ and $\Delta\varepsilon_i$ must be replaced by a suitable linear combination.

The Franz-Keldysh oscillations contain information about effective masses and it is, therefore, of interest to perform measurements with uniform fields so as to obtain as many oscillatons as possible. For low fields the penetration depth (and thus the field homogenity) is largest with intrinsic samples. However, Handler et al.[23] have pointed out that for larger fields

their homogenity, as measured by $\left|\frac{1}{\mathcal{E}}\ \frac{d\mathcal{E}}{dz}\right|$ at the surface, may be better with extrinsic samples. Figure 2 shows the calculated values $\left|\frac{1}{\mathcal{E}}\ \frac{d\mathcal{E}}{dz}\right|$ as a function of surface field for several germanium samples of different dopings: the dopings are represented by the standard parameter $u_B=(E_F-E_{FI})/kT$, where E_F-E_{FI} is the Fermi energy (E_F) referred to that of intrinsic material (E_{FI}). Appropriate choice of the doping which gives the smallest homogeneity for a given surface field, enabled Handler et al.[23] to see a large number of oscillations at the E_o and $E_o+\Delta_o$ edges of germanium, even at room temperature.

Besides the longitudinal field-effect configuration discussed above, measurements can also be performed with transverse fields provided the sample resistivity is high ($\rho \gtrsim 10^8$ ohm-cm). Such measurements have the advantage of the field uniformity and the extra optical anisotropy associated with the transverse field: even for optically isotropic samples measurements with light polarized with $\underset{\sim}{E}$ parallel to the modulating field $\underset{\sim}{\mathcal{E}}$ should yield results different from those for $\underset{\sim}{E}$ perpendicular to $\underset{\sim}{\mathcal{E}}$. The doping of semiconductors with impurities which yield levels near the middle of the gap is known to produce, by compensation of residual shallow levels, samples of high resistivity at low temperatures. Hence transverse field measurements become possible with gold-doped silicon[24]. The field is applied with two gold electrodes evaporated onto the reflecting surface with a $\sim$ 0.5 mm field gap between them. The light is reflected on the field gap. Using a similar technique, Fischer et al.[25] were able to measure transverse electroreflectance in germanium. The high resistivity samples (10^8 ohm-cm at 77° K) were prepared from high-purity n-type material ($\sim 10^{13}$ donors/cm^3) by irradiation with cobalt-60 γ-rays: a dose of 10^{18} cm^{-3} is known to produce about 10^{15} cm^{-3} deep-lying acceptor levels.

b) Theory

Most of the recent theoretical activity concerning effects of electric fields on the optical constants has dealt with the exciton problem[26-30]. The effect of electric field on one-electron interband absorption is well understood, at least whenever the optical structure is due to well-defined, isolated critical points[31]. The exciton interaction is known to modify, sometimes rather drastically, structure due to interband critical points in the absence of an external field: for M_o and M_3 critical points this problem can be approximately treated by solving the corresponding hydrogenic Schrödinger equation with an attractive (M_o critical points) or repulsive (M_3 critical points) Coulomb potential. The attractive Coulomb potential enhances optical structure (M_o critical point), while the repulsive one suppresses it (M_3 critical point).

The singularity at infinity of the potential of a uniform electric field prevents its treatment by perturbation thecry, even in the case of small fields: The Schrödinger effective-mass equation for the relative motion of electron and hole in the presence of external field and Coulomb interaction must be solved. This equation has, at least for isotropic masses, an axis of symmetry of revolution (parallel to the applied field) and hence its solution can be reduced to that of a two-dimensional equation. This equation can be separated into two one-dimensional equations with the use of parabolic coordinates. These equations must be integrated numerically. One of them has discrete eigenvalues while the other has a continuous eigenvalue spectrum because of the fact that the external potential becomes $-\infty$ at large distances.

The continuous nature of the eigenvalue spectrum presents some difficulties when numerical methods of solving the equations are used. The normalization condition is:

$$\int \chi^{*}_{E_1}(\zeta)\, \chi_{E_2}(\zeta)\, d\zeta = \delta(E_1 - E_2) \qquad (2)$$

The δ function is obviously difficult to handle numerically. In order to avoid the numerical solution Duke and Alferieff[32] replaced the potential in the effective mass equation, sum of the Coulomb and the external field potentials, by a pure Coulomb potential near $\rho = 0$ (ρ = distance between electron and hole) and the pure external potential for large values of ρ; the solution of both problems are then matched at the cut-off surface. Since this separation must be made in parabolic coordinates, the cut-off surface for switching from one potential to another is not simply ρ = constant and thus it does not have a clear physical meaning. As we shall see later, some of the results of this calculation, such as a <u>decrease</u> in the exciton binding energy with <u>increasing</u> field, even for small fields, contradict the results obtained by numerical solution with the exact potential. These results seem to depend rather critically on the details of the potential at the maximum of the barrier, where the transition from Coulomb-like to uniform-field-like takes place.

Ralph[26] solved the problem of the normalization of the continuous wave functions by imposing its vanishing at a large, fixed value of the argument. This boundary condition, which vaguely corresponds to assuming a crystal of finite size, makes the eigenstates discrete and thus removes the normalization problems since the wave functions can then be normalized

in the standard manner to a Kronecker-δ. Blossey[29] proposed a different, but equivalent approach: he showed that the normalization integral of Eq. (2) can be obtained simply from the assymptotic behavior of $\chi_E(\xi)$ without having to use the complete numerical solutions. The result of Ralph's work is shown in Fig. 3, for various values of the reduced field f (f is the field in units of exciton Rydbergs per exciton Bohr radius). The n=2 exciton disappears for values of $f \approx 0.2$ while the n=1 exciton remains up to $f \approx 1$. Similar results have been obtained by Blossey, who considered also the case of an M_3 edge (effective repulsive Coulomb potential). The results for a M_3 edge, shown in Fig. 4, indicate the smoothing out of the square-root singularity near M_3 by the Coulomb interaction and the appearance of Franz-Keldysh-like oscillations below the singularity for $f \neq 0$.

Dow and Redfield[28] have discussed the exciton behaviour for $f \neq 0$ in the energy region below an M_o edge. They find numerically the following result valid over a very wide range of ϵ_i (several decades):

$$\epsilon_i \sim \exp\left[C_o (E_o - E) / f\right] \tag{4}$$

where E_o is the energy gap and C_o a negative constant. This result contradicts the predictions of Duke and Alferieff[32], who found a similar expression but with the three-halves power of $(E_o - E)$ in the exponent.

A common criticism to all the work discussed above is that it neglects lifetime broadening of the excitons, i. e. it assumes infinitely sharp discrete excitons for $f = 0$. Lifetime broadening is of the essence for describing the experimental results: the broadening induced by the

electric field is usually smaller than this lifetime broadening. No satisfactory description of the electrooptic effect of an exciton in the presence of broadening has been given to date. The convolution approach of Rees[33,34] should be valid in the continuum region but probably not for the discrete states. This approach is based on the use of the convolution or spectral broadening expression:

$$\varepsilon_i(\omega,\mathcal{E}) = \frac{1}{\omega^2} \int_{-\infty}^{+\infty} d\omega' \; \omega'^2 \; \varepsilon_i(\omega',0) \; \frac{1}{\Omega} \, Ai\left(\frac{\omega' - \omega}{\Omega}\right) \tag{5}$$

with Ai the Airy function and $\Omega = (\mathcal{E}^2/8\,\mu)^{1/3}$ (μ is the reduced mass). The limits of validity of Eq. (5) are not very clear; it would be interesting to check numerically whether it can account for the results of Fig. 3.

The replacement of the Coulomb exciton interaction by a Koster-Slater contact interaction (δ-function of the electron-hole separation) has been useful to provide qualitative information about the excitonic behavior of general interband critical points. However one must treat this approximation with a great deal of care: it gives <u>at most</u> one bound state below an M_o critical point and thus it fails to predict the detailed behavior of the hydrogenic excitons. In this approximation the behavior of the complex dielectric constant near a critical point is given by:

$$\varepsilon(\omega) = \frac{1}{1 + g\,F(\omega)} \, \varepsilon^{o}(\omega) \tag{6}$$

where $\varepsilon^{o}(\omega)$ is the dielectric constant in the absence of exciton interaction, g the interaction constant ($g < 0$) and $F(\omega)$ a complex function related to the optical density of states $N_d(\omega)$ through:

$$F(\omega) = -\int_{-\infty}^{+\infty} \frac{1}{\omega - \omega' + i\eta} N_d(\omega')\, d\omega' \qquad (7)$$

the density of states $N_d(\omega)$ is related to the imaginary part of $\varepsilon^{o}(\omega)$ and the average matrix element for the transitions P^2 through:

$$\varepsilon_i^{o}(\omega) = \frac{4\pi^2}{\omega^2} P^2 N_d(\omega) . \qquad (8)$$

Penchina et al.[30] have treated the problem of the effect of a uniform electric field on the Koster-Slater exciton discussed above. Their calculations, restricted to the case of one-dimensional electrons, yield the same result as Eq. (6), with $\varepsilon^{o}(\omega)$ replaced by $\varepsilon^{o}(\omega,\xi)$, the inter-band (Franz-Keldysh) dielectric constant in the presence of the uniform field but in the absence of the Coulomb interaction.

This simple result, probably also valid for three-dimensional bands, can be used to explain the effect of exciton interaction on the electroreflectance line shapes[35].

c) Results

As mentioned earlier, Aspnes and Frova have performed simultaneous electroreflectance measurements and surface field measurements on germanium with both the dry sandwich[18] and the electrolyte technique[19]. The results obtained with both techniques are essentially the same. Figure 5 shows the E_o peak obtained by the electrolytic method for various values of the surface field (surface potential) on a nearly intrinsic sample: a noticeable change of shape occurs as one goes to high fields. Similar changes in line shape with field can be observed for most space-charge barrier electroreflectance measurements. They have been attributed to a transition from the low field, long penetration depth regime (the field is uniform over the penetration depth of the light) to the high field, short penetration depth, in which the field varies drastically within the penetration depth of the light. In the short penetration depth regime the eletroreflectance signal is[22]:

$$\frac{\Delta R}{R} = \alpha < \Delta\varepsilon_r > + \beta < \Delta\varepsilon_i > \qquad (9)$$

where α and β are the differential coefficients of Seraphin and Bottka, and $< \Delta\varepsilon >$ is defined as:

$$< \Delta\varepsilon > = < \Delta\varepsilon_r > + < \Delta\varepsilon_i > = - 2\, ik \int_{-\infty}^{o} \Delta\varepsilon(z')\, e^{-2ikz'}\, dz' \qquad (10)$$

where $\Delta\varepsilon(z')$ is the result of the uniform field theory with the field at the point z', and z the coordinate normal to the surface, assumed

to occur at $z = 0$. k is the unperturbed propagation constant. For a very short field penetration depth, Eq. (10) can be written as:

$$< \Delta\varepsilon > = - 2 ik \int_{-\infty}^{o} \Delta\varepsilon(z') \, dz' \qquad (11)$$

The integral in Eq. (11) represents the average change in the dielectric constant, while the coefficient in front produces a mixing in the real and the imaginary parts.

Figure 6 shows the results of a calculation of $< \Delta\varepsilon >$[22] for intrinsic germanium for various values of the surface field. The change in shape exhibited by the experiments of Fig. 5 can be easily understood by refering to Fig. 6: near E_o $\beta \simeq 0$ and $\Delta R/R \propto < \Delta\varepsilon_r >$. For small fields ($\mathcal{E}_s \lesssim 5$ kV/cm) a strong negative peak II is seen, followed by a positive one (III). Another weak negative peak is seen above III. This is the behavior shown by the upper curves $< \Delta\varepsilon_r >$ of Fig. 6: the oscillations at higher energies may be depressed by scattering. At the highest fields Fig. 5 shows a growth of peak I at the expense of peak III, as expected from the calculations of Fig. 6. This theoretical and experimental behavior is exhibited explicited in Fig. 7, where the strengths of peaks I, II and III are plotted as a function of surface field. The field for crossover in the strengths of peaks I and III observed experimentally agrees satisfactorily with that calculated, especially when one considers that broadening and exciton effects have been neglected. The position of peaks I, II and III shifts slightly in going from the low field to the high field regime, as shown in Fig. 8. This behavior is also predicted by the calculations based on the spatial dependence of $\Delta\varepsilon$.

The variation of electroreflectance structure with an applied uniform field has been studied for the E_o peak of GaAs in the transverse field configuration[24]. The results have been compared with calculations of the Franz-Keldysh effect with inclusion of Lorentzian broadening[31]. The strength of the signal, proportional to $\mathcal{E}^{1/3}$ in the unbroadened theory, becomes proportional to $\mathcal{E}^2$ at fields such that:

$$\theta = \left(\frac{\mathcal{E}^2}{2\mu}\right)^{1/3} << \Gamma , \qquad (12)$$

where Γ is the broadening parameter. Thus the tensorial dependence on $\mathcal{E}$ is recovered as a result of broadening. For $\theta \approx \Gamma$ the peak strength becomes linear, since it should be roughly proportional to the area under the main unbroadened peak (height $\propto \mathcal{E}^{1/3}$, width $\propto \mathcal{E}^{2/3}$). At higher fields the unbroadened $\mathcal{E}^{1/3}$ dependence is recovered. This is illustrated in Fig. 9, where we have shown the peak-to-peak strength observed for the E_o structure of GaAs and fitted it, by choice of the broadening parameter $\Gamma \simeq 11$ meV, to the theoretical peak-to-peak strength obtained from the broadened electrooptic function $G(x, \Gamma)$.

Figure 10 shows the results of transverse electroreflectance measurements performed by Fischer et al.[25] for the E_1, $E_1+\Delta_1$ and E_2 peaks of germanium. The polarization dependence observed for the E_1 and $E_1+\Delta_1$ peaks with a (111) field (none is observed for a (001) field) confirms the Λ symmetry of the corresponding transitions. The magnitude and sign of this anisotropy is close to what one would expect for valleys with a large longitudinal mass (only the transverse components of the field produces electrooptic effect). The lack of polarization effects at E_2

for $\mathcal{E}||(111)$ indicates the absence of (111) symmetry in the corresponding transitions. The polarization effects are strong for $\mathcal{E}||(001)$. The large differences in the spectra for $\mathcal{E}||(111)$ and for $\mathcal{E}||(001)$ suggest either a different dominant critical point for each configuration or a different electroreflectance mechanism. For instance, the structure for $\mathcal{E}||(001)$ could be due predominantly to energy shifts while the broader one for $\mathcal{E}||(111)$ could be due to changes in matrix elements. The clarification of this matters constitutes a rather interesting problem.

Handler et al.[23] have performed electrolytic electroreflectance measurements on germanium choosing the doping so as to provide a very uniform field over the penetration depth of the light. The results obtained at room temperature for the E_o and $E_o+\Delta_o$ edges as shown in Fig. 11. The dashed curves in the semilog plots are theoretical curves obtained from the Lorenzian-broadened expressions for the Franz-Keldysh effect. Because of the existence of two different types of holes, light and heavy, two sets of Franz-Keldysh oscillations must be considered. Their "periods" differ little inspite of the difference in reduced masses (0.38 for heavy holes, 0.022 for light holes) because the mass enters in the "periods" of the oscillations as $\mu^{1/3}$. The beating seen in Fig. 11 is due to this small difference in $\mu^{1/3}$ between light and heavy hole bands. The values of the broadening parameter required for the theoretical fit of Fig. 11 are remarkably small: 3 meV for E_o and 9 meV for $E_o+\Delta_o$.

The main structure in the electroreflectance spectra of zincblende materials is composed of the E_o peak, the E_1 peak (and its spin-orbit mate $E_1+\Delta_1$) and the E_2 peak. Additional weaker structures, such as the E_o' peaks, between $E_1+\Delta_1$ and E_2, and the E_1' peaks, above E_2, are known to exist. Both E_o' and E_1' exhibit spin-orbit splitting, but the

details of this splitting are not thoroughly understood: that of E_o' is related to the splitting of the upper valence band and the second lowest conduction band near Γ_1 while that of E_1' is related to the splittings of the same bands at L. Recent work by Glosser et al.[15] has contributed significantly to our understanding of the E_o' structure, shown in fig. 12 together with the E_1, $E_1+\Delta_1$ peaks. These authors observed that the A-A' components of E_o' disappear for p-type surfaces and thus they suggested they are related to transitions of conduction electrons from the lowest to the second lowest conduction band. The peaks labeled B and B', higher than A-A' by about the E_o gap, are the corresponding valence-to-conduction-band transitions; structure with a behavior similar to the A peak of Fig. 12 has been observed by Parsons et al. for GaSb[16]. These authors have reported very detailed structure corresponding to E_o' and E_1' for GaAs, GaSb, and Ge. The position of the observed peaks is presented in Table I, together with that of structure observed recently in wavelength derivative spectroscopy by Zucca and Shen[36], and the energy of the peaks in the derivative spectra calculated from the band structure of the materials[37].

Glosser and Seraphin have reported a rather curious reversal of the electroreflectance structure of InSb (dry sandwich, Al_2O_3-Ni-type electrode) after illumination with light of photon energy higher than 2.7 eV.[38] This reversal persists after the light is switched off; recovery times are of the order of minutes at room temperature and days at 77° K. The phenomenon was interpreted as due to internal photoemission from the InSb to trapping states in the Al_2O_3 dielectric layer.

The possibility of observing electroreflectance structure due to shallow impurity states below the E_o gap has been known for sometime. A detailed study of such structure in GaAs with controlled dopings (Mn, Si, Cd) has been presented by Williams[39].

This discussion of electroreflectance has been limited so far to electro-optic effects <u>even</u> in the electric field, such as the Franz-Keldysh effect. Zincblende-type materials lack an inversion symmetry and thus should exhibit a linear electrooptic effect which should be measureable at the modulating frequence, even in the absence of dc bias or surface field. Such an effect has been observed for CuCl by Daunois et al.[40] and by Mohler[41]. Figure 13 shows the reflection peaks E_o and $E_o+\Delta_o$ of CuCl, the quadratic and the linear electroreflectance signal at those peaks. Both peaks have the same sign for the quadratic effect, as expected from the theory of the electric effect of excitons. The sign of the observed structure corresponds to an increase in the binding energy with field, as given by the theory. The linear electrooptic effect, observed for a field parallel to a cubic axis, ($\mathcal{E} \parallel C_4$) is strong only for light polarized with $E \perp \mathcal{E}$; E_o and $E_o+\Delta_o$ have opposite signs, thus suggesting a repulsion of both excitonic states produced by the electric field. The observed selection rule can be easily understood: the electric field along the z direction can only couple the x and y components of the Γ_{15} excitons, thus giving a signal only for E parallel to either x or y ($E \perp C_4$).

We have so far discussed work on materials of the germanium family. Electroreflectance and electrotransmission work also has been performed

for other types of materials such as Cu_2O[42,43], HgI_2[44,45], and Se[47]. Of special interest is the electroabsorption work performed for the ground state of the exciton in Cu_2O. This is a dipole forbidden (even parity) exciton which becomes dipole allowed in the presence of the modulating field[42]. Recent electroabsorption work by Deiss et al.[43] with oriented samples has considered the selection rules associated with the field-induced dipole transitions. We show in Fig. 14 the electrotransmission of Cu_2O for a modulating field $\mathcal{E}\|(001)$ and with light propagated along (110) $(q\|(110))$, for both principal directions of polarization ($E\|(001)$ and $E\|(1\bar{1}0)$). The n=1 direct line and two indirect (phonon absorption and phonon emission) satellites appear in this figure. The n=1 line has an s-like shape for $E\|(001)$, while its shape is that expected for the field-induced exciton for $E\|(1\bar{1}0)$. The s-shaped line can be explained as a superposition of the field induced line and the field shifted quadrupole line: the quadrupole line is allowed for $E\|(001)$ but not for $E\|(1\bar{1}0)$ (for $q\|(110)$). The shape of the field-shifted quadrupole line should be essentially the derivative of the field induced dipole line and hence the line shape for $E\|(001)$ is explained. It is interesting to note that the sign of the field-shifted quadrupole contribution to the n=1 line and that of the indirect peaks corresponds to a field induced increase in the exciton binding energy.

Recent interest in the properties of amorphous materials suggests the study of their spectra by means of modulation techniques. Piller et al.[46] have reported the electroreflectance spectra of thin germanium films

deposited at various substrate temperature T_s. Films deposited with $T_s \lesssim 200^{\circ}$ C are amorphous while for $T_s \gtrsim 200^{\circ}$ C they are crystalline. The spectra of the E_o, $E_o+\Delta_o$ peaks are seen for both crystalline and amorphous materials, although they are shifted to lower energies in the amorphous case. Other peaks, such as E_1, $E_1+\Delta_1$ and E_2 are only seen for crystalline films (see Fig. 15).

Similar measurements have been performed by Weiser and Stuke for crystalline and amorphous selenium[47]. They find the lowest-energy peak (equivalent perhaps to E_o of germanium) in both cases while structure at higher energies is only present for crystalline films.

PHOTOREFLECTANCE

a) Experimental Techniques

In the original photoreflectance experiment of Wang et al.[6] the reflectivity of a sample was modulated by means of a strong conventional lamp focused onto the sample. This light was chopped at a frequency of 13 Hz. The monochromatic measuring light was focused on the same spot. Results were reported for Ge, CdS and ZnTe.

The main problem in a photoreflectance measurement is to eliminate stray and diffuse-reflected light from the modulating source which may reach the detector. Such light may produce a spurious signal many times larger than the photoreflectance signal and usually limits the sensitivity of the technique. Photoluminescence produced by the modulating light has been usually found to give spurious signals much smaller than photoreflectance, except at very low temperatures[48]. The elimination of such spurious signals can be facilited by using a monochromatic laser as modulating source and suitable filters to prevent the spurious laser light from reaching the detector. Excellent results have been obtained with a He-Ne laser[48-51] operating at 6328 Å : a 2-64 Corning filter can be used to eliminate spurious light. Modulation with a laser also has the advantage of added simplicity in focusing the radiation on the sample. Small 1 mW lasers are sufficient to study photoreflectance in most cases: the use of more powerful lasers does not represent a significant increase in the sensitivity since the photoreflectance signal varies approximately like the 1/3 power of the modulating intensity, while the spurious scattered light is linear. A number of methods have been used to enhance the rejection of

spurious signal. If the modulating light is linearly polarized (as is the case with most lasers) considerable rejection can be accomplished by linearly polarizing the probing light perpendicularly to the modulating light or by placing a polarizer in front of the detector crossed with the modulating light[50]. The modulation of the probing beam at a frequency Ω_1 different from that of the modulating light Ω_2 has also been suggested: the photoreflectance signal appears at the frequences $\Omega_1 \pm \Omega_2$ while the spurious signal due to scattered radiation appears only at Ω_1 (and harmonics)[52]. It is also possible to reduce the amount of spurious signal by using a second detector placed so as to receive only spurious signal. The signals from both detectors are then sent to a difference amplifier; the gains are adjusted so as to eliminate the spurious signal[48].

As will be discussed in the next subsection, the phenomenon of photoreflectance with a modulating source of wavelength smaller than the fundamental edge is related to the photoexcitation of electron-hole pairs by the modulating light. The associated temperature is usually too small ($\sim 0.01^{\circ}$ K according to Nahory and Shay[49]) to produce significant modulation of the reflectivity (thermoreflectance). An admixture of the effects of pair production and temperature modulation has been observed by Nilsson[53] when using a mercury arc, presumably with a considerable infrared component, as the modulating source. The thermoreflectance component exhibits a time lag with respect to the modulating light and it becomes smaller as the frequency is increased. The absence of such time lag and frequency dependence is an indication of the absence of the thermoreflectance in the photoreflectance signal.

The dependence of the phenomenon on the density of pairs injected by the modulating light introduces an additional sample quality factor: the lifetime of such pairs near the injection surface. Samples which give strong signals with other modulation techniques are sometimes useless for photoreflectance work: their injected carrier lifetime is too small. As discussed in the next subsection, the nature of the photoreflectance signals is usually the same as that of the electroreflectance signals. The photoreflectance technique, however, has an inherent simplicity with respect to electroreflectance since it does not require electrodes and insulating layers on the reflecting surface. Such layers and electrodes are the source of wavelength and temperature limitations in the surface barrier electroreflectance technique. Photoreflectance signals, however, are typically an order of magnitude smaller than those obtained in electroreflectance. Also, the problem of scattered light, which appears in photoreflectance, is not present in electroreflectance.

b) Photoreflectance Mechanisms and Results

Most of the recent activity in the field of photoreflectance has revolved around the problem of the mechanism responsible for the observed signals. This has resulted in theoretical work[54,55] and in a number of experiments especially designed to clarify the question of the photoreflectance mechanism[49-51]. Three mechanisms have been proposed, all related to the production of electron-hole pairs by the modulating light:

i) Modulation of the field in the surface barrier by the photoinjected pairs[6]

ii) Burstein shift in absorption edges due to the filling of the bands by the photoinjected carriers[54]

iii) Screening of the exciton interaction by the photoinjected pairs[55]

The temperature modulation produced by the modulating light is negligible at high enough chopping frequencies (a few hundred Hz), as discussed in the previous subsection. All of the three mechanisms given above may be operative, and even dominant, depending on the circumstances. Mechanism (i) (≡ electroreflectance) seems to be the most general one.

The line shapes expected for these three mechanisms are considerably different. In mechanism (i) the injected carriers usually decrease (screen) the surface field (except for nearly intrinsic samples[51]) and hence the optical structure is sharper when the modulating light is on. The main

peak in ΔR $(= R \text{ (light on)} - R \text{ (light off)})$ is expected to be positive. With mechanism (ii) and (iii) the modulating light (i. e. the injected carriers) decreases the sharpness of the optical structure or shifts it to higher energies ; the dominant peak in ΔR is expected to be negative.

Mechanism (ii) can only be operative for optical transitions in which either the top of the valence band or the bottom of the conduction band is involved: the lifetime of carriers at the lower valence band or at higher conduction band states is too short to produce any significant filling. This mechanism can thus be operative at the lowest direct gap of diamond-, zincblende- and wurtzite-type materials but not at the higher-energy transitions. Thus the strong signals observed at the E_1 and $E_1+\Delta_1$ peaks of Ge and GaAs cannot be due to mechanism (ii).

Mechanism (ii) can also be ruled out at the lowest direct edge of InSb (E_o). Shay et al.[56] have measured the photoreflectance of this material in the neighborhood of E_o, in the presence of a strong magnetic field (magnetophotoreflectance) and have observed the rich Landau level structure shown in Fig. 16. Because of the splitting between Landau subbands, only the lowest peak in Fig. 16 should be affected by band population filling (Burstein shift): the relative intensities of the many peaks in Fig. 16 are quite similar to those observed in magnetoelectroreflectance[57]. One must therefore conclude that mechanism (ii) is not important at the E_o edge of InSb. The strongest support for mechanism (i)

comes from the observation of changes in the photoreflectance upon variation of the quiescent (i. e. for zero ilumination) surface field[49-51]. This variation can be easily accomplished by the electrolyte technique[14]. Aspnes[51] has performed careful measurements of photoreflectance on a Ge sample immersed in an electrolyte, as a function of sample bias. He performed simultaneous measurements of the surface potential ϕ_S, and thus the surface field $\mathcal{E}_s$, and was able to show that the signal vanishes for $\phi_s = 0$. His results for the E_o peak of Ge are shown in Fig. 17 for several values of $\mathcal{E}_s$. It is interesting to note that, contrary to electroreflectance, the sign of the signal is the same for both signs of $\mathcal{E}_s$. The signal vanishes within the experimental error for $\mathcal{E}_s = 0$, as required by (and only by) mechanism (i). The width of the oscillations increases with $\mathcal{E}_s$, in agreement with the Franz-Keldysh theory of electroreflectance. The line shape observed for $\mathcal{E}_s = 1.0$ is also in qualitative agreement with that predicted by the Franz-Keldysh theory; at higher values of $\mathcal{E}_s$ the line shape changes in qualitative agreement with the inhomogenous field theory of Aspnes and Frova[22] (see Fig. 6).

The sign of the signal in Fig. 17 indicates that the modulating light increases the surface field (the leading peak in ΔR at 0.795 eV is negative). This is not the usual sign found in photoreflectance. This fact is due to the nearly intrinsic character of the sample and the absence of surface states with Aspnes' electrolyte method: an increase in the electron-hole pair concentration n_I produces a decrease in the Debye screening length $\mathcal{L}$:[12]

$$\mathcal{L} = \left(\frac{\varepsilon_o \, kT}{8 \pi \, e2 \, N_I} \right)^{1/2} \qquad (13)$$

(ε_o is the static dielectric constant, N_I the intrinsic electron concentration) with a resulting increase in the surface field for a constant value of ϕ_s.

Shay[58] has done a systematic study of photoreflectance at the E_o edge of ultrapure epitaxial GaAs as a function of doping, temperature and modulating laser intensity. The spectra obtained for the purest samples available ($N_d = 1.65 \times 10^{13}$ cm^{-3}) for two laser intensities which differ by a factor of 100 are shown in Fig. 18. At low modulating intensity the sign of the signal is opposite to that in Fig. 17, (the leading peak at 1.43 eV is positive) thus indicating a decrease of the surface field with light intensity. This fact was interpreted by Shay as due to trapping of the injected holes at surface states (apparently absent in Aspnes' experiment). The trapped holes screen (and thus decrease) the electric field. With this model it is possible to explain qualitatively the observed increase in the period and the amplitude of the photoreflectance oscillations with doping. The sign of the peaks seen in Fig. 18 for strong laser intensity, opposite that for low illumination, can be explained as due to the band filling (mechanism (ii)): it is only observed for the purest samples measured.

Striking evidence for the connection between photoreflectance and electroreflectance has been obtained by Cerdeira[50] for a (110) silicon surface. It is well known that the structure in the longitudinal (space-charge barrier) electroreflectance spectrum of a (110) silicon surface is aniso-

tropic around 3.3 eV: the intensity is stronger for the electric field of the measuring light $\underline{E} \parallel (001)$ than for $\underline{E} \perp (001)$. Similar anisotropy has been found in the photoreflectance spectrum, as shown in Fig. 19. This rules out rather conclusively mechanism (ii) and (iii).

Extremely strong photoreflectance signals ($\Delta R/R \sim 10^{-2}$) have been found near the E_o edge of GaAs at 2^o K[48]. The leading peak has been attributed to excitons bound to impurities, with a small binding energy. The effect is strong enough to be observed directly (light on, light off) in the reflection spectrum without the aid of phase-sensitive detection. The nature of this modulation is not understood.

Albers[55] has considered quantitatively mechanism (iii), namely the screening of the electron-hole Coulomb interaction by the injected free carriers. In a material like CdS the injected holes become trapped and the screening is produced only by the injected electrons. The screened Coulomb potential becomes:

$$V(r) = \exp(-\alpha r)/\varepsilon_o r, \tag{14}$$

where the screening constant is, in the high temperature limit:

$$\alpha = \left\{ \frac{4 \pi N e^2}{\varepsilon_o kT} \right\}^{1/2} \tag{15}$$

(compare with Eq. 13) where N is the free electron density. Albers has solved with the variational trial function:

$$\Gamma = \Gamma_{ex}(\beta)\ e^{-\beta r} \qquad (16)$$

the effective mass equation corresponding to the potential of Eq. (15) with N as a parameter for the $E_o(B)$ exciton of CdS. He finds that the binding energy and the oscillator strength of the ground state, unscreened exciton ($n = 1$) must be multiplied by the functions $\mathcal{G}_1(N)$ and $\mathcal{F}(N)$ shown in Fig. 20. Once these functions are known, it is easy to calculate the screening contribution to the photoreflectance of the $E_o(B)$ exciton of CdS. The calculated results for the experimental conditions of the work of Wang et al.[6] are shown in Fig. 21 compared with the experimental results. From Fig. 21 we must conclude that mechanism (ii) dominates the photoreflectance of the E_o peak of CdS (at least for the dark electron concentration of the sample used in Ref. 6).

Figure 22 shows the line shape of the $E_o(B)$ peak of CdS calculated from mechanism (ii), assuming interband transitions only (no excitons)[54]. This line shape does not agree with the experimental results of Fig. 21.

STRESS MODULATION AND OTHER MODULATION MEASUREMENTS UNDER STATIC STRESS

a) Experimental Techniques

The measurement of the modulation in the optical properties produced by stress presents considerable difficulties: the mechanical motion associated with the modulating stress produces spurious effects sometimes much larger than the modulation in the optical constants. These spurious effects arise from mechanical vibrations in the experimental system (including sound propagation in air), and from lack of uniformity in the reflecting sample surface. Vibrations of the system and sound propagation can be minimized by keeping the size of the vibrating parts of the modulator as small as possible. In this respect great simplicity is achieved by using a thin sample ($\sim$ 0.1 mm thick) glued onto a piezoelectric transducer (e. g. Lead Zirconate-Titanate, supplied by the Clevite Corporation). In order to obtain a well-defined stress configuration it is important to use a long sample with only the ends glued to the transducer: the stress has a well defined configuration away from the sample ends[59].

Piezoabsorption measurements[60] have been made on AgBr samples excited electrostatically into their mechanical vibration modes[61]. The mechanical vibration was excited with a capacitor, one of whose plates was a silver-plated end-face of the sample (an elongated parallelepiped). Resonant frequencies between 50 and 100 kHz were used.

An ingenious system which permits the simultaneous application of a static and a modulating stress has been described by Sell and Kane[62]. The stress

is produced in a pneumatic chamber which is alternately filled and exhausted by a valve. Either a rotary valve driven by a motor or a fast solenoid valve can be used for this purpose. The stress is transmitted by a piston and a push-rod to the sample. The magnitude of the stress can be measured with a transducer (e. g. Kistler 912 quartz force transducer) placed between sample and supporting yoke. Operation takes place at about 100 Hz with modulating forces of about 5 kg rms.

b) Theory

Kane has presented a general group-theoretical symmetry analysis of the effect of stress on the dielectric tensor[63]. While it is not possible to discuss here this very extensive work in detail, we shall mention some of its general features. The work provides a rational basis for a unified notation of the many deformation potentials used in the literature. It may be used to describe effects of stress on interband transitions with or without consideration of the exciton interaction. The stress, a symmetric second rank tensor, is decomposed into its irreducible tensor components: three for a material of the germanium-zincblende family to which we confine our discussion. Only terms linear in stress are included in the Hamiltonian. These terms have a structure formally analogous to the kinetic energy, a quadratic function of p_i and hence also a second rank tensor. Thus the symmetry analysis of the stress Hamiltonian is equivalent to that of the kinetic energy in the effective mass approximation. The effect of stress on the dielectric constant is characterized by a fourth rank tensor which, for the cubic materials under consideration, has only three independent components (like the elastic tensor). These

Components are labeled W_1, W_3, and W_5 in the notation of Kane: the subindex denotes the irreducible representation to which the corresponding irreducible stress belongs. W_1 corresponds to a hydrostatic stress, W_3 and W_5 to a (001) and a (111) shear stress, respectively. The irreducible components W_1, W_3, and W_5 are complex functions of frequency. The changes in the dielectric constant ϵ parallel and perpendicular to the stress for (001) and (111) stresses of magnitude X are:

(001) stress:

$$\delta \epsilon_{||} = \left(\frac{W_1}{3} + \frac{2 W_3}{\sqrt{6}} \right) X$$

$$\delta \epsilon_{\perp} = \left(\frac{W_1}{3} - \frac{W_3}{\sqrt{6}} \right) X \qquad (17)$$

(111) stress:

$$\delta \epsilon_{||} = \left(\frac{W_1}{\sqrt{3}} + 2 W_5 \right) X$$

$$\delta \epsilon_{\perp} = \left(\frac{W_1}{\sqrt{3}} - W_5 \right) X$$

Prominent structure in W_i appears in the neighborhood of critical points. One must distinguish two contributions to this structure: that of stress-induced shifts in gaps and that of changes in matrix elements. The first

contribution is proportional to the derivative of the unperturbed structure in the dielectric constant while the second is proportional to this unperturbed structure. As a result energy shift structure is dominant near a singularity; the ratio of the energy shift to the corresponding matrix element structure is proportional to E_g/Γ, where Γ is the phenomenological energy broadening parameter and E_g the energy gap responsible for the change in matrix element (wave function mixing). Matrix elements changes are only observable for small interacting gaps E_g (such as those produced by spin-orbit interaction).

For small stresses (splittings smaller than exciton binding energies) one must consider the effect of stress on exciton states: their symmetries are obtained as a product of the corresponding band edge symmetries. For stresses which produce splittings large compared with exciton binding energies, the excitons shift tied to the corresponding interband gaps and one must consider interband deformation potentials. Kane has shown[63] that the exciton deformation potentials ($\mathcal{E}$) are smaller than the corresponding band edge deformation potentials (D): the splitting of degenerate bands is not felt as much by an exciton formed from wavefunctions of all degenerate bands. Such differences between low and high stress deformation potentials have yet to be observed experimentally.

Several types of deformation potentials must be considered. The hydrostatic deformation potentials (subscript 1 in Kane's notation) produce uniform

shifts of a given degenerate multiplet. Shear stresses produce splittings of multiplets with a given $\underset{\sim}{k}$ (intraband deformation potentials) and also splittings of the various points of the star of $\underset{\sim}{k}$ (interband deformation potentials). Superscripts 3 and 5 are used ot characterize the corresponding irreducible stress components. We notice that some deformation potentials represent first order changes in matrix elements but only second order (in stress) changes in energies.

The symmetry treatment of the effect of uniaxial stress on ε is usually performed under the assumption of a stress-independent spin-orbit interaction. Actually a hydrostatic compression should increase the spin-orbit splittings as a result of the greater wavefunction confinement (wavefunction renormalization). An OPW calculation[64] yields for the change $\delta\Delta_o$ in the spin-orbit splitting of the valence band of germanium at Γ with hydrostatic stress:

$$\frac{\delta\Delta_o}{\Delta_o} = -4\,\frac{\delta a_o}{a_o} \qquad (18)$$

where a_o is the lattice constant and δa_o its stress-induced variation. Equation (18) can be obtained by a simple argument based on the wave function renormalization associated with the compression. Such renormalizytion would introduce a factor $\sim -3\,\delta a_o/a_o$ in $\delta\Delta_o/\Delta_o$, while the $\underset{\sim}{p}$ dependence of Δ_o introduces another factor $\delta a_o/a$. Experimental results[66] yield a value of $\delta\Delta_o/\Delta_o$ about five times smaller than predicted by Eq. (18). It should be mentioned that recent KKR calculations for CdTe[65], and also experimental

to be discussed later, yield a value of $\delta a_o/a_o$ several times smaller than predicted by Eq. (18). This fact may correspond to a large localization of the corresponding wave functions, so that a change in the unit cell boundaries does not change much the renormalization, or to a change with stress of the relative proportion of metal d wave function in the Γ_{15} state.

The possibility of a non-vanishing dependence of the spin-orbit interaction on uniaxial stress has been suggested by Hensel and Suzuki[69]. Let us consider, for instance, the top valence band of germanium at $k = 0$ (Γ_{25}' orbital symmetry). The conventional treatment of stress as an orbital Hamiltonian, with the spin-orbit interaction taken on the same perturbation - theoretical footing, yields for the stress Hamiltonian three independent matrix elements: $\underline{a}$ (hydrostatic), $\underline{b}$ (pure (001) shear) and $\underline{d}$ (pure (111) shear). If the possibility of a stress dependence of the spin-orbit interaction is to be included, one must consider the double group symmetries of the spin-orbit-split states (Γ_8^+, Γ_7^+) explicitely and a larger number of parameters is needed: the stress coupling between the Γ_8^+ and the Γ_7^+ states is no longer given as a function of the splitting of the Γ_8^+ states only[68]. The stress dependence of the spin-orbit Hamiltonian at Γ_{25}' ($\sim L \cdot \sigma$ in the spherical notation, $L \equiv$ orbital angular momentum, $\sigma \equiv$ Pauli matrices) can be written as:

$$
\begin{aligned}
H_{\varepsilon,so} = {} & \underline{a}_2 (L \cdot \sigma)(e_{xx} + e_{yy} + e_{zz}) \\
& + 3\,\underline{b}_2 \left(L_x \sigma_x - \tfrac{1}{3} L\sigma + c\,p\right) \\
& + \tfrac{3}{2}\,\underline{d}_2 \left\{(L_x \sigma_y + L_y \sigma_x) + c\,p\right\}
\end{aligned}
\qquad (19)
$$

The stress-orbital Hamiltonian is similar in form to that of Eq. (19), with a_2, b_2 and d_2 replaced by other parameters a_1, b_1 and d_1, and σ replaced by L. These Hamiltonians yield the following results for the stress dependence of the Γ_8^+ and Γ_7^+ states:

Hydrostatic stress:

$$\Gamma_8^+ : \quad \Delta E_H = (a_1 + 2a_2)(e_{xx} + e_{yy} + e_{zz}) \tag{20a}$$

$$\Gamma_7^+ : \quad \Delta E_H = (a_1 - a_2)(e_{xx} + e_{yy} + e_{zz})$$

(001) stress

$$\text{linear splitting} : \quad \Delta E_{001} = 2(b_1 + 2b_2)(e_{zz} - e_{xx}) \tag{20b}$$

$$\Gamma_8^+ - \Gamma_7^+ \text{ coupling} : \quad 2^{1/2}(b_1 - b_2)(e_z - e_{xx})$$

(111) stress

$$\text{linear splitting:} \quad \Delta E_{111} = 2\sqrt{3}(d_1 + 2d_2)e_{xy} \tag{20c}$$

$$\Gamma_8^+ - \Gamma_7^+ \text{ coupling:} \quad \sqrt{6}(d_1 - d_2)e_{xy}$$

Equations (20) indicate that the $\Gamma_8^+ - \Gamma_7^+$ coupling is related to the linear splitting when no stress dependence of the spin-orbit interaction exists. Simultaneous measurements of the $\Gamma_8^+ - \Gamma_7^+$ coupling and the Γ_8^+

splitting should yield both orbital and spin-orbit deformation potentials. The $\Gamma_7^+ - \Gamma_8^+$ coupling can be measured either by observing non-linear terms in the Γ_8^+ splitting or by studying the linear stress dependence of matrix elements (or strength of optical structure). The stress dependence of matrix elements can also be obtained from a study of the stress dependence of effective masses in cyclotron resonance[69]. A detailed pseudopotential calculation of the effect of stress on the band structure of germanium has been performed by Saravia and Brust[70]. The pseudopotential Hamiltonian was linearized with respect to strain: quadratic strain dependences could, however, arise through the coupling of neighboring states via the linear strain Hamiltonian. The atomic form factors of the pseudopotential were assumed to have spherical symmetry and to be independent of stress for a given reciprocal lattice vector K (rigid ion model). The required derivatives of the atomic form factors were obtained from screening theory[71]. These calculations give deformation potentials for the E_o, $E_o+\Delta_o$ edge ($\Gamma_{25'} \rightarrow \Gamma_{2'}$ transitions) and for the E_1, $E_1+\Delta_1$ edge ($\Lambda_3 \rightarrow \Lambda_1$) in good agreement with piezo-electroreflectance measurements[68]. Figure 23 shows the variation of the energies of the E_o, $E_o+\Delta_o$, E_1 and $E_1+\Delta_1$ peaks of germanium with stress as calculated by Saravia and Brust[70] and as determined from piezo-electroreflectance[68]. (The unperturbed interband energies are taken equal to zero). The agreement between theory and experiment is generally good, in particular the quadratic increase in Δ_1 with stress due to the repulsion between the two spin-orbit split Λ_3 states. The calculated quadratic dependence on stress of the low-energy component of E_o, due to a similar $\Gamma_8^+ - \Gamma_7^+$ repulsion, is for a (001) stress smaller than experimentally observed. The opposite is true for a (111) stress. This

fact will be discussed later in connection with wavelength modulation experiments in silicon under static stress. Notice that the quadratic increase in Δ_1 calculated for a (111) stress ($(\bar{1}11)$, $(1\bar{1}1)$ and $(11\bar{1})$ valleys) is not observed experimentally.

All one-electron energy levels of a solid at $k = 0$ have, at least, the Kramers degeneracy. If one considers excitonic instead of one-electron transitions the Kramers degeneracy, valid only for an odd number of particles, may be lifted by the exciton interaction (electron-hole exchange). The simplest example of this effect is obtained for the fundamental edge of wurtzite-type materials ($\Gamma_9 \rightarrow \Gamma_7$ for the so-called A line). The corresponding exciton has as symmetry:

$$\Gamma_9 \times \Gamma_7 = \Gamma_5 + \Gamma_6$$

Only the double degenerate Γ_5 exciton is allowed for optical dipole transitions and only one A-peak is seen in absorption. A stress perpendicular to the c-axis (e. g. along z) splits the (x,y) degeneracy of the Γ_5 exciton into two lines polarized along x and y respectively. This splitting is the combined effect (cross term) of stress and exciton exchange on the excitons. It can be regarded as the result of the bilinear repulsion between the A and B excitonic levels. Exchange-stress splittings of Kramers degeneracies have been observed in conventional reflectivity measurements for CdS, CdSe and ZnO. As we shall show later, modulated piezoreflectance and wavelength derivative spectroscopy with a high static stress are excellent techniques to study these splittings.

c) Results: Modulated Stress

Figure 24 shows the piezotransmission spectrum of the indirect edge of AgBr obtained by Ascarelli[60] for a (111) stress at 12° K. The polarization dependence of this spectrum together with the insensitivity to polarization found for a (001) stress, confirms the (111) symmetry of the valence bands involved in these transitions (the conduction minimum is at (000)). A great wealth of structure is present. The first strong peak is interpreted as indirect transitions to the ground state of the exciton (n = 1) with emission of an LA phonon: the exciton is formed with dressed (polaron) electron and hole states. Weaker phonon absorption structure is also seen at lower energies. Ascarelli suggested the existence of a valley-orbit splitting (singlet-triplet) in the main peak ($n = 1 + h\omega_{LA}$). However, it has been recently shown that such a splitting is impossible[72]. Ascarelli also interpreted some of the structure in Fig. 24 as due to excitons formed with undressed electrons (without polaron well) and dressed holes and vice versa (e. g. TRIPLET + $h\omega_{LA}$ + (pol)). From these data he deduced values for the electron and hole polaron coupling constants ($\alpha_e = 1.69$, $\alpha_h = 2.5$) which are in agreement with other experiments.

Figure 25 shows the piezoreflectance spectrum of the direct (E_o) edge of GaSb, as obtained with the piezoelectric transducer method, for stresses along (001) and (111) and for polarization parallel and perpendicular to the stress[59]. A strong polarization dependence is apparent. It is due to the splitting of the corresponding valence band (Γ_8) under the uniaxial compression: for $E||X$ transitions from the $\left(\frac{3}{2}, \frac{3}{2}\right)$ split band are for-

bidden, while for $E \perp X$ transitions from $\left(\frac{3}{2}, \frac{1}{2}\right)$ are only very weakly allowed. As a result, the effective shift produced by the stress on the energy gap is $\delta\omega_H - \frac{1}{2}\delta\omega$ for $E \parallel X$ and $\delta\omega_H + \frac{1}{4}\delta\omega$ for $E \perp X$ ($\delta\omega_H$ is the hydrostatic component of the shift; $\delta\omega$ the uniaxial splitting). From the ratio of signal amplitudes:

$$\left(\frac{\Delta R_{\parallel}}{\Delta R_{\perp}}\right) = \frac{\delta\omega_H - \frac{1}{2}\,\delta\omega}{\delta\omega_H + \frac{1}{4}\,\delta\omega} \quad , \tag{21}$$

it is possible to determine the ratio $\delta\omega/\delta\omega_H$. Whenever $\delta\omega_H$ is known from measurements under hydrostatic pressure $\delta\omega$, and thus the shear deformation potentials of the valence band, can be determined.

Table II shows the values of b and d found with these and other measurements for several diamond- and zincblende-type materials. The ratio $d/\sqrt{3}b$ of the splittings for the same strain along either (111) or (001) increases in going from a group IV to a III-V and to a II-VI material. This increase seems related to the increasing ionic charge.[59]

Figure 26 shows piezoreflectance spectra of the A and B (E_o) excitons of CdS and CdSe for a stress along $(11\bar{2}0)$ and light polarized with $E \perp c$ for E parallel and perpendicular to the stress. According to one-electron theory both polarizations should give the same spectrum because of Kramers degeneracy. It is clearly seen in Fig. 26 that the A peak is stronger for $E \perp X$ than for $E \parallel X$. The opposite is true of peak B at least for CdS. This fact can be attributed, as discussed

earlier, to exchange splitting of the degenerate Γ_5 excitons. From the ratio of intensities for both polarization directions information about the exchange coupling constant has been obtained[59].

Figure 27 shows the irreducible components of the strain-optical tensor of germanium (W_1, W_3, W_5) obtained by Sell and Kane with their pneumatic stress modulation apparatus. The spectral region is that of the E_1-E_1+Δ_1 peaks, which correspond to transitions at Λ ((111)) critical points: no energy shift or splitting should occur for a (001) stress. Hence the coefficient W_3, which corresponds to a (001) stress, should be zero if changes of matrix elements with stress are neglected. This is not the case in Fig. 27 and therefore W_3 must be due to changes in matrix elements with stress. The larger width of the W_3 structure, as compared with that in W_1 and W_5 due to energy shifts, confirms this conclusion. Figure 27 (b) shows a theoretical fit (solid line) to the experimental data from which the deformation potential $D_3{}^3$ which produces the changes in matrix element (orbital coupling by the stress between the Λ_6 and $\Lambda_{4,5}$ valence bands) can be obtained. This deformation potential agrees with electroreflectance results under large uniaxial stress. The W_5 of Fig. 27 (c) is the sum of an energy shift (deformation potential $D_1{}^5$ of E_1) and a matrix element change contribution (deformation potential $D_3{}^5$). From a theoretical fit to this curve $D_1{}^5 = 7.5$ eV and $D_3{}^5 = 1.5$ eV can be obtained. A discrepancy seems to exist between this value of $D_3{}^5$ and piezo-electroreflectance measurements[68].

d) Results: Modulation Experiments under Static Uniaxial Stress

The wavelength derivative technique has been profusely used to study effects of high static stress on the optical spectra. As an example we show in Fig. 28 the dependence on (111) stress of the peaks observed with wavelength modulated transmission at the indirect edge of AlSb. Peaks corresponding to absorption and emission of LA, TA, LO and TO phonons at or very near the X point are observed at 77° K. It is interesting to note that the TO_e (emission of transverse optical phonons) peaks are only resolved when stress is applied. From the splitting of the peaks with stress shown in Fig. 23 the shear deformation potential can be determined (see Table II). The shift of the center of mass of the split peaks yields the hydrostatic deformation potential of the indirect gap a_i = + 2.2 eV. This deformation potential is considerably larger than that obtained from work under hydrostatic pressure (+ 1 eV): similar discrepancy is found for Ge, Si and GaP[73]. Analogous measurements on AlSb under a (001) stress yield the shear deformation potentials b (see Table II) and ξ_2 = + 5.4 eV.

The low-energy components of the split doublets of Fig. 23 should actually exhibit non-linearities associated with the stress coupling of the $\left|\frac{3}{2}, \frac{1}{2}\right\rangle$ and $\left|\frac{1}{2}, \frac{1}{2}\right\rangle$ states discussed earlier. Such non linearities cannot be ascertained in Fig. 23: they are expected to be very small because of the large spin-orbit splitting of AlSb. A detailed study of these non-linearities can be performed in silicon, a materials with a (001) indirect edge similar to that of AlSb. The high yield stress of Si makes it possible to obtain valence band splittings as high as 0.08 eV, larger than the spin-orbit splitting Δ_o = 0.04 eV. Under these conditions, the corresponding non-linearities cannot be described by second order perturbation theory:

a diagonalization of the corresponding 2×2 valence band Hamiltonian is necessary. The experimental results obtained with wavelength-modulated transmission for a (111) stress are shown in Fig. 29. Both the A_1 and the A_2 lines show a non-linear behavior. The non-linear behavior of the A_1 peak $\left[\left(\frac{3}{2}, \frac{1}{2}\right) \rightarrow \text{conduction band}\right]$ can be explained as due to the $\left(\frac{3}{2}, \frac{1}{2}\right) - \left(\frac{1}{2}, \frac{1}{2}\right)$ coupling: the dashed line shows the corresponding linear behavior. A fitting of this non-linearity requires a stress dependence of the spin-orbit interaction $(d_2 = + 0.14 \pm 0.05$ eV, see Eq.(19)). The non-linearity in A_2 must be due to another mechanism since the stress produces no $\left(\frac{3}{2}, \frac{3}{2}\right) - \left(\frac{1}{2}, \frac{1}{2}\right)$ coupling. It has been suggested that this non-linearity is associated with the stress coupling between the Δ_1 and Δ_2' conduction bands, related to the splitting of the X_1 degeneracy for a (111) stress. From the results of Fig. 29 one obtains for this coupling a deformation potential $|\Xi_2^*| = 13 \pm 4$ eV. The consideration of these non-linearities is very important for the determination of the small hydrostatic deformation potential a_i based on the average shift of A_1 and A_2. Laude et al.[73] obtained $a_i = + 1.5 \pm 0.3$, in rather good agreement with the results of hydrostatic pressure work. Hence the discrepancy between hydrostatic and uniaxial determinations of a_i mentioned above disappears when non-linearities are properly taken into account. Such discrepancies may be due to similar reasons for the other indirect gap materials (GaP, Ge, AlSb).

Strongly non-linear shifts have also been observed[73] for the indirect excitons of silicon under (001) and (011) stress. The (001) stress measurements yield the spin-orbit deformation potential $b_2 = - 0.15 \pm 0.07$.

It is interesting to note that the deformation potential $\underline{d}_2$ obtained for silicon agrees in sign with calculations by Suzuki and Hensel based on a rigid-ion model:

$$\underline{b}_2 = +0.01$$
$$\underline{d}_2 = +0.004 \qquad (22)$$

The sign of b_2 found experimentally for silicon is opposite to that given in Eq. (22). The experimental magnitude of $\underline{b}_2$ and $\underline{d}_2$ is also considerably larger than that given in Eq. (22). As indicated in connection with Fig. 23 (also unpublished results) piezo-electroreflectance measurements also yield for germanium $d_2 > 0$ and $b_2 < 0$: for a (001) stress the non-linearity of the $\left(\frac{3}{2}, \frac{1}{2}\right)$ state is larger and for a (111) stress smaller than calculated from the linear splitting in the absence of stress dependence of the spin-orbit interaction. Hensel and Suzuki found for germanium $d_2 > 0$ and $b_2 > 0$ from cyclotron resonance measurements under stress. The reason for the discrepancy in the sign of b_2 is not understood.

Melz[66] has performed electroreflectance measurements in germanium and CdTe under hydrostatic stress. He obtained from these measurements the hydrostatic deformation potentials of the Δ_o (for CdTe and Ge) and the Δ_1 (for CdTe only) spin-orbit splittings. The corresponding pressure coefficients are listed in Table III. We have also listed on this table the prediction of Eq. (18) and the results of recent calculations by the Korringa-Kohn-Rostocker or Green's functions method[65]. These calculations yield smaller pressure coefficients than Eq. (18), in better agreement with the experimental results.

Rowe et al.[74] have performed wavelength-modulated reflectance measurements of the E_1 and $E_1+\Delta_1$ peaks of GaAs under a (001) stress. A splitting of these peaks appears (see Fig. 30), contrary to the expectations of one-electron theory. The selection rules associated with this splitting, and shown also in Fig. 30, suggest it is due to exchange-stress splitting of excitons; considerable effects of exciton interaction are known to be present at these E_1 and $E_1+\Delta_1$ peaks.

Measurements of the shift of the exciton peaks of selenium under static uniaxial stress have been recently performed by Tuomi using wavelength derivative spectroscopy

A rather unusual stress modulation experiment, involving the L_{III} x-ray emission spectrum of copper, has been reported recently by Willens et al.[76]. The sample was loaded and unloaded at 10 sec intervals with a stress of about 100 kg/cm^2. Photon counting, rather than phase-sensitive detection was used. Figure 31 shows the modulation spectrum obtained. The authors point out that this spectrum is not simply the derivative of the standard emission spectrum, thus indicating that valence band states with widely different deformation potentials are involved in the emission process.

OTHER MODULATION TECHNIQUES

a) Experimental Methods

Thermoreflectance

Temperature modulation can be easily accomplished with the Joulean heat produced by a modulating current[5]. Moderatly conducting samples can be heated by passing a current through them, while more insulating ones can be heated indirectly. A silver-paint strip onto which the sample is glued provides an easy indirect heater. The modulating frequencies must be kept low ($\sim$ 10 Hz) unless very thin samples (e. g. vacuum deposited) are used.

Dzhioeva et al.[77] have used a CO_2 laser (wavelength 10.6 μ) focused on the sample as the temperature modulator. The laser was chopped at 20 Hz. The possibility of a photoreflectance contribution to the signal is excluded if the photon energy of the laser is below the fundamental edge of the material.

Wavelength Modulation

As mentioned earlier, wavelength modulation spectra are somewhat simpler to interpret than those based on external modulation techniques. For wavelength modulation spectroscopy double beam systems must be used so as to eliminate structure in the wavelength derivative of the incident spectrum[78]. An example of such a system is shown in Fig. 32. Two modu-

lation channels are used: amplitude modulation at the frequency Ω_1 and wavelength modulation at the frequency Ω_2. The wavelength modulation is produced by a vibrating plate placed in the optical path inside of the monochromator. This plate may be driven either with a motor-eccentric system[78] ($\sim$ 25 Hz) or at higher frequencies ($\sim$ 500 Hz) with a ferroelectric bimorph[79]. The signal at the frequency Ω_1 in photomultiplier PM1 is proportional to the incident intensity I_o, while that in PM2 is proportional to $I = I_o R$ (R = sample reflectivity). At the frequency Ω_2, the signal in PM1 is proportional to $dI_o/d\lambda$, while that in PM2 is proportional to $RdI_o/d\lambda + I_o dR/d\lambda$. A servo acts on the high voltage of PM1 so as to keep the output of the differential amplifier at the frequency Ω_1 equal to zero. Under these conditions the spurious signal $RdI_o/d\lambda$ is automatically eliminated provided the spectral dependence of the sensitivity of PM1 and PM2 is the same. A second servo regulates the high voltage of PM2 so as to keep its dc output constant. Under these conditions the recorder yields directly a plot of $dR/Rd\lambda$.

Spatial Modulation

When a sample has a spatial inhomogeneity in its optical properties, mechanical motion can be used as a means of producing optical modulation. This technique should be useful to study samples with a gradient in composition (e. g. alloys), or impurity concentration. It has been used by McNatt and Handler to study the optical properties in the neighborhood of a grain boundary in germanium bicrystals.[80] The measurements were performed by transmission with the arangement of Fig. 33. The motion of the bycrystals was accomplished with a pair of vibrating ferroelectric bimorphs. The

measurements with this configuration must be performed at the second harmonic of the modulating frequency. McNatt et al. found a component of the modulated signal associated with the disorder at the grain boundary and another one due to the electric field in the space-charge layer associated with the grain boundary (essentially electroabsorption). This second component can be enhanced by application of a biasing voltage to the bicrystal.

b) Results and Discussion

Thermoreflectance and Energy Derivative

Matatagui et al.[81] have published the thermoreflectance spectra of a number of zincblende- and wurtzite-type semiconductors. They suggested that these spectra are quite similar to photon-energy-derivative spectra since the main modulation mechanism is the temperature modulation of the energy gap. The other possible mechanism, modulation of the thermal broadening, was shown to be considerably smaller. Walter and Cohen[82] have calculated the photon-energy derivative of the reflection spectra of GaAs, GaP, ZnSe and ZnS and shown that it is in good semiquantitative agreement with the results of thermoreflectance measurements. Photon-energy- (or wavelength-) derivative spectra have recently become available for GaAs, GaSb, InAs, InSb, Ge and Si[36]. Figure 34 shows the energy derivative reflection spectrum of GaSb at 80° K compared with the thermoreflectance spectrum[81] at the same temperature and with the calculated energy derivative spectrum[37]. Except for the E_1 peak, the measured energy derivative spectrum agrees with the theoretical one more closely than the thermoreflectance spectrum: some broadening modulation contribution is probably present in the thermoreflectance spectrum. The positive and the negative swing of the calculated E_1 peak have about the same strength. The measured peaks show a suppression of the lower energy positive swing and an enhancement of the negative swing. This effect, which seems particularly strong in the energy derivative spectrum is present in most materials of zincblende structure[83]. It has been attributed to exciton interaction at E_1 critical points which have M_1

character with a very large negative mass. The E_o' and E_1' peaks have already been discussed in connection with Table I. Considerable structure, difficult to identify with certainty, appears at the high energy side of E_2.

Shaklee and Nahory[72] have recently reported the wavelength-derivative transmission spectrum of silicon at 1.8° K, in the region of the indirect gap. They were able to observe excited states (n = 2) of the indirect excitons (TO-phonon-aided), and also to identify exciton transitions which take place with the emission of LO-phonons. Previous evidence of valley-orbit splitting, obtained from a fit of the conventional absorption spectra[84], was shown to be spurious. This fact illustrated once more the advantages of the modulation techniques with respect to conventional spectroscopy.

c) Covalent Bonding and Energy Gaps

As we have mentioned, a large amount of information has been obtained about critical energy gaps by means of modulation spectroscopy, especially for the materials with zincblende structure. The crystal potential of a zincblende-type crystal can be decomposed as the sum of a component symmetric with respect to the permutation of the two atoms in the unit cell plus an antisymmetric component. It is customary to assume that the symmetric potential is the same as that of the isoelectronic group-four element; when the two component atoms belong to different rows of the periodic table an appropriate average isoelectronic group-four element must be taken. In the so-called two-band model the effect of the antisymmetric potential is to introduce an off-diagonal matrix element between valence and conduction bands. Under these conditions energy gaps E_j of a partially ionic material are given by the solution of a quadratic equation[85]:

$$E_j = E_{j,h} \left[1 + \left(\frac{C}{E_{i,h}} \right)^2 \right]^{1/2} , \qquad (23)$$

where $E_{j,h}$ is the analogous gap of the corresponding group IV material. The parameter C is assumed to be the same for all gaps E_j; it can be expressed as a function of the ionic radii or alternatively obtained from the infrared dielectric constant. The values of C for zincblende-type materials have been tabulated by Van Vechten[85].

With a few simple assumptions about the scaling of $E_{j,h}$ with lattice constant, Eq.(23) can be used to obtain the main gaps (E_o, E_1, E_o', E_2, E_1') observed in germanium- and zincblende-type materials[85]. We shall discuss here the application of Eq. (23) to the calculation of the concentration dependence of energy gaps in pseudobinary alloy systems[86]. This dependence is known largely through reflection modulation measurements[87-89]. It can be represented by the quadratic expression:

$$E_j = a + bx + cx^2 \ , \qquad (24)$$

where x is the concentration of a given component. Equation (23) yields a non-linear dependence of E_j on x if one assumes that $E_{j,h}$ and C vary linearly with x. The results calculated by Van Vechten for the E_o gap of the GaAs-GaP system are shown in Fig. 35, together with the experimental data of Thompson et al. (only the deviation from linearity is plotted)[87]. The agreement between theory and experiment is excellent. Results of a pseudopotential calculation with form factors linearly dependent on x (see also Fig. 35) give a deviation from linearity of a sign opposite to that observed experimentally. We should point out, however, that Jones and Lettington[90] were able to explain the deviation from linearity for the GaAs-InAs system, similar to that shown in Fig. 35, with linearly interpolated pseudopotential form factors.

In more ionic zincblende-type materials (II-VI, I-VII compounds) deviations from linearity larger than those obtained with Eq.(23) are observed.

These larger deviations can be interpreted as an additional decrease in the gap produced by the random potential. Van Vechten and Bergstresser[86] have suggested that a significant random fluctuation is produced only by the antisymmetric potential, and thus related to differences of the antisymmetric constants C of the constituents. For an alloy of formula $AF_{0.5}G_{0.5}$ the fluctuation in C can be written as:

$$C_{FG} = be^2 Z \left| \frac{1}{r_F} - \frac{1}{r_G} \right| e^{-k_s R} \qquad (25)$$

where b is a constant of the order of one, Z the valence of the atoms F and G, r_F and r_G the corresponding covalent radii (essentially one-half of the nearest neighbor distance of the group IV material of the same row), k_s the Fermi-Thomas radius of the valence electrons and R the average covalent radius $\left(R = \frac{1}{2} (r_A + 0.5\, r_F + 0.5\, r_G) \right)$. The decrease in gap due to the random potential is quadratic in C_{FG} (second-order perturbation) and thus should be equal to:

$$C_{FG}^2 / \alpha , \qquad (26)$$

where α is a constant which, for the sake of simplicity, is taken to be the same for all zincblende-type materials.

		E'_o					E_2					E'_1	
	Wavelength Derivative	4.44	4.60				5.11	5.64	5.91	6.07			
GaAs	Electroreflectance	4.53	4.71	4.91			5.14	5.53	5.76	6.00	6.26		
	Calculated	4.35	4.50				4.94		5.85		6.5	6.7	
	Wavelength Derivative	3.35	3.69				4.35	4.55	4.75	5.07	5.51	5.65	
GaSb	Electroreflectance	2.94	3.20	3.34	3.41	3.75	4.34	4.57	4.72	5.11	5.62	5.98	
	Calculated	3.32	3.64				4.4				5.6	6.0	
	Wavelength Derivative	4.39	4.58				4.74	4.95	5.33	5.52			
InAs	Electroreflectance 300° K	4.44					4.70		5.19				
	Calculated	4.2	4.4				4.75	6.0			6.3	6.5	6.8
	Wavelength Derivative	3.39	3.78				4.23	4.56	4.75	4.92	5.33	5.50	5.98
InSb	Electroreflectance 300° K	3.18	3.37	3.57	3.72		4.08	4.66			5.25		
	Calculated	3.18	3.42	3.51	3.75		4.4	4.9			5.15	5.50	5.9
	Wavelength Derivative	3.20					4.49	5.01			5.65	5.88	
Ge	Electroreflectance 300° K	3.13	3.32				4.42				5.25	5.43	5.77

Table I. Energies (in eV) of the E'_o, E_2 and E'_1 peaks observed in the derivative reflectance[36] and the electroreflectance[15] of several semiconductors. Data at low temperatures ($T < 80^\circ$ K) unless specified. Also corresponding peaks in the calculated wavelength derivative spectra.

	Ge	GaAs	GaSb	InP	ZnS	CdTe
b (eV)[a]	- 2.8	- 1.75	- 3.3	- 1.55	- 0.53	- 1.1
	- 2.6[b]	- 2.0[b]				- 1.18[c]
d (eV)[a]	- 4.95	- 5.55	- 8.35	- 4.4	- 3.7	- 5.45
	- 4.7[b]	- 6.0[b]				- 4.84[c]

a) The values b and d have an uncertainty of ±20 % which includes a 10 % uncertainty in the values of a.

b) See Ref. 68.

c) D.G. Thomas, J. Appl. Phys. 32S, 2298 (1961).

Table II. Deformation potentials b and d obtained from piezo-reflectance (see Ref. 59) and other measurements for several germanium and zincblende-type semiconductors

		$\frac{d\Delta_i}{dP}$ (10^{-7} eV/bar)	$\frac{d\Delta_i}{dP}$ (10^{-7} eV/bar)	$\frac{d\Delta_i}{dP}$ (10^{-7} eV/bar)
		Experiment[a]	Simple Theory[a]	KKR Theory[b]
CdTe	Δ_o	7 ±2	28	12
	Δ_1	5 ±7	18	12
Ge	Δ_o	1 ±1	5	

a) from Ref. 66

b) from Ref. 65

Table III. Hydrostatic pressure coefficients of the Δ_o and Δ_1 spin-orbit splitting of CdTe and the Δ_o gap of germanium as obtained experimentally, and as calculated with Eq. (18) (simple theory) and with the KKR method.

Literature

1. T.S. Moss, J. Appl. Phys. 32 S, 2136 (1961)

2. P. Handler, Proceedings of the International Conference on the Physics of Semiconductors, Paris 1964, (Dunod eds., Paris, 1965)

3. B.O. Seraphin and R.B. Hess, Phys. Rev. Letters 14, 138 (1965)

4. W.E. Engeler, H. Fritzsche, M. Garfinkel and J.J. Tiemann, Phys. Rev. Letters 14, 1069 (1965)

5. B. Batz, Solid State Commun. 4, 241 (1965)

6. E.Y. Wang, W.A. Albers and C.E. Bleil, in "II-VI Semiconducting Compounds" D.G. Thomas, ed. (Benjamin, New York, 1967) p. 136

7. A.G. Thompson, M. Cardona, K.L. Shaklee and J.C. Woolley, Phys. Rev. 146, 601 (1966)

8. J.G. Mavroides, M.S. Dresselhaus, R.L. Aggarwal and G.F. Dresselhaus, Proc. Phys. Soc. Japan Suppl. 21, 184 (1966)

9. S.H. Groves, C.R. Pidgeon and J. Feinleib, Phys. Rev. Letters 17, 463 (1966)

10. B.O. Seraphin, Electroreflectance, in "Semiconductors and Semimetals", edited by R.K. Willardson and A.C. Beer (Academic Press, Inc. New York), Vol. VI

11. B.O. Seraphin, Modulated Reflectance, in "Optical Properties of Solids" edited by F. Abeles (North Holland Publishing Co., in press)

12. M. Cardona, Modulation Spectroscopy Supplement 11 to "Solid State Physics", edited by F. Seitz, D. Turnbull and H. Ehrenreich (Academic Press Inc., New York, 1969)

13. D.E. Aspnes and N. Bottka, Electric Field Effects on the Dielectric Function of Semiconductors and Insulators in "Semiconductors an Semimetals", edited by R.K. Willardson and A. Beer, Vol. VI (Academic Press Inc., New York)

14. M. Cardona, K.L. Shaklee and F.H. Pollak, Phys. Rev. 154, 696 (1967)

15. R. Glosser, B.O. Seraphin and J.E. Fischer, Phys. Rev., to be published

16. B.J. Parsons and H. Piller, Proceedings of the Conference on Electronic Density of States (National Bureau of Standards, Gaithersburg, Md., 1969), to be published

17. F. Evangelisti and A. Frova, Solid State Commun. 6, 62 (1968)

18. A. Frova and D.E. Aspnes, Phys. Rev. 182, 795 (1969)

19. D.E. Aspnes and A. Frova, to be published

20. Y. Hamakawa, P. Handler and F.A. Germano, Phys. Rev. 167, 709 (1968)

21. B.O. Seraphin, Surface Sci., 8, 399 (1967)

22. D.E. Aspnes and A. Frova, Solid State Commun. 7, 155 (1969)

23. P. Handler, S. Jasperson and S. Koeppen, Phys. Rev. Letters 23, 1387 (1969)

24. R.A. Forman, D.E. Aspnes and M. Cardona, J. Phys. Chem. Solids, in press

25. J.E. Fischer, D.E. Kyser, and N. Bottka,

26. H.I. Ralph, J. Phys. C 1, 378 (1968)

27. R. Enderlein, Phys. Stat. Sol. 26, 509 (1969). As pointed out in Refs. 28 and 30 this paper contains a serious error.

28. J.D. Dow and D. Redfield, Phys. Rev., to be published

29. D.F. Blossey, Ph. D. Thesis, University of Illinois, 1969

30. C.M. Penchina, J.K. Pribram and J. Sak , to be published

31. D.E. Aspnes, Phys. Rev. 147, 554 (1966), Ibid 153, 972 (1967)

32. C.B. Duke and M.E. Alferieff, Phys. Rev. 145, 583 (1966)

33. H.D. Reese, J. Phys. Chem. Solids 29, 143 (1968)

34. D.E. Aspnes, P. Handler and D.F. Blossey, Phys. Rev. 166, 921 (1968)

35. J.E. Rowe and D.E. Aspnes, Bull. Am. Phys. Soc. 15, 288 (1970)

36. R.L. Zucca and Y.R. Shen, to be published

37. C.W. Higginbotham, Ph. D. Thesis, Brown University, 1970

38. R. Glosser and B.O. Seraphin, Z. Naturforsch. 24a, 1320 (1969)

39. E.W. Williams, Sol. State Commun. 7, 541 (1969)

40. A. Daunois, J.L. Deiss and S. Nikitine, Compt. Rend. Acad. Sc. 268, 977 (1969)

41. E. Mohler, Phys. Stat. Sol. 29, K 55 (1968)

42. S. Brahms and M. Cardona, Solid State Commun. 6, 733 (1968)

43. J.L. Deiss, A. Daunois and S. Nikitine, Proceedings of the Conference Molecular Spectroscopy, Liège, 1969, to be published

44. A. Daunois, J.L. Deis and S. Nikitine, Compt. Rend. Acad. Sc. 268, 930 (1969)

45. Ch. Gähwiller and G. Harbeke, Phys. Rev. 185, 1141 (1969)

46. H. Piller, B.O. Seraphin, K. Markel and J.E. Fischer, Phys. Rev. Letters 23, 775 (1969)

47. G. Weiser and J. Stuke, Phys. Stat. Sol. 35, 747 (1969)

48. J.L. Shay and R.E. Nahory, Solid State Commun. 7, 945 (1969)

49. R.E. Nahory and J.L. Shay, Phys. Rev. Letters 21, 1569 (1968)

50. F. Cerdeira and M. Cardona, Solid State Commun. 7, 879 (1969)

51. D.E. Aspnes, Solid State Commun., in press

52. F. Cerdeira, unpublished

53. N.G. Nilson, Solid State Commun. 7, 479 (1969)

54. J.G. Gay and L.T. Klauder, Jr. Phys. Rev. 172, 811 (1968)

55. W.A. Albers, Jr. Phys. Rev. Letters 23, 410 (1969)

56. J.L. Shay, R.E. Nahory and C.K.N. Patel, Phys. Rev. 184, 809 (1969)

57. C.R. Pidgeon, S.H. Groves and J. Feinleib, Solid State Commun. 5, 677 (1967)

58. J.L. Shay, Phys. Rev., in press

59. A.A. Gavini and M. Cardona, Phys. Rev., in press

60. G. Ascarelli, Phys. Rev. Letters 20, 44 (1968)

61. G. Ascarelli and A. Barone, Nuovo Cimento 37, 818 (1965)

62. D.D. Sell and E.O. Kane, Phys. Rev. 185, 1103 (1969)

63. E.O. Kane, Phys. Rev. 180, 852 (1969)

64. D. Brust and L. Liu, Solid State Commun. 4, 193 (1966)

65. F. Cerdeira and J. de Witt, private Communication

66. P.J. Melz, Bull. Am. Phys. Soc. 14, 417 (1969)

67. K. Suzuki and J.C. Hensel, Bull. Am Phys. Soc. 14, 113 (1969)

68. F.M. Pollak and M. Cardona, Phys. Rev. 172, 816 (1968)

69. J.C. Hensel and K. Suzuki, Bull. Am. Phys. Soc. 14, 113 (1969)

70. L.R. Saravia and D. Brust, Phys. Rev. 178, 1240 (1969)

71. W.A. Harrison, Pseudopotentials in the Theory of Metals (W. A. Benjamin, Inc., New York, 1966)

72. K.L. Shaklee and R.E. Nahory, to be published

73. L.D. Laude, M. Cardona and F.H. Pollak, Phys. Rev., in press; also to be published

74. J.E. Rowe, F.H. Pollak and M. Cardona, Phys. Rev. Letters 22, 933 (1969)

75. T.O. Tuomi, Phys. Stat. Sol., in press

76. R.H. Willens, H. Schreiber, E. Buehler and D. Brasen, Phys. Rev. Letters 23, 413 (1969)

77. S.G. Dzhioeva, V.S. Ivanov and V.B. Stopachinskii, Physics and Technics of Semiconductors 3, 1316 (1969)

78. K.L. Shaklee and J.E. Rowe, Applied Optics, in press

79. A. Perregaux and G. Ascarelli, Appl.Opt. 7, 2031 (1968)

80. J.L. McNatt and P. Handler, Phys. Rev. 178, 1328 (1969)

81. E. Matatagui, A.G. Thompson and M. Cardona, Phys. Rev. 176, 950 (1968)

82. J.P. Walter and M.L. Cohen, Phys. Rev. 183, 763 (1969)

83. E.O. Kane, Phys. Rev. 180, 852 (1969)

84. P.J. Dean, Y. Yafet and J.R. Haynes, Phys. Rev. 184, 837 (1969)

85. J.A. Van Vechten, Phys. Rev. Oct. 15, (1969)

86. J.A. Van Vechten and T.K. Bergstresser, Phys. Rev., in press

87. A.G. Thompson, M. Cardona, K.L. Shaklee and J.C. Wooley, Phys. Rev. 146, 601 (1966)

88. A.G. Thompson, J.E. Rowe and M. Rubenstein, J. Appl. Phys. 40, 3280 (1969)

89. E.M. Williams and V. Rehn, Solid State Commun. 7, 545 (1969)

90. D. Jones and A.H. Lettington, Solid State Commun. 7, 1319 (1969)

Figure Captions

Fig. 1 Block diagram of the electronic, electrolytic, and optical system used by Aspnes and Frova[19] for electroreflectance measurements with simultaneous surface capacitance and fast photovoltage measurements.

Fig. 2 Surface field homogeneity parameter as a function of surface field for various dopings, as measured by the parameter U_B. This figure shows that at high fields best homogeneity is obtained with extrinsic samples ($U_B \neq 0$). From Ref. 23.

Fig. 3 Effect of an electric field (measured by the field strength parameter f) on a hydrogenic exciton spectrum. From Ref. 26

Fig. 4 Effect of an electric field (measured by the field strength parameter f) on an M_3 edge including exciton effects. From Ref. 29

Fig. 5 Electroreflectance spectrum of the E_o peak of nearly intrinsic germanium for various values of the surface potential. The corresponding surface field is also given. From Ref. 19.

Fig. 6 Real and imaginary parts of $\langle \Delta\varepsilon \rangle$, the effective dielectric constant for space-charge barrier electroreflectance, at various values of the surface field $\mathcal{E}_s$ for nearly intrinsic germanium.
From Ref. 22.

Fig. 7 Magnitude of the electroreflectance peaks I, II, and III (see insert) as a function of surface field $\mathcal{E}_s$. The dashed curved was obtained theoretically; the points experimentally with the dry-sandwich technique. From Ref. 18.

Fig. 8 Shift in the position of peaks I, II, and III of Fig. 7 with surface field. The dashed curves are calculated with the theory of Aspnes and Frova. From Ref. 18.

Fig. 9 Evaluation of the peak - to - peak amplitude of the transverse electroreflectance E_o signal of GaAs at 77° K as a function of reduced field $\mathcal{E}/\mathcal{E}_o$. The points are experimental. The full curve was calculated with a broadening parameter Γ = 11 meV. From Ref. 24.

Fig. 10 Transverse electroreflectance spectra of the E_1, $E_1+\Delta_1$, and E_2 peaks of germanium. Solid curves $\underline{E} \perp \underline{\mathcal{E}}$. Dashed curves $\underline{E} \parallel \underline{\mathcal{E}}$. From Ref. 25.

Fig. 11 Electroreflectance peaks E_o and $E_o+\Delta_o$ of germanium obtained at room temperature with a very uniform surface field (as measured by the criterion of Fig. 2). The upper curve is a linear plot of the experimental data. The two lower curves are semilog plots of experimental data (solid curves) for two different surface orientations, and a theoretical fit (dashed curve). From Ref. 23.

Fig. 12 Electroreflectance structure E_1, $E_1+\Delta_1$ and E_o' of InSb, showing the various components of E_o'. The A and A' components are only observed for n-type surfaces. From Ref. 15.

Fig. 13 Reflection spectrum, linear, and quadratic electroreflectance spectra of CuCl at 85° K. From Ref. 40.

Fig. 14 Electrotransmission spectra of the n = 1 exciton of Cu_2O for the field configuration shown. The central lines are the field-induced forbidden lines (for $\underline{E} \parallel (001)$ there is also a quadrupole component). The side bands are indirect, phonon-aided lines. From Ref. 43.

Fig. 15 Position of the E_o, $E_o+\Delta_o$, E_1, $E_1+\Delta_1$, and E_2 electroreflectance peaks of germanium films as a function of the temperature of deposition. Below $\sim 200^o$ C the films are amorphous. From Ref. 46.

Fig. 16 Photoreflectance spectrum of InSb at 50^o K in the presence of a magnetic field B = 19.8 kG along the (211) direction. The dashed line gives the spectrum in zero field. From Ref. 56.

Fig. 17 Photoreflectance of the E_o edge of Ge for several values of the surface field in the darkness. From Ref. 51.

Fig. 18 Photoreflectance spectrum of the E_o peak of ultrapure GaAs for two different intensities of the modulating laser. From Ref. 58.

Fig. 19 Photoreflectance and longitudinal electroreflectance spectra of the E_o' peak of silicon showing the polarization dependence obtained for a (110) surface. From Ref. 50.

Fig. 20 Functions $\zeta_g(n)$ and $\tilde{\gamma}(n)$ which give the multiplicative correction to the exciton binding energy and the strength of the n=1 exciton in the presence of free carrier screening. The abcissa is the normalized electron density N/N_o, with $N_o \equiv 1.67\ ((\mu^2 T)/\epsilon_o) \times 10^{18}\ cm^{-3}$. The reduced mass μ is in units of the free electron mass. From Ref. 55.

Fig. 21 Experimental photoreflectance line associated with the B exciton of CdS compared with the results of a calculation based on the carrier screening mechanism. It has been assumed that the ΔN perturbation washes out completely all exciton structure with $n \geq 2$. From Ref. 55.

Fig. 22 Photoreflectance signal expected for the band edge of CdS (interband transitions) on the basis of the Burstein shift mechanism. From Ref. 54.

Fig. 23 Effect of stress on the E_o, $E_o+\Delta_o$, E_1, and $E_1+\Delta_1$ transitions of germanium. Solid line: calculations by Saravia and Brust. (From Ref. 70) Circles: electroreflectance experiments. (From Ref. 68). The gap changes are relative to the values for zero stress.

Fig. 24 Piezotransmission spectrum of AgBr at 12° K for a (111) stress. Upper curve: light polarized with E along $(1\bar{1}0)$. Lower curve: E along (111). From Ref. 60.

Fig. 25 Piezoreflectance spectra of the E_o edge of GaSb at 77° K, for (001) and (111) stress. From Ref. 59.

Fig. 26 Piezoreflectance spectra of CdS and CdSe at 77° K. For the given stress and light propagation directions difference in the intensities of A and B for both polarizations are indicative of stress-exchange splitting. From Ref. 59.

Fig. 27 Irreducible components W_1, W_3, W_5 of the piezoreflectance tensor of germanium at 300° K. The solid W_3 curve is obtained theoretically. From Ref. 62.

Fig. 28 Stress dependence of the indirect exciton energies of AlSb as a function of (111) stress for light polarized parallel (circles) and perpendicular (squares) to the stress axis. The solid points show the LA_e exciton thresholds from which the deformation potentials $\underline{a}_i$ and $\underline{d}$ have been obtained. The stress-induced splittings of the other excitons were drawn parallel to the LA_e exciton lines in order to fit the experimental points. From Ref. 73.

Fig. 29 Effect of (111) stress on the TO phonon-assisted indirect transitions of silicon for light polarized parallel and perpendicular to the stress axis and light incident on a $(11\bar{2})$ sample face. The energy difference between Λ_1 and Λ_2 gives the splitting between the $|v_1>_{111}$ and $|v_2>_{111}$ valence band states. The dotted lines represent the calculated linear shifts of the indirect transitions. The solid line was obtained theoretically taking into account the stress dependence of the spin-orbit interaction. From Ref. 73.

Fig. 30 The stress dependence of the E_1 and $E_1+\Delta_1$ optical structure of GaAs at 77° K for stress along (100). The filled (open) circles correspond to the electric field vector of the incident light polarized perpendicular (parallel) to the stress axis. From Ref. 74.

Fig. 31 Stress modulation spectrum of the x-ray emission of copper. From Ref. 76.

Fig. 32 Double beam system used for wavelength modulation spectroscopy. From Ref. 78.

Fig. 33 Arrangement used by McNatt and Handler for spatial modulation in the neighborhood of a grain boundary. From Ref. 80.

Fig. 34 Energy derivative spectrum of GaSb at 80° K (measured and calculated) compared with the corresponding thermoreflectance spectrum. From Refs. 36, 37 and 81.

Fig. 35 Deviation from linearity in the variation of the E_o gap of the GaAs - GaP system with composition. The crosses are experimental points (Ref. 87). The solid curve was calculated with Eq. (23). The dashed curve was obtained with linearly interpolated pseudopotential parameters. From Ref. 86.

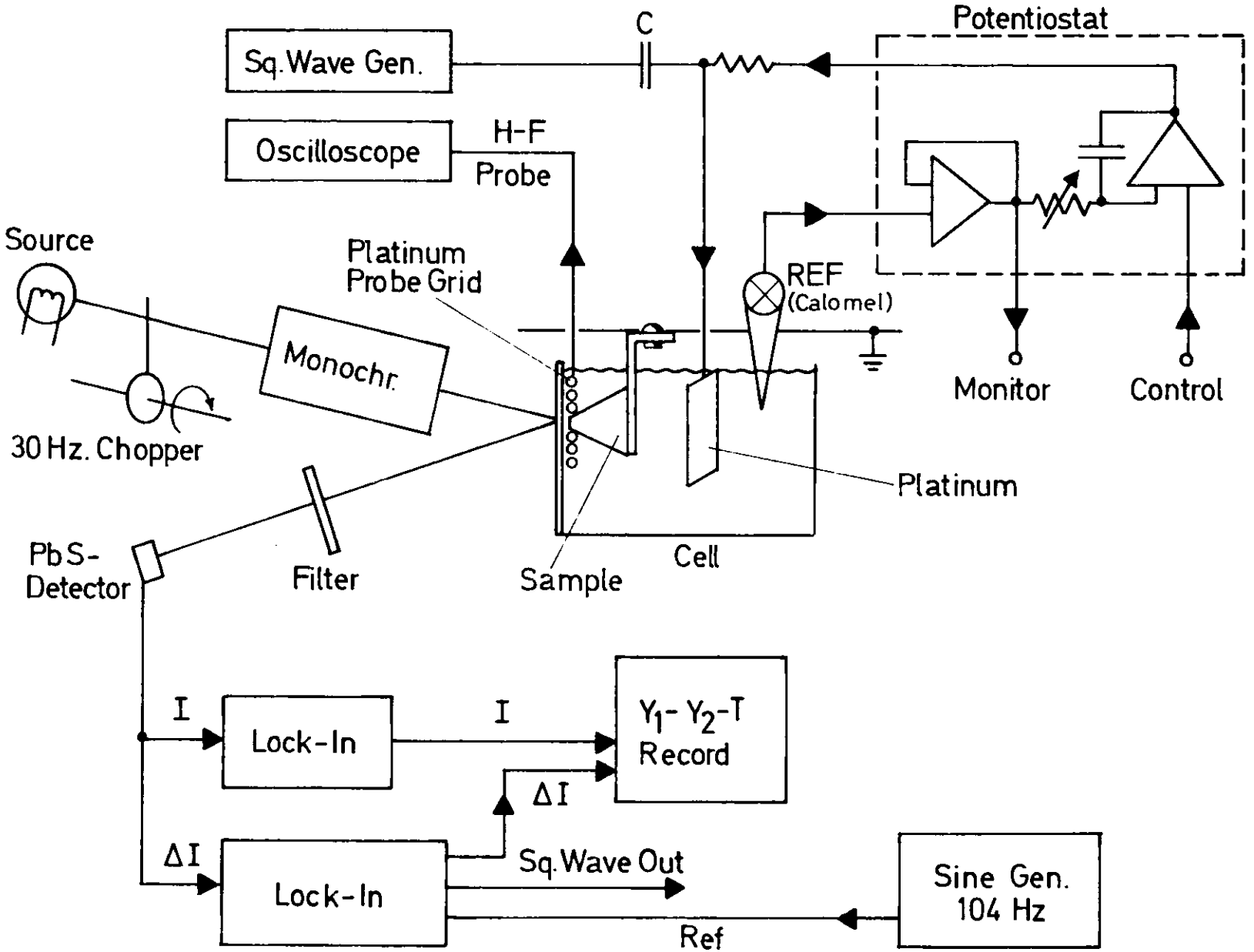
Sq. Wave Gen.
C
Potentiostat
Oscilloscope
H-F
Probe
Source
Platinum
Probe Grid
REF
(Calomel)
Monochr.
Monitor
Control
30 Hz. Chopper
Platinum
PbS-
Detector
Filter
Sample
Cell
I
Lock-In
I
Y1- Y2-T
Record
ΔI
ΔI
Lock-In
Sq. Wave Out
Sine Gen.
104 Hz
Ref

Figure 1

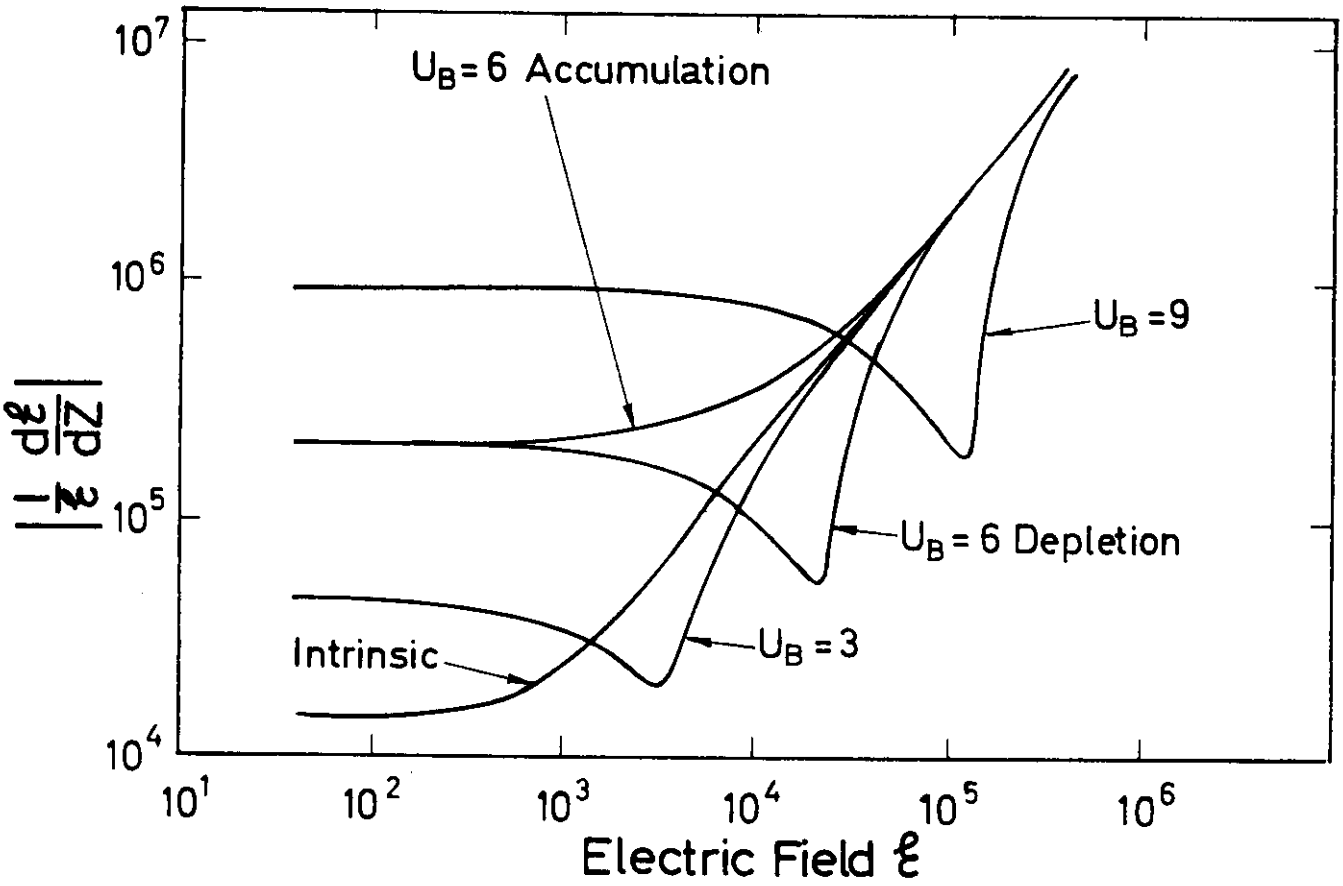
10^7
10^6
10^5
10^4
$\left|\frac{1}{2}\frac{dZp}{dZ}\right|$
$U_B = 6$ Accumulation
$U_B = 9$
$U_B = 6$ Depletion
$U_B = 3$
Intrinsic
10^1
10^2
10^3
10^4
10^5
10^6
Electric Field $\mathcal{E}$

Figure 2

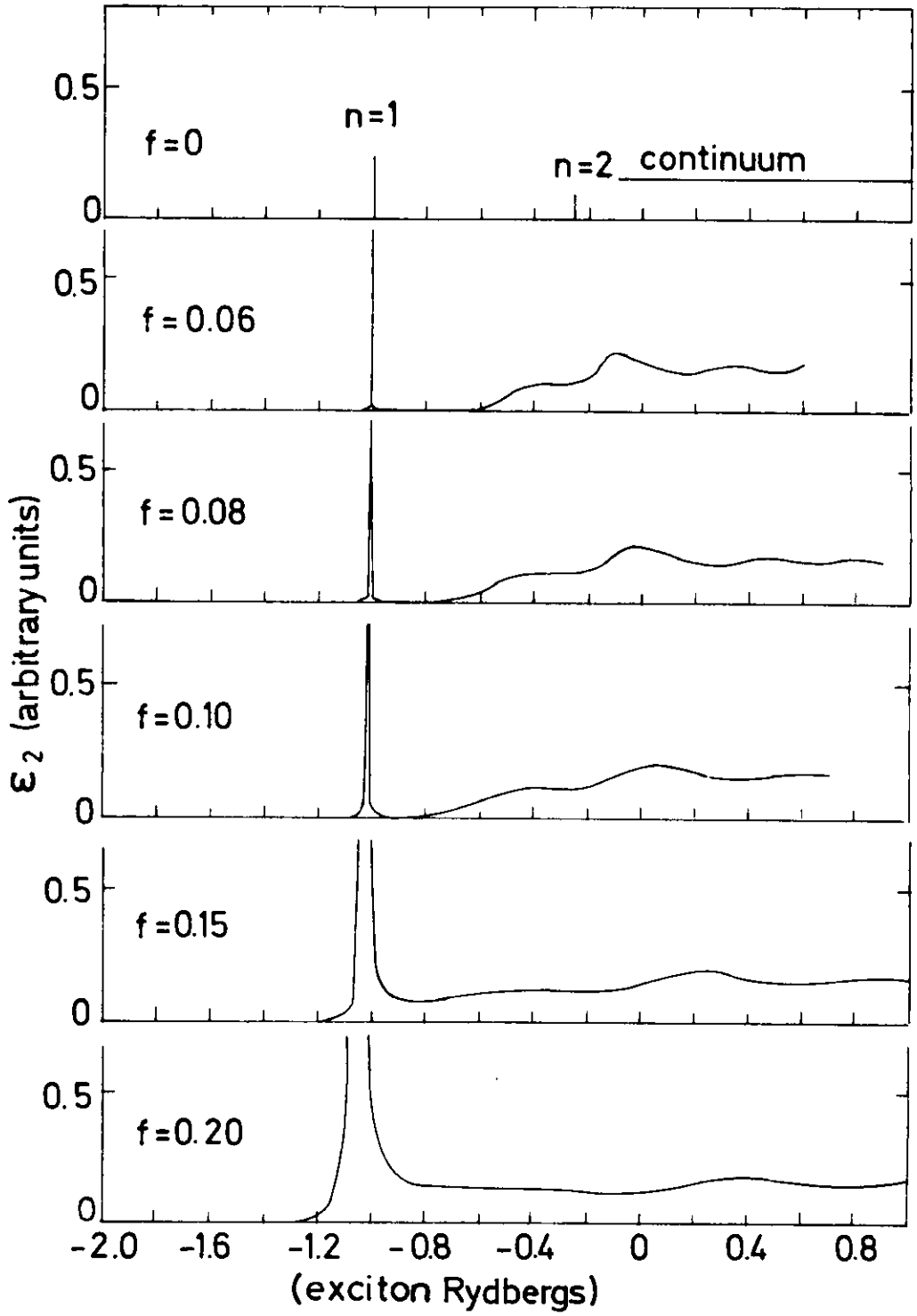
0.5
0
n=1
f=0
n=2
continuum
f=0.06
f=0.08
f=0.10
f=0.15
f=0.20
ε2 (arbitrary units)
-2.0
-1.6
-1.2
-0.8
-0.4
0
0.4
0.8
(exciton Rydbergs)

Figure 3

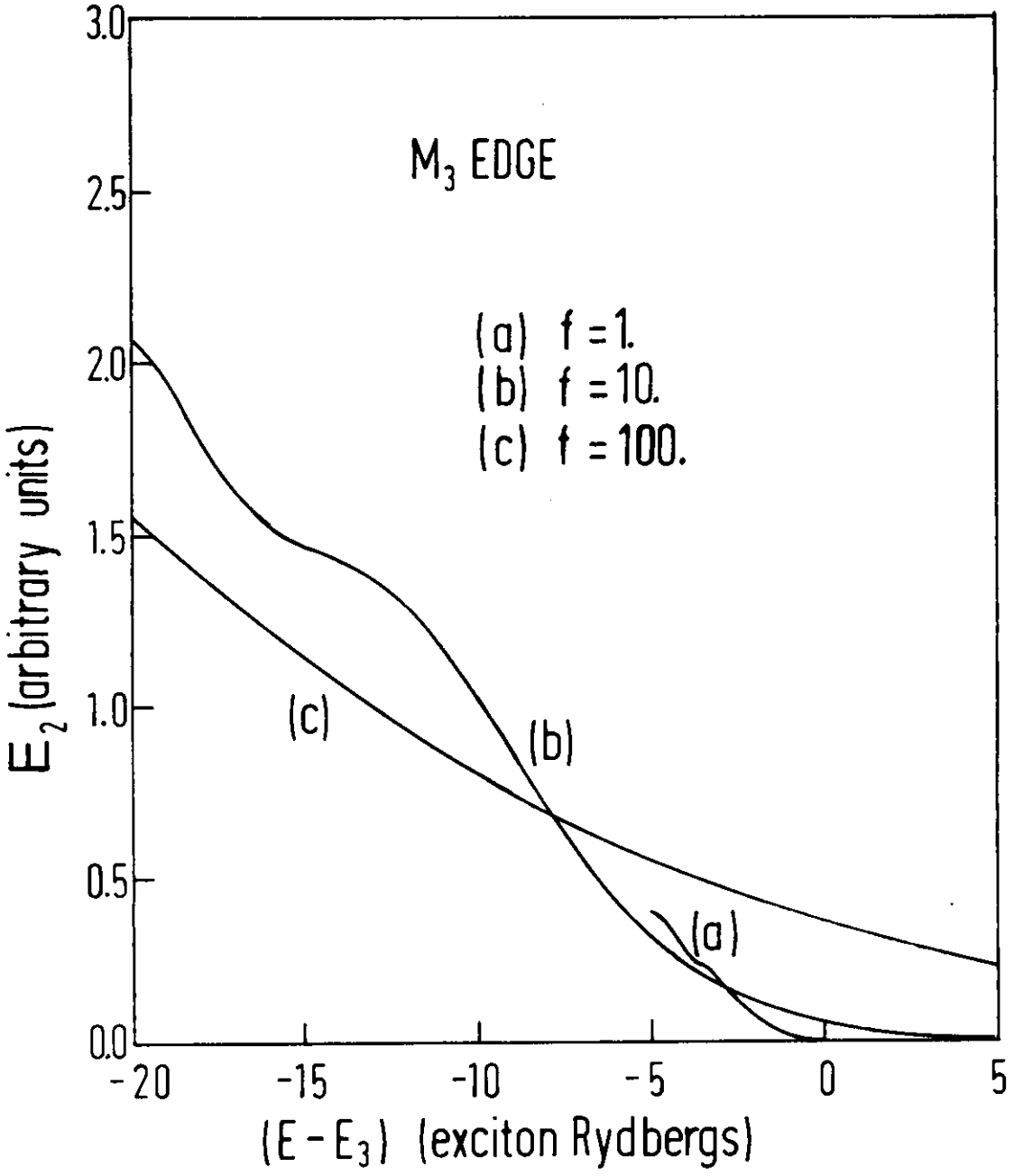
3.0
2.5
2.0
1.5
1.0
0.5
0.0
M_3 EDGE
(a) f = 1.
(b) f = 10.
(c) f = 100.
(c)
(b)
(a)
E_2 (arbitrary units)
-20
-15
-10
-5
0
5
(E - E_3) (exciton Rydbergs)

Figure 4

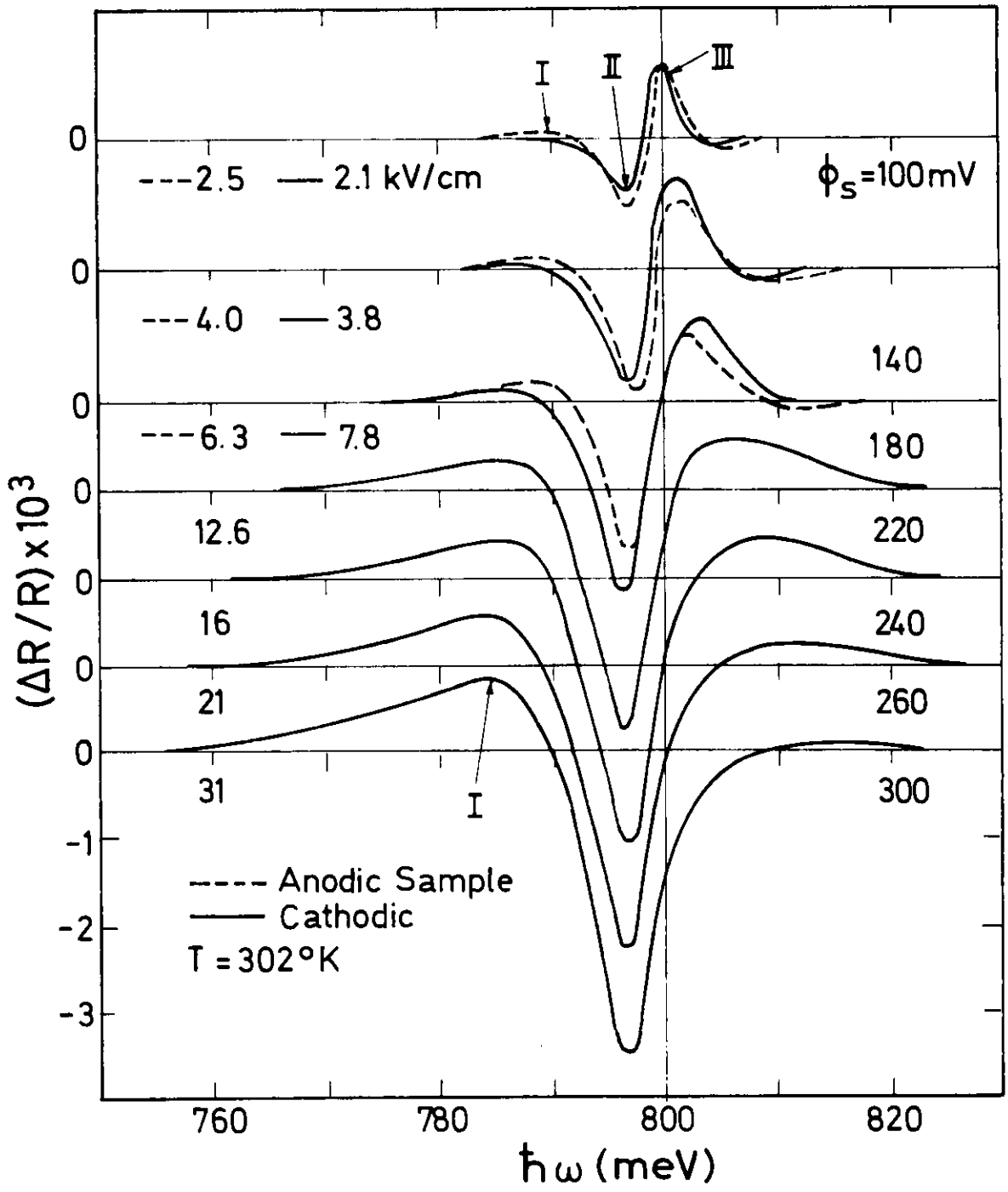
I
II
III
---2.5 — 2.1 kV/cm
ϕ_s=100mV
---4.0 — 3.8
140
---6.3 — 7.8
180
12.6
220
16
240
21
260
31
300
I
Anodic Sample
Cathodic
T = 302°K
$(\Delta R/R) \times 10^3$
$\hbar\omega$ (meV)
760
780
800
820
0
-1
-2
-3

Figure 5

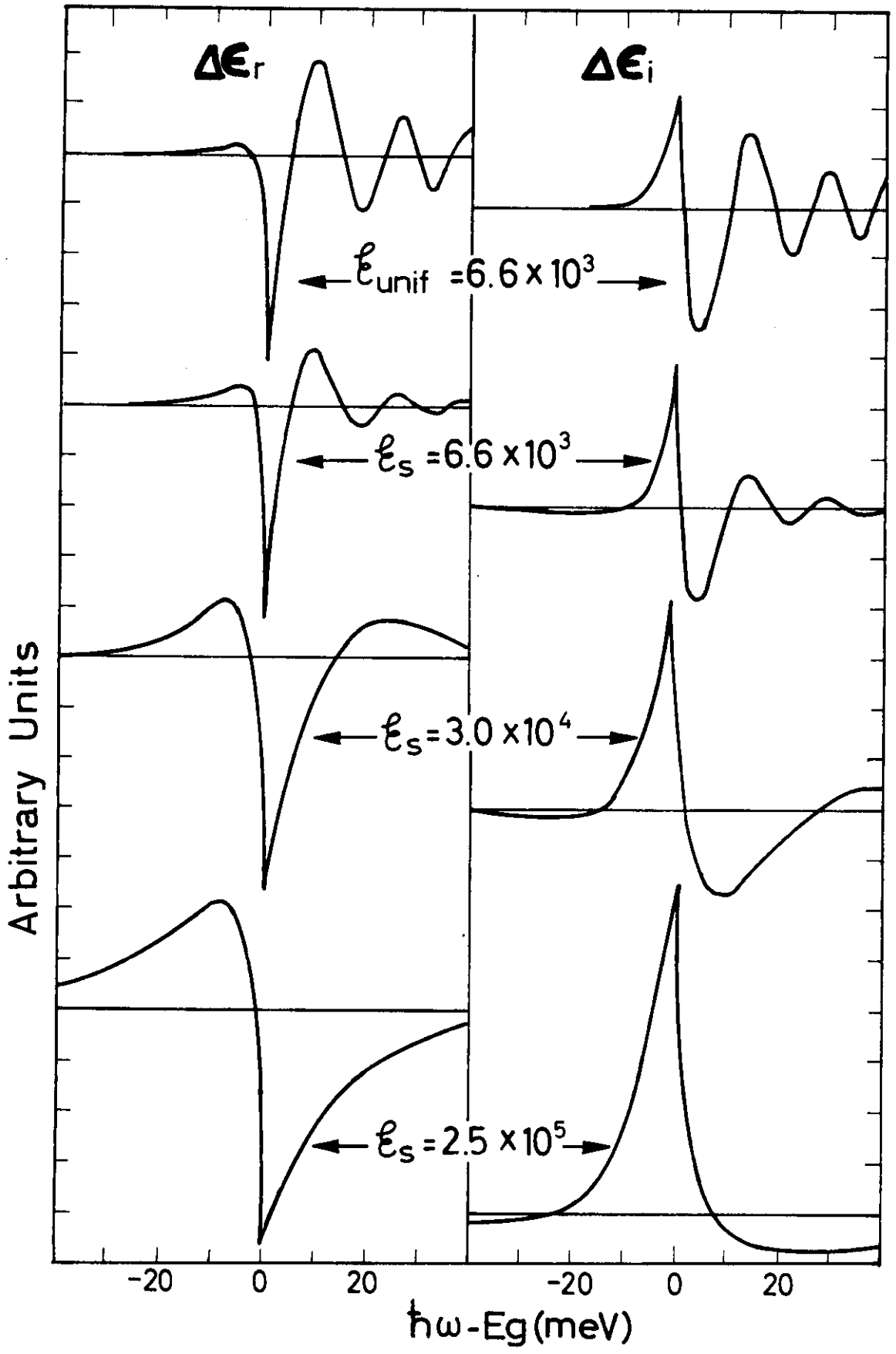
$\Delta\epsilon_r$
$\Delta\epsilon_i$
$\mathcal{E}_{unif} = 6.6 \times 10^3$
$\mathcal{E}_s = 6.6 \times 10^3$
$\mathcal{E}_s = 3.0 \times 10^4$
$\mathcal{E}_s = 2.5 \times 10^5$
Arbitrary Units
-20
0
20
-20
0
20
$\hbar\omega$-Eg (meV)

Figure 6

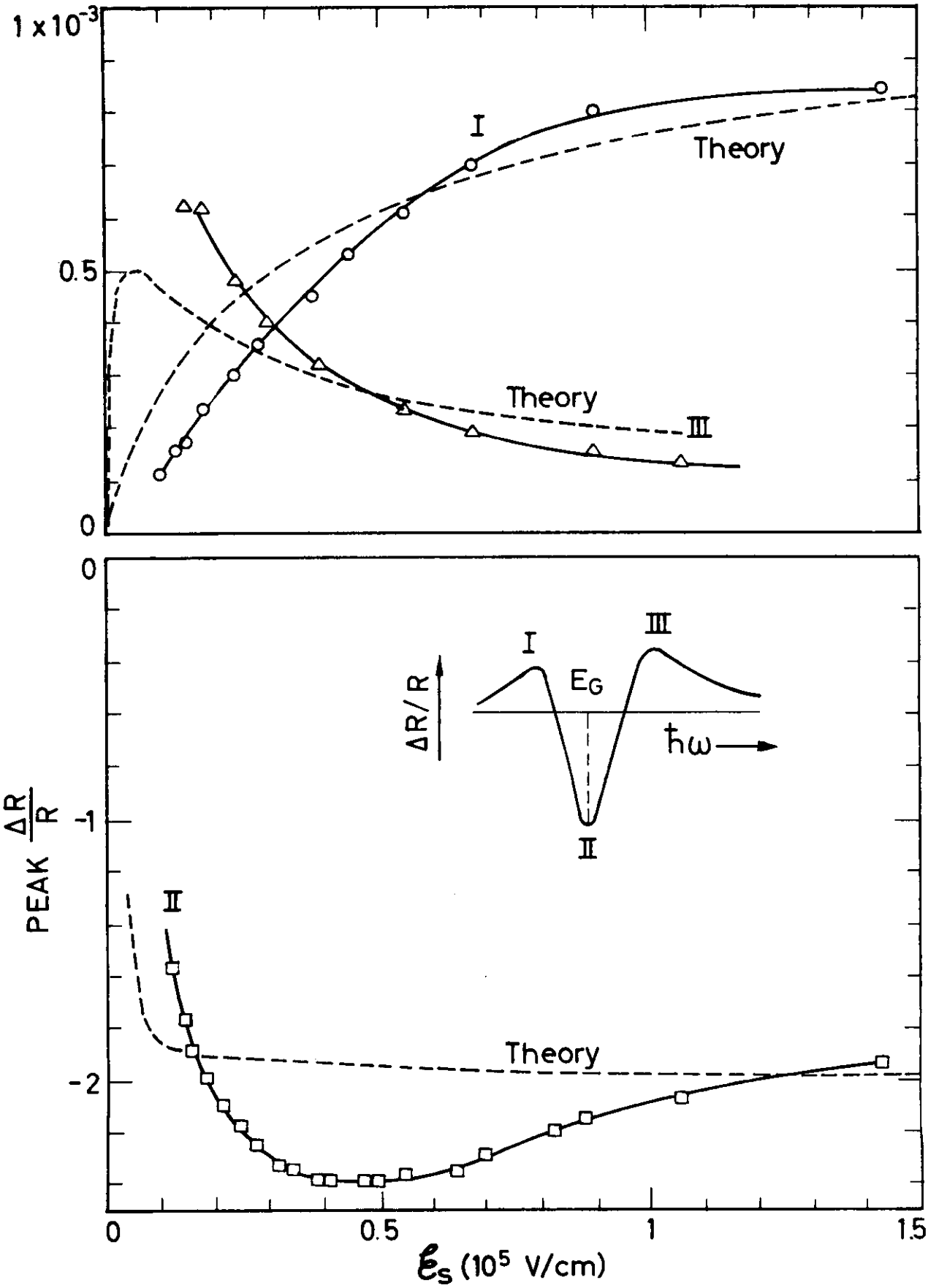
1 x 10⁻³
0.5
0
I
Theory
Theory
III
0
-1
-2
PEAK ΔR/R
ΔR/R
I
III
EG
ħω
II
II
Theory
0
0.5
1
1.5
ℰS (10⁵ V/cm)

Figure 7

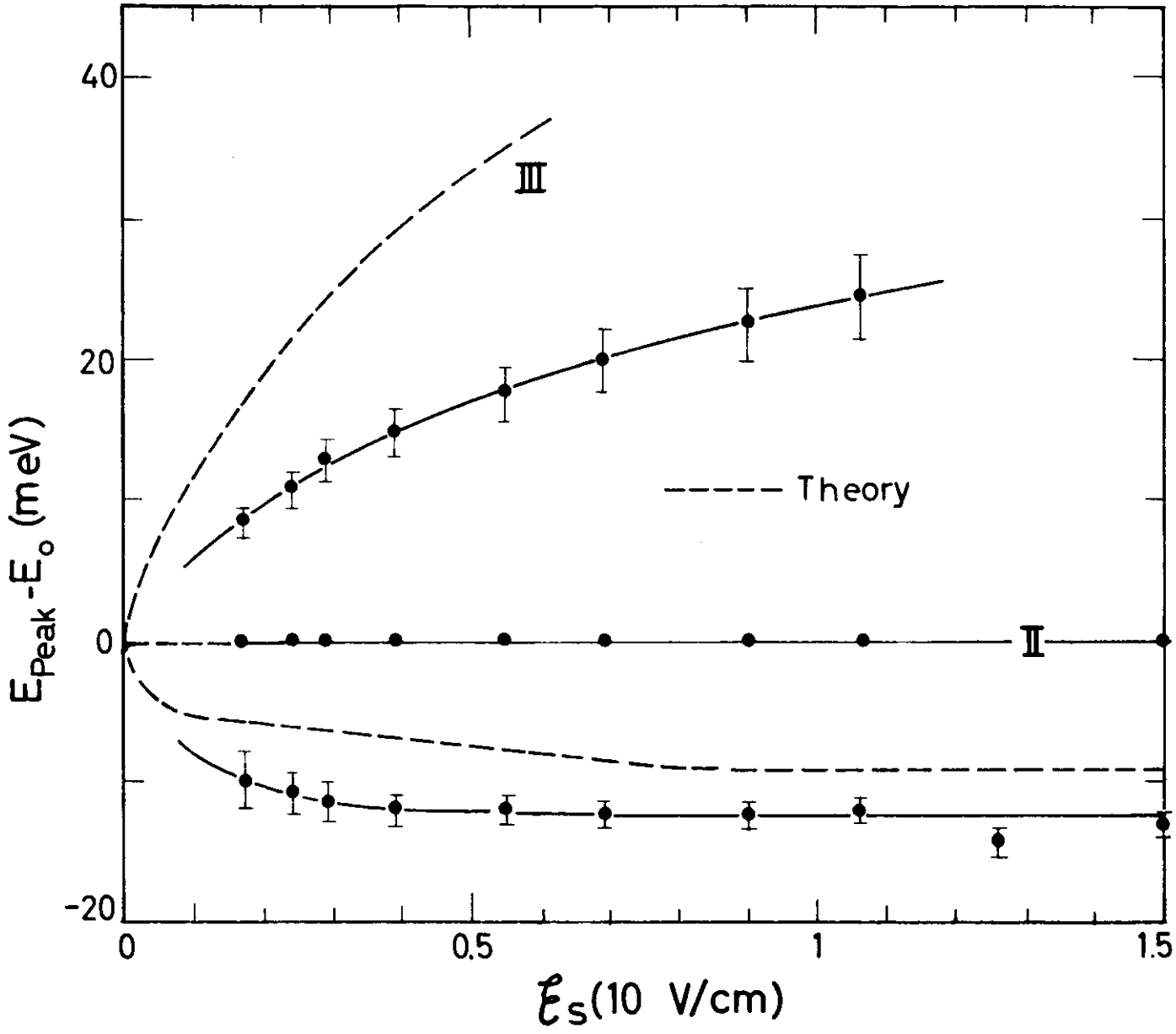

Figure 8

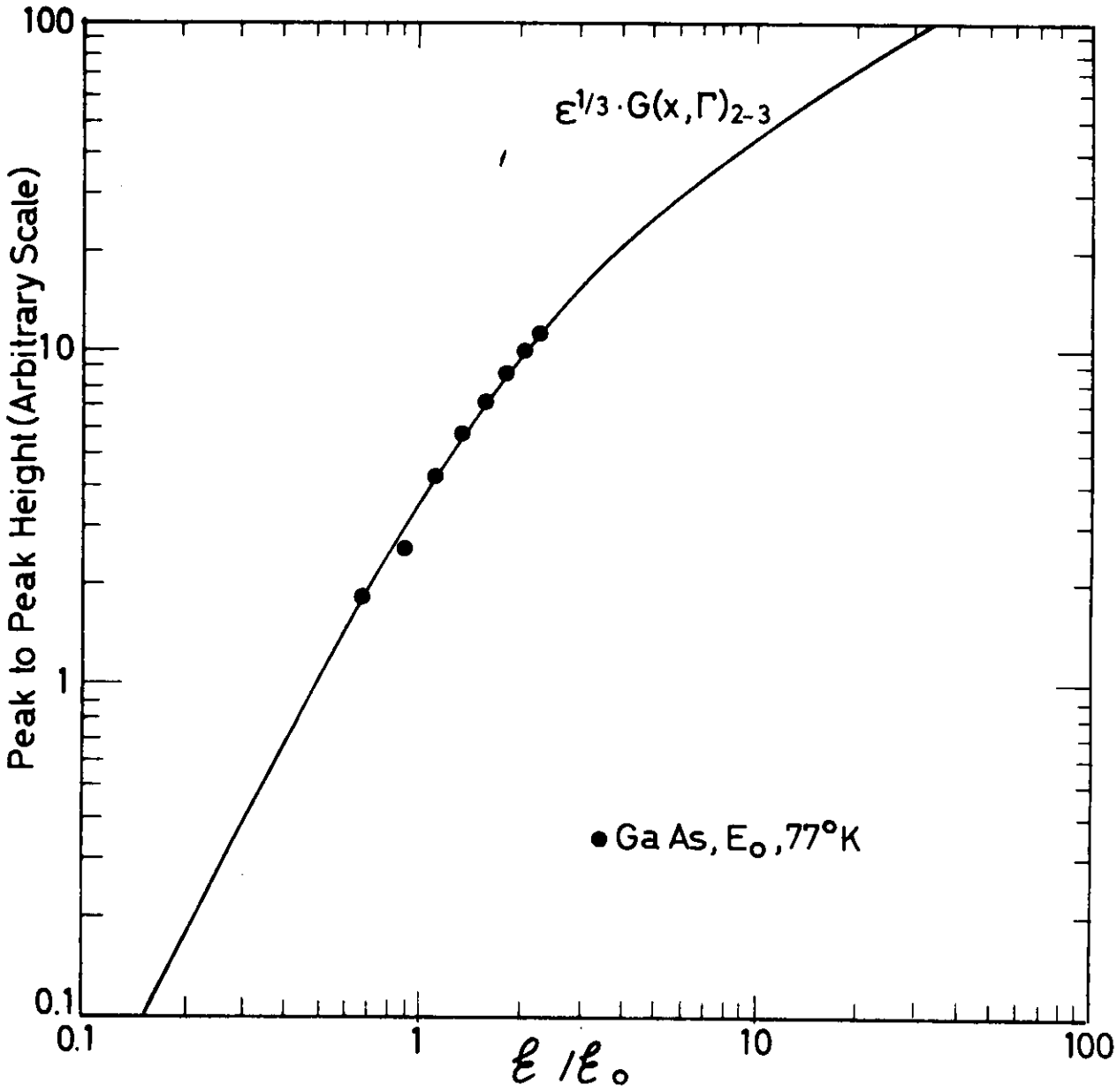
100
10
1
0.1
0.1
1
10
100
Peak to Peak Height (Arbitrary Scale)
$\mathcal{E}/\mathcal{E}_o$
$\varepsilon^{1/3} \cdot G(x,\Gamma)_{2-3}$
● Ga As, E_o, 77°K

Figure 9

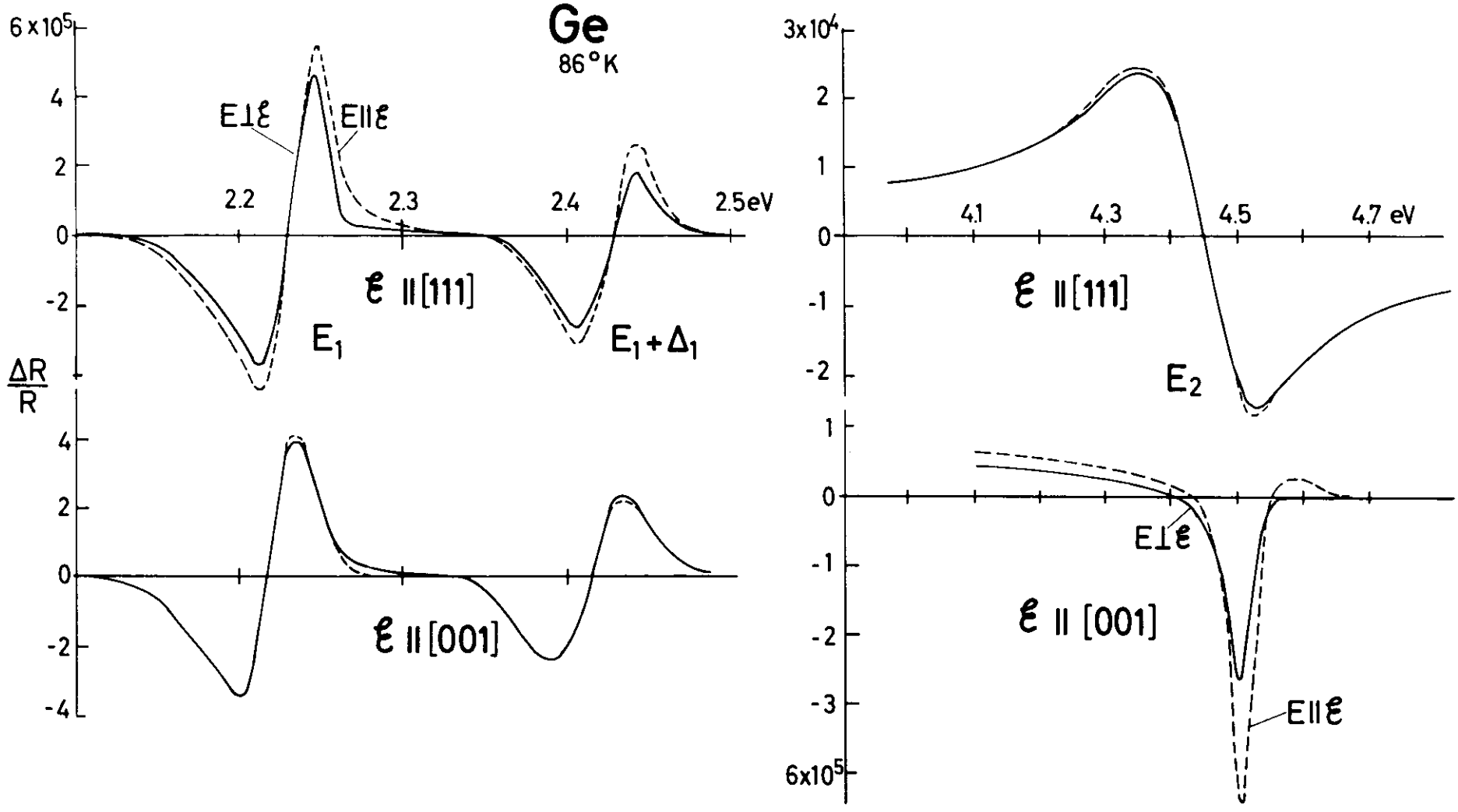
Ge
86°K
6x10^5
4
2
0
-2
ΔR/R
E⊥ε
E∥ε
2.2
2.3
2.4
2.5eV
ε ∥[111]
E1
E1+Δ1
4
2
0
-2
-4
ε ∥[001]
3x10^4
2
1
0
-1
-2
4.1
4.3
4.5
4.7 eV
ε ∥[111]
E2
1
0
-1
-2
-3
6x10^5
E⊥ε
ε ∥[001]
E∥ε

Figure 10

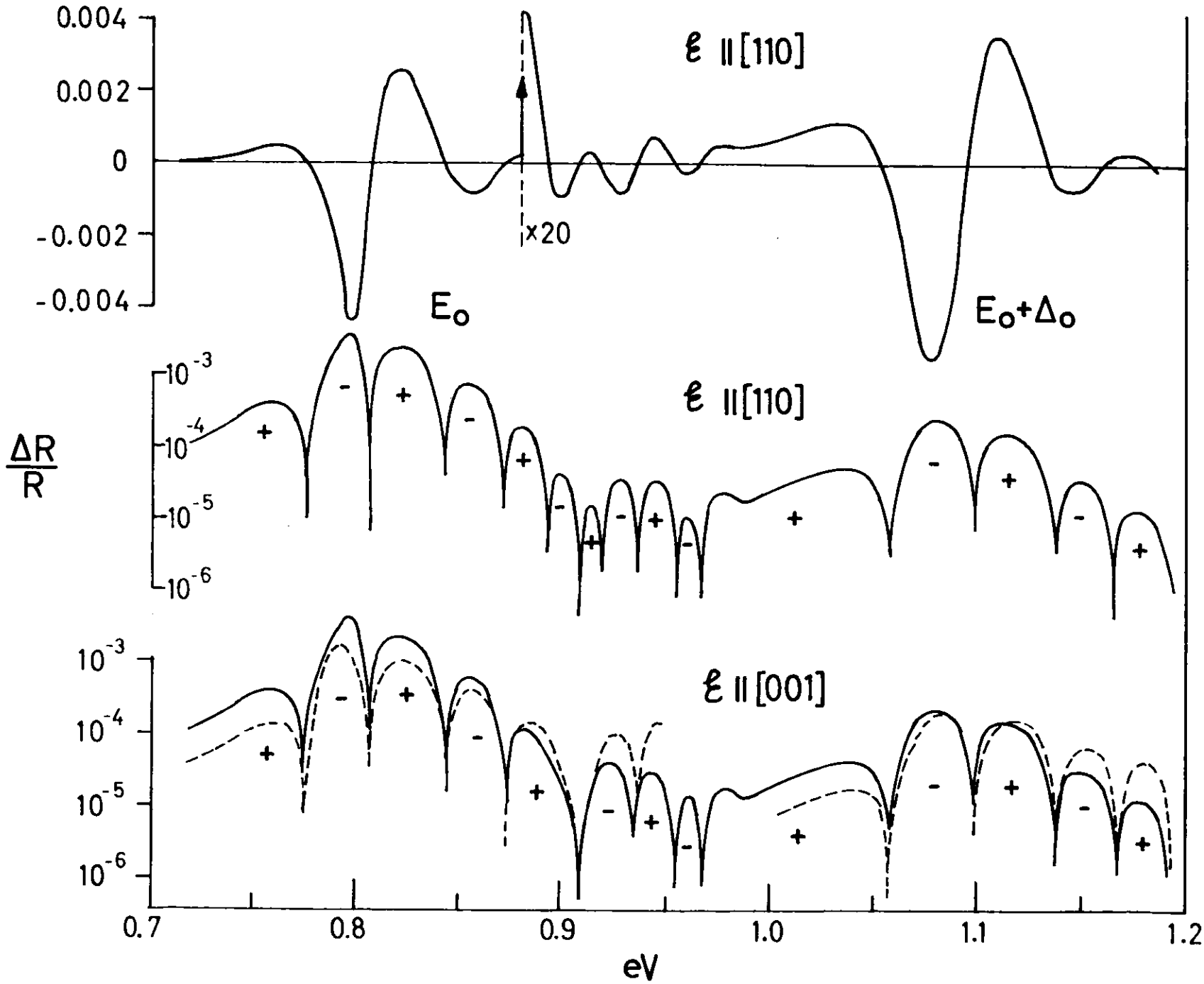
0.004
0.002
0
-0.002
-0.004
ε ∥[110]
×20
E₀
E₀+Δ₀
ΔR/R
10⁻³
10⁻⁴
10⁻⁵
10⁻⁶
ε ∥[110]
ε ∥[001]
0.7
0.8
0.9
1.0
1.1
1.2
eV

Figure 11

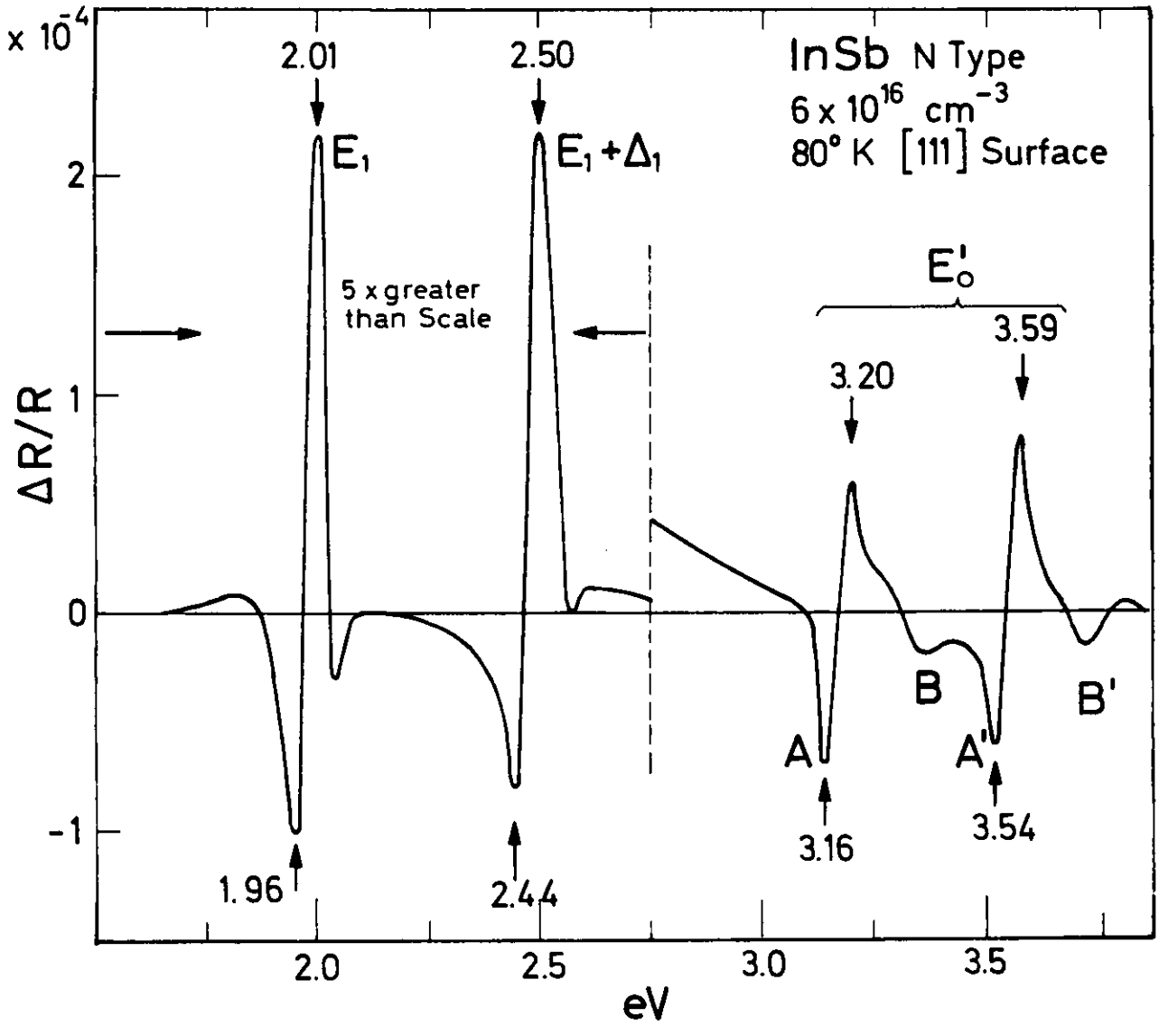
x 10⁻⁴
2.01
2.50
InSb N Type
6 x 10¹⁶ cm⁻³
80° K [111] Surface
E₁
E₁ + Δ₁
5 x greater than Scale
E'₀
3.59
3.20
2
1
0
-1
ΔR/R
B
B'
A
A'
3.16
3.54
1.96
2.44
2.0
2.5
3.0
3.5
eV

Figure 12

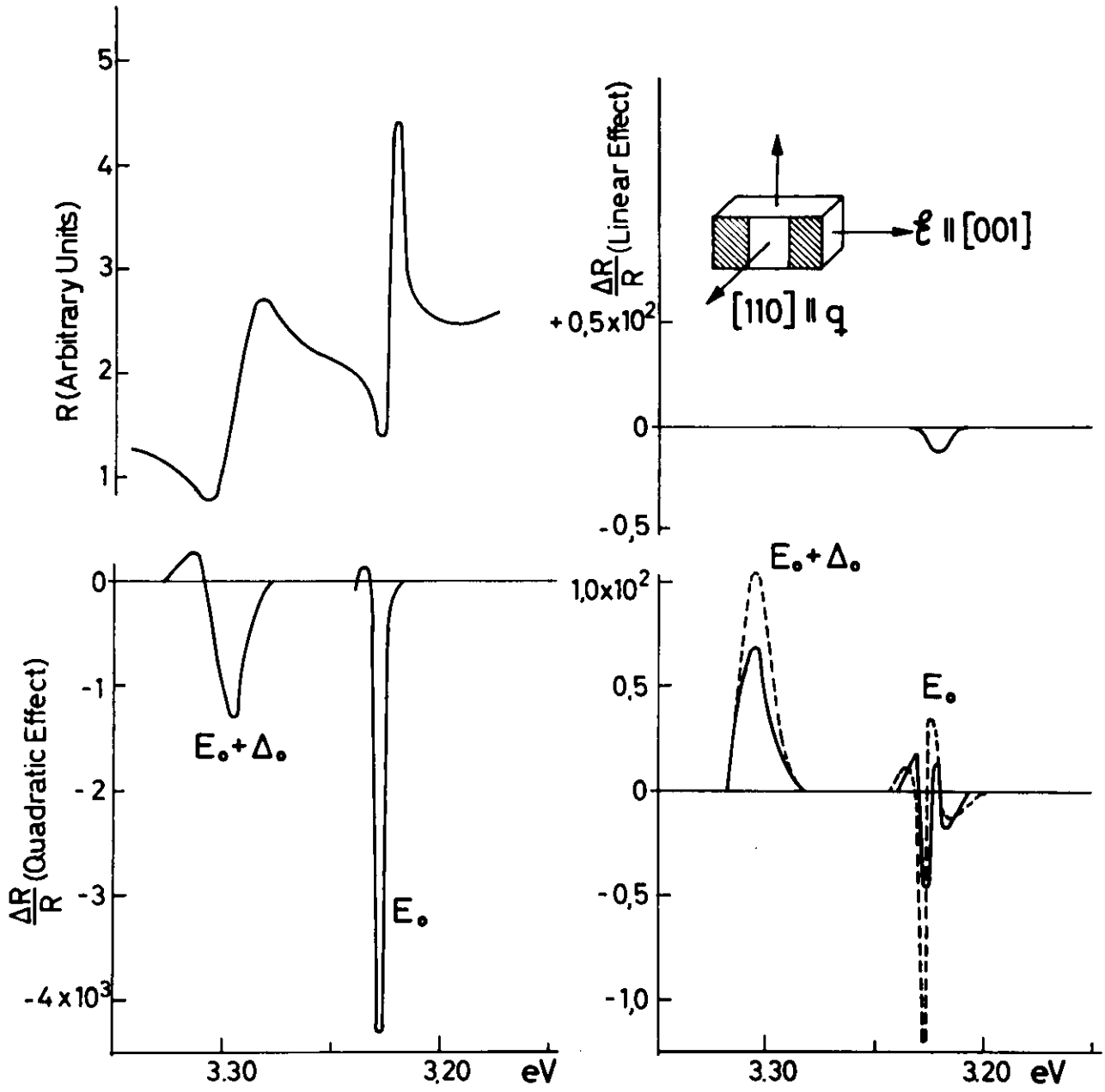
R (Arbitrary Units)
5
4
3
2
1
ΔR/R (Linear Effect)
+0,5x10²
0
-0,5
ℰ ∥ [001]
[110] ∥ q
ΔR/R (Quadratic Effect)
0
-1
-2
-3
-4x10³
E₀+Δ₀
E₀
3.30
3.20
eV
1,0x10²
0,5
0
-0,5
-1,0
E₀+Δ₀
E₀
3.30
3.20
eV

Figure 13

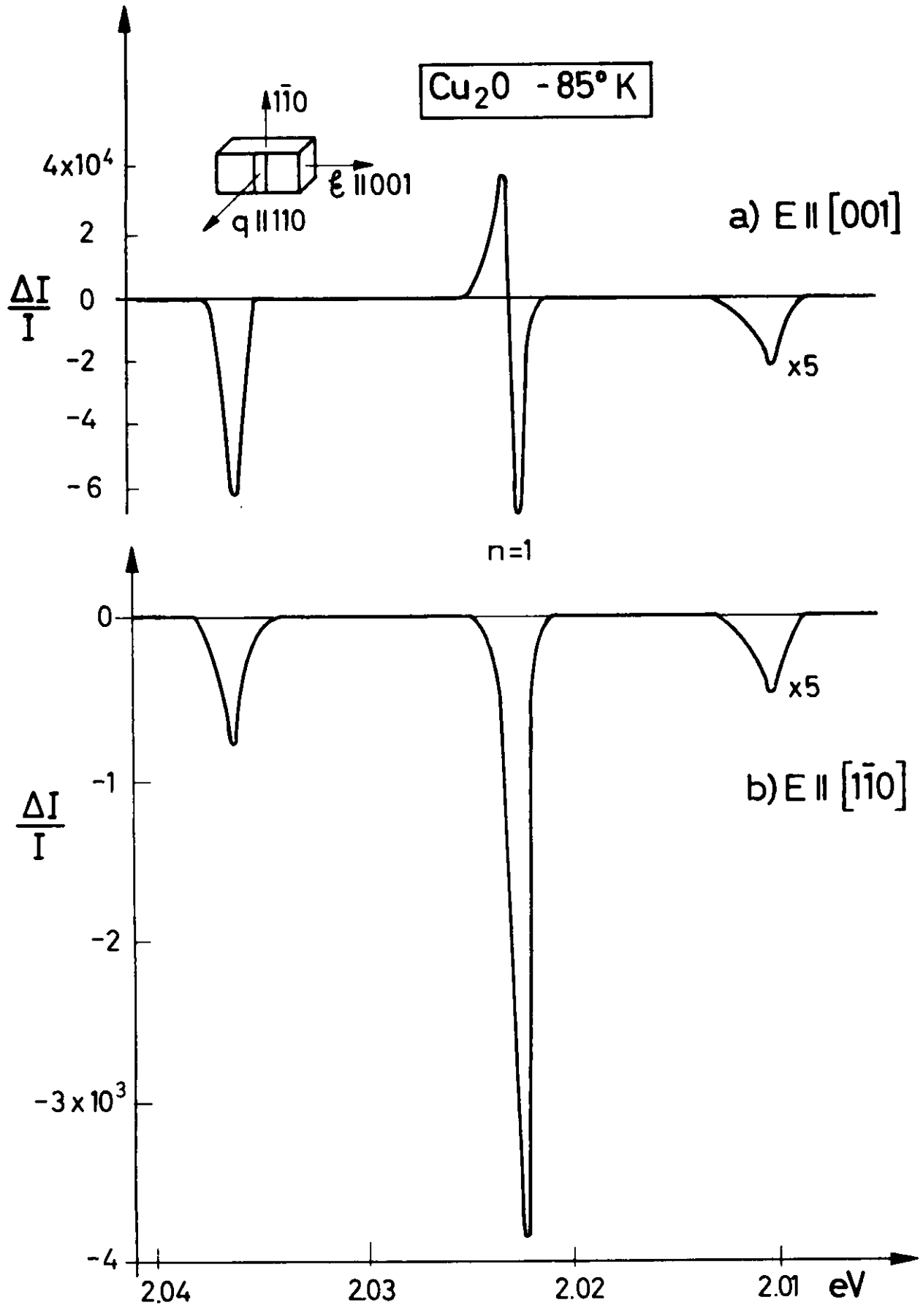
Cu2O -85° K
1̄10
ε ∥ 001
q ∥ 110
4x10⁴
2
0
-2
-4
-6
ΔI/I
a) E ∥ [001]
x5
n=1
0
-1
-2
-3x10³
-4
ΔI/I
b) E ∥ [1̄10]
x5
2.04
2.03
2.02
2.01
eV

Figure 14

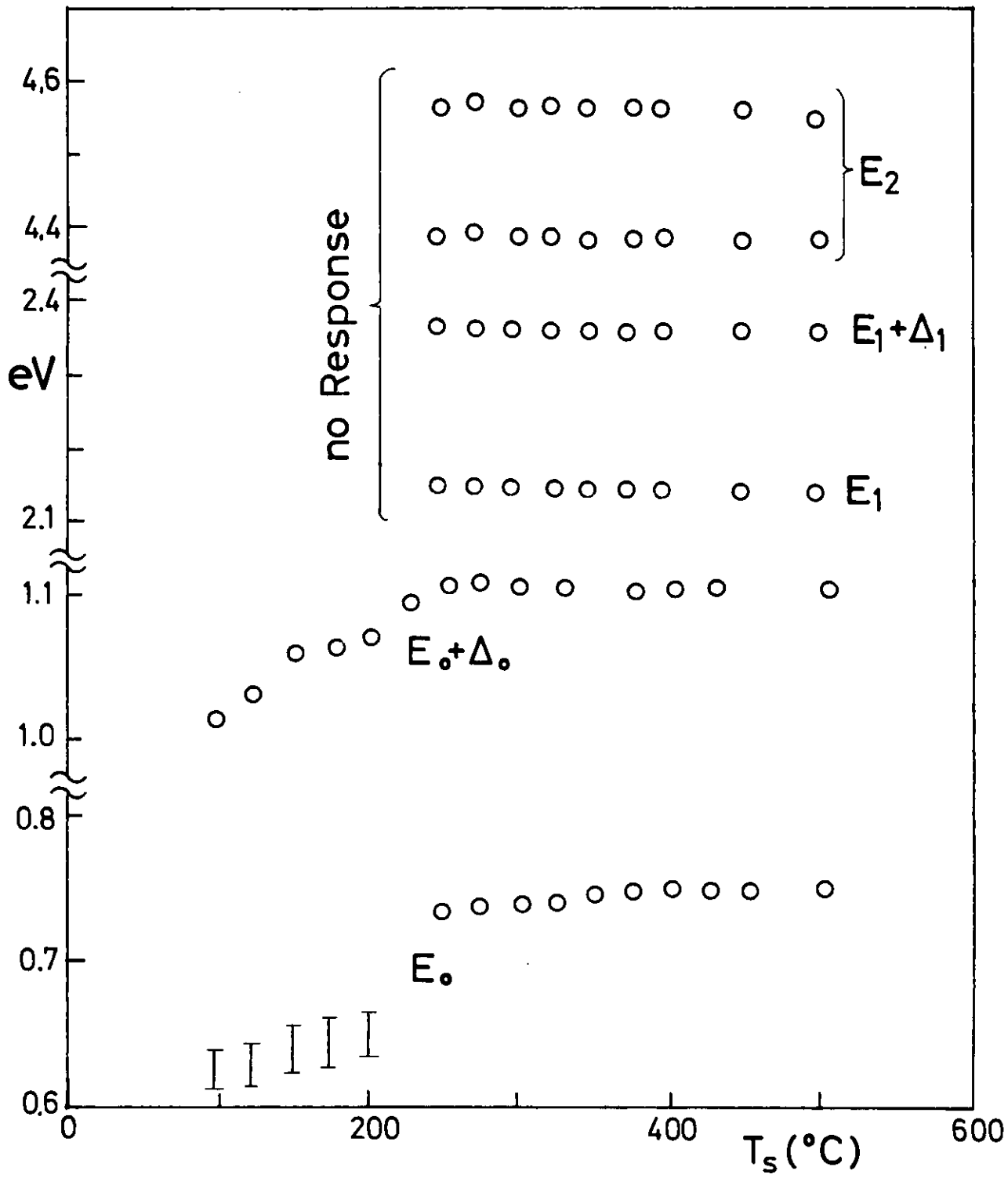
4,6
4.4
2.4
2.1
1.1
1.0
0.8
0.7
0.6
eV
0
200
400
600
T_s (°C)
no Response
E_2
$E_1+\Delta_1$
E_1
$E_o+\Delta_o$
E_o

Figure 15

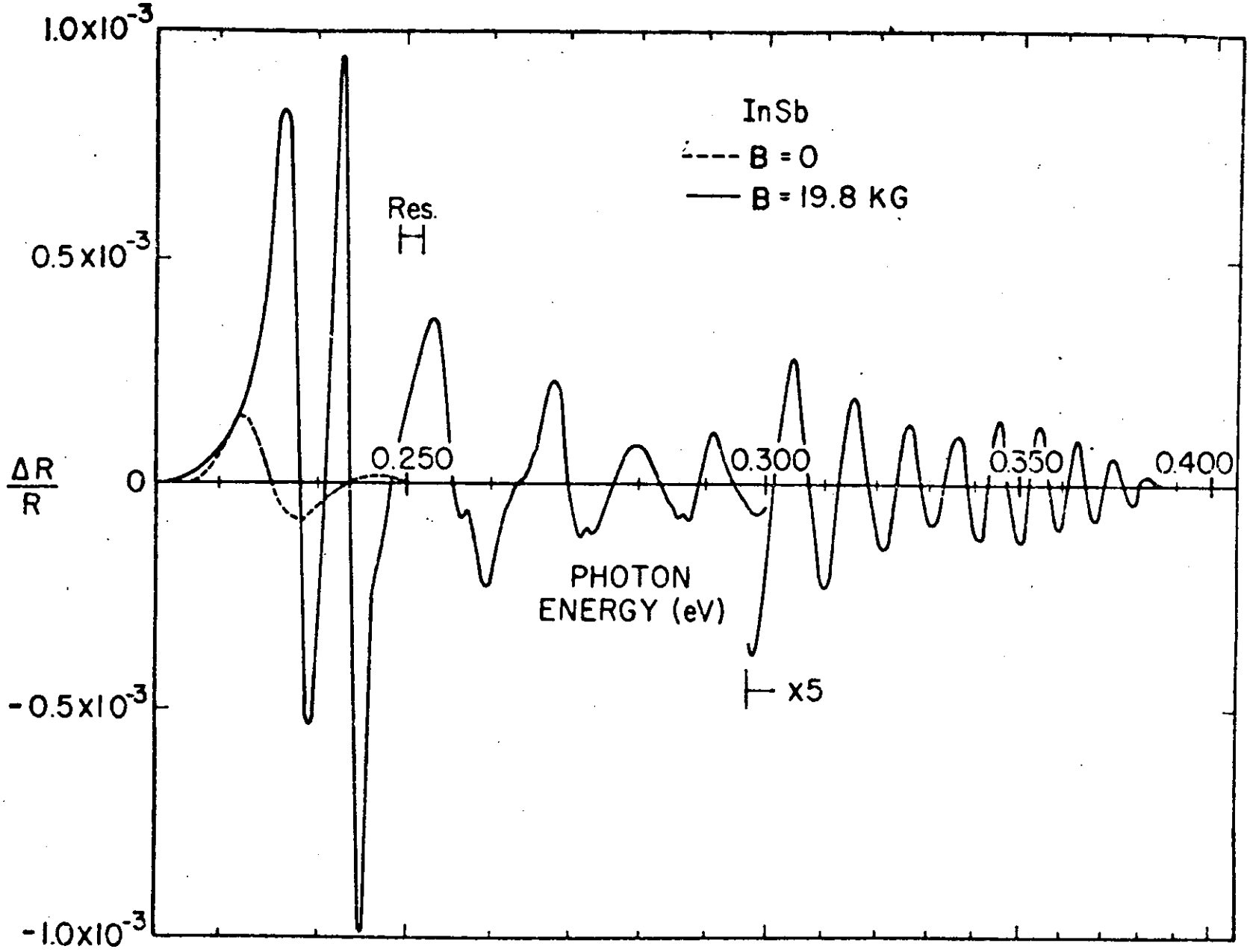
1.0x10-3
0.5x10-3
ΔR/R
0
-0.5x10-3
-1.0x10-3
InSb
B = 0
B = 19.8 KG
Res.
H
0.250
0.300
0.350
0.400
PHOTON ENERGY (eV)
x5

Figure 16

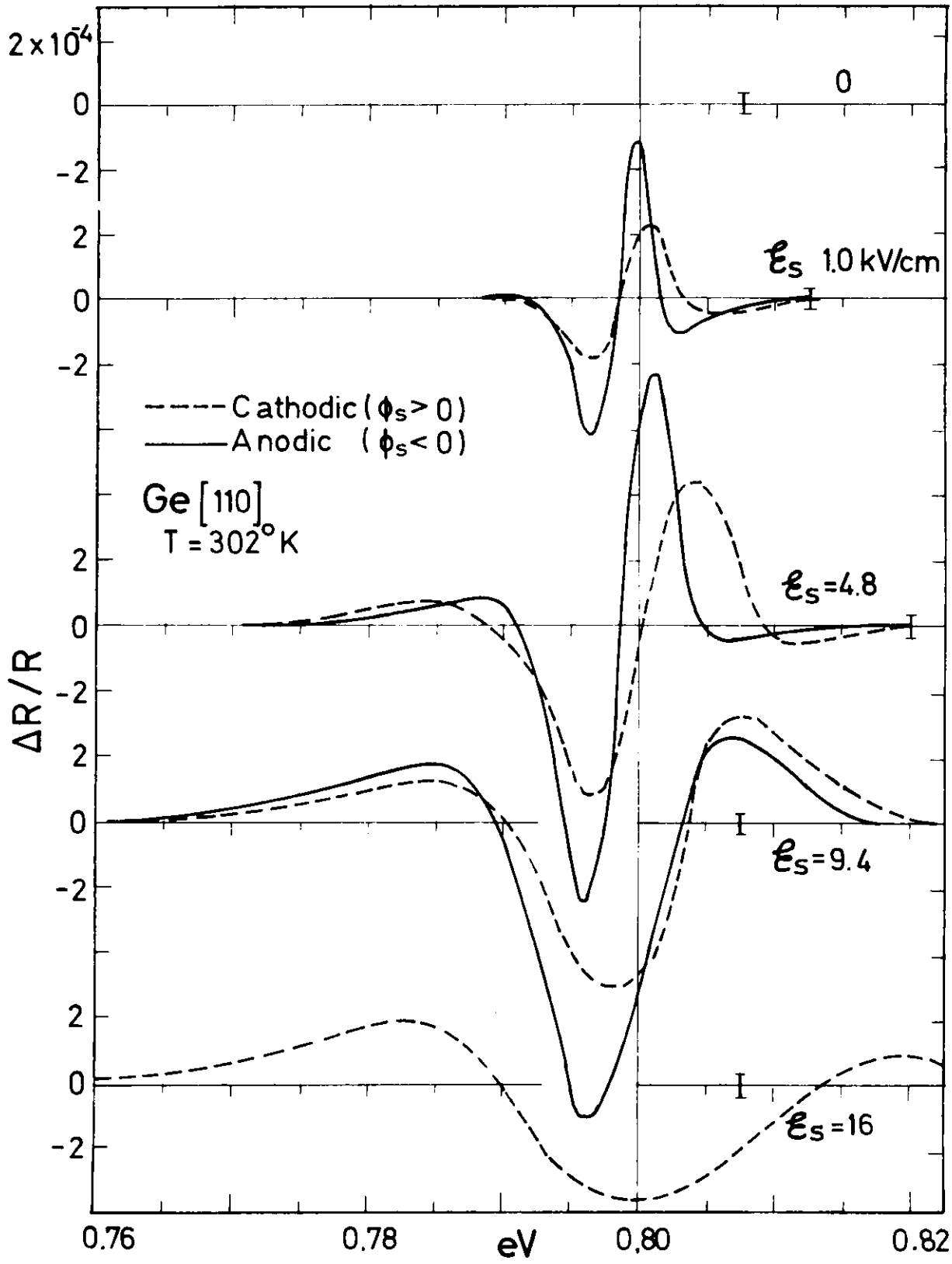
2x10⁻⁴
0
-2
2
0
-2
2
0
-2
2
0
-2
2
0
-2
0
ℰs 1.0 kV/cm
Cathodic (φs > 0)
Anodic (φs < 0)
Ge [110]
T = 302° K
ℰs=4.8
ℰs=9.4
ℰs=16
ΔR/R
0.76
0.78
eV
0.80
0.82

Figure 17

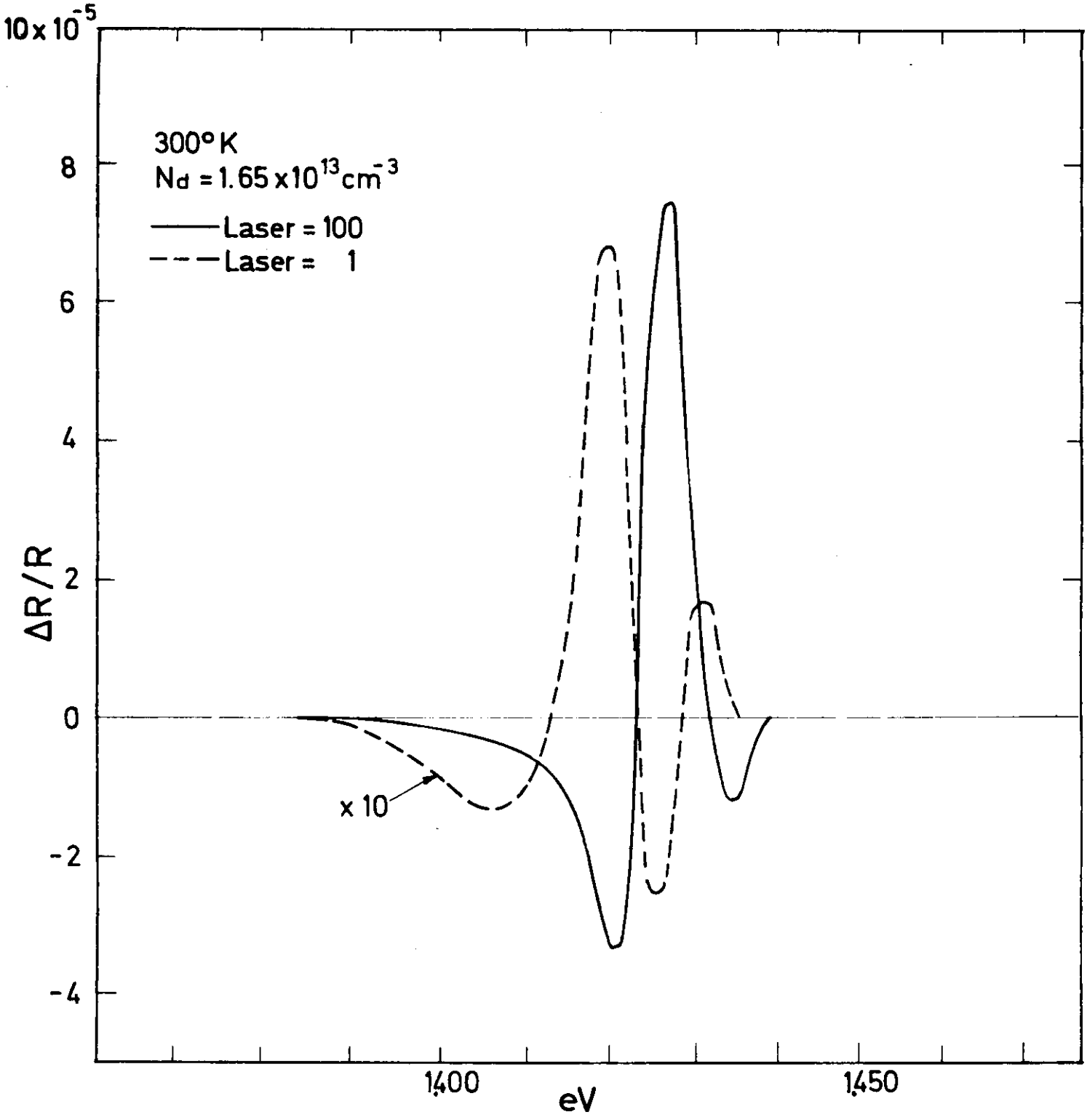
10x10⁻⁵
300°K
Nd = 1.65x10¹³cm⁻³
Laser = 100
Laser = 1
8
6
4
2
0
-2
-4
ΔR/R
x 10
1400
1450
eV

Figure 18

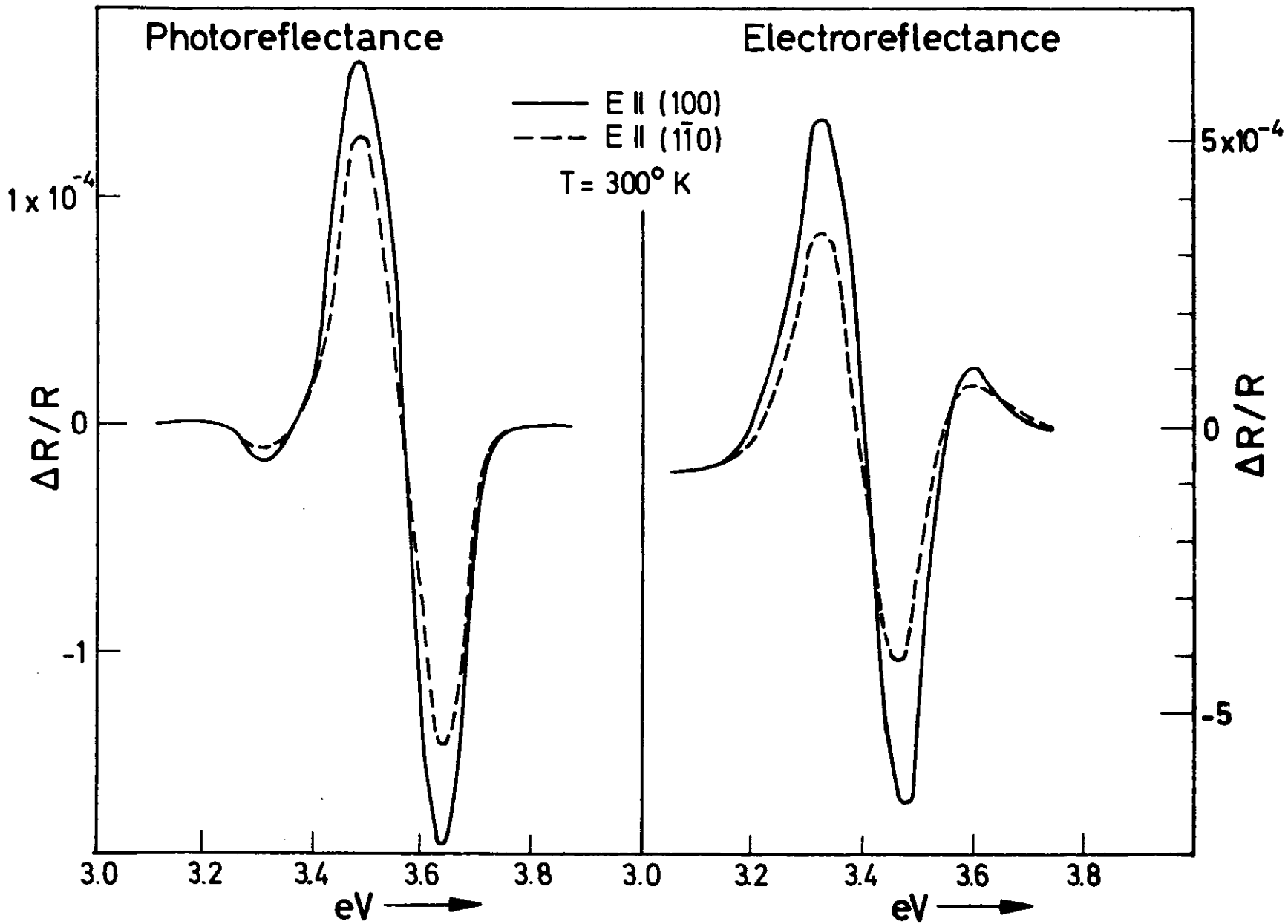
Photoreflectance
Electroreflectance
E ∥ (100)
E ∥ (1$\bar{1}$0)
T = 300° K
1 x 10^{-4}
0
-1
5x10^{-4}
0
-5
ΔR/R
ΔR/R
3.0
3.2
3.4
3.6
3.8
eV
3.0
3.2
3.4
3.6
3.8
eV

Figure 19

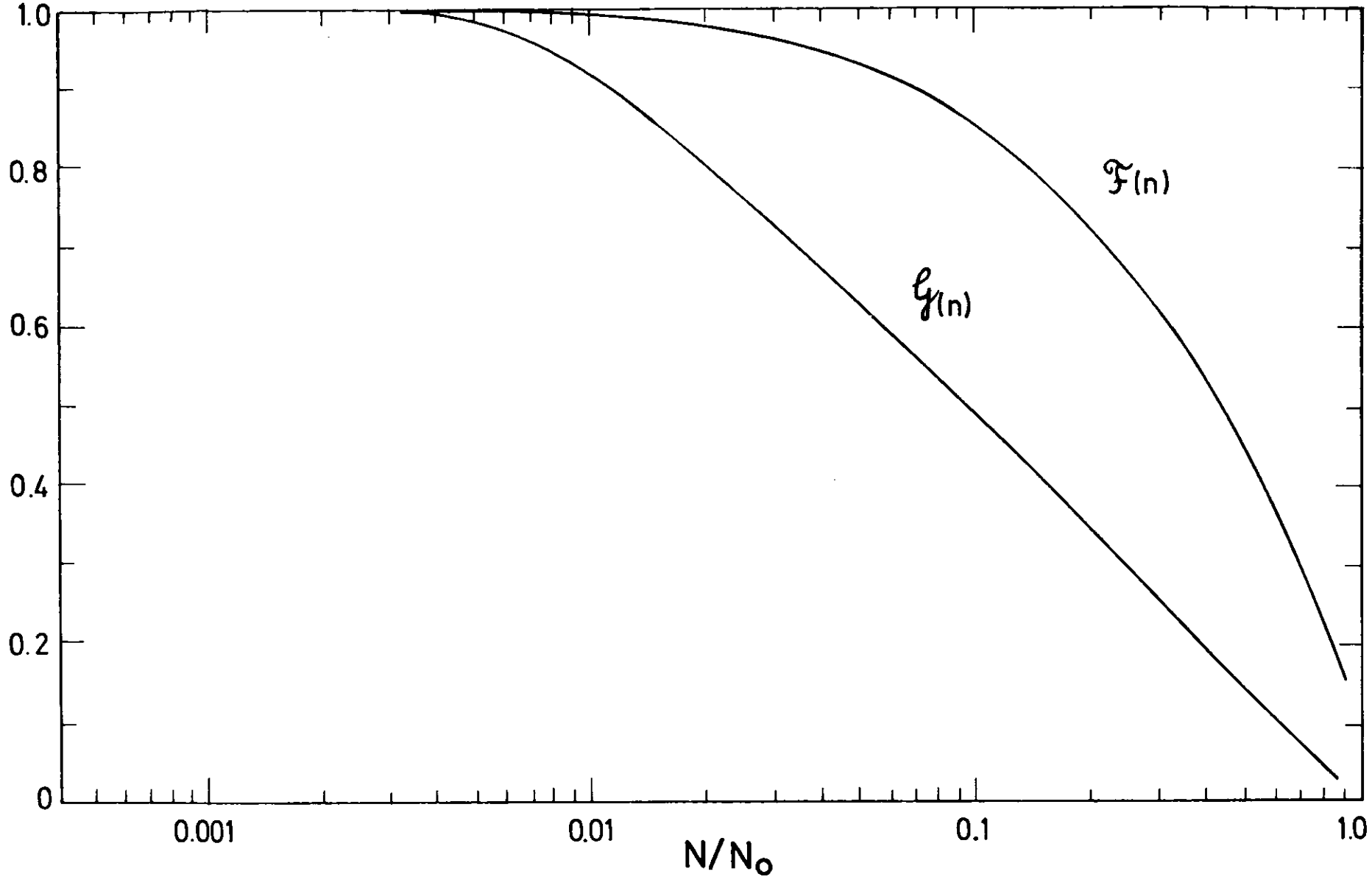

Figure 20

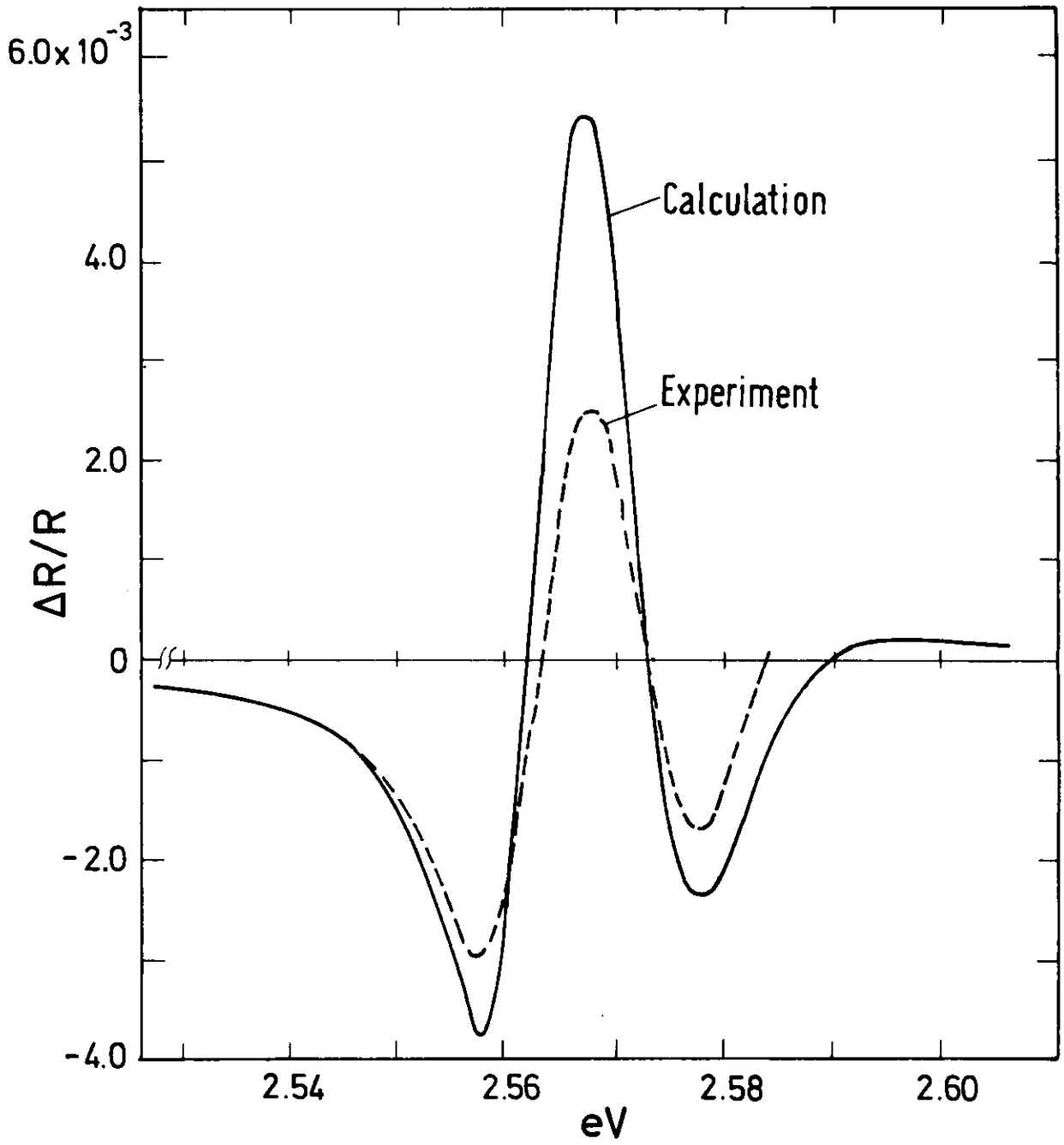
6.0x10^-3
4.0
2.0
0
-2.0
-4.0
ΔR/R
Calculation
Experiment
2.54
2.56
2.58
2.60
eV

Figure 21

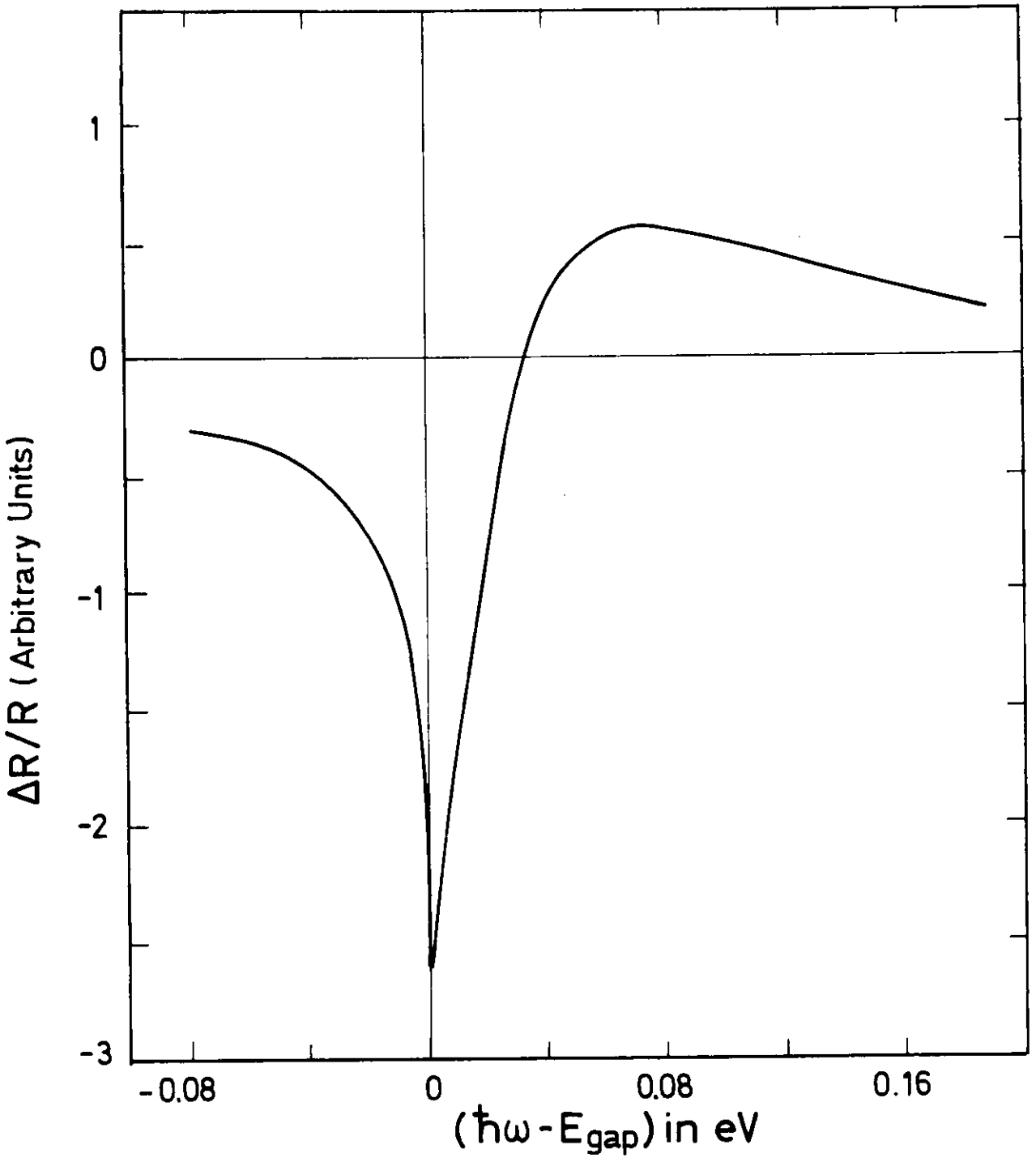

Figure 22

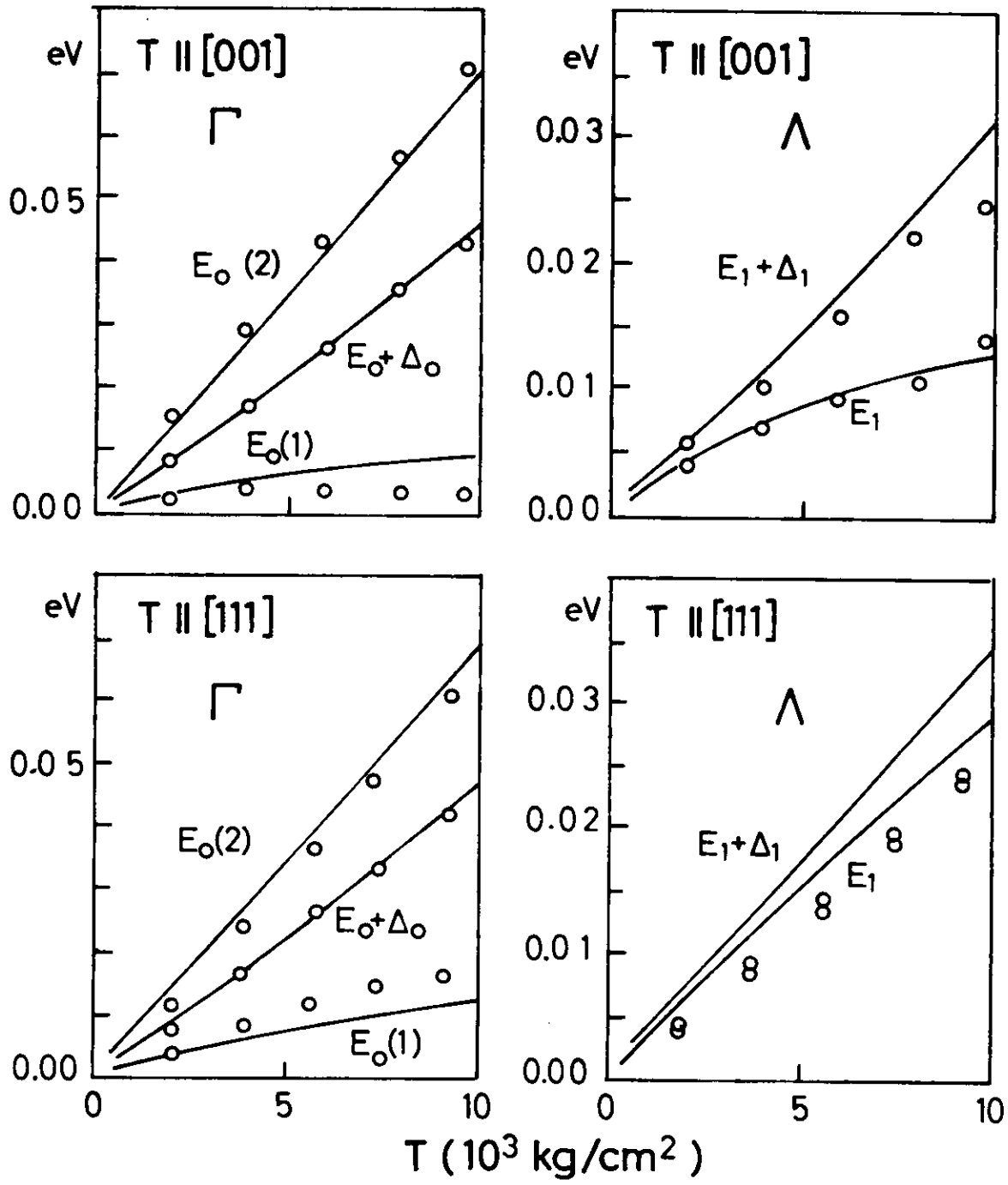
eV
T ∥ [001]
Γ
0.05
0.00
E_o (2)
$E_o+\Delta_o$
E_o(1)
eV
T ∥ [001]
Λ
0.03
0.02
0.01
0.00
$E_1+\Delta_1$
E_1
eV
T ∥ [111]
Γ
0.05
0.00
E_o(2)
$E_o+\Delta_o$
E_o(1)
0
5
10
eV
T ∥ [111]
Λ
0.03
0.02
0.01
0.00
$E_1+\Delta_1$
E_1
0
5
10
T (10^3 kg/cm^2)

Figure 23

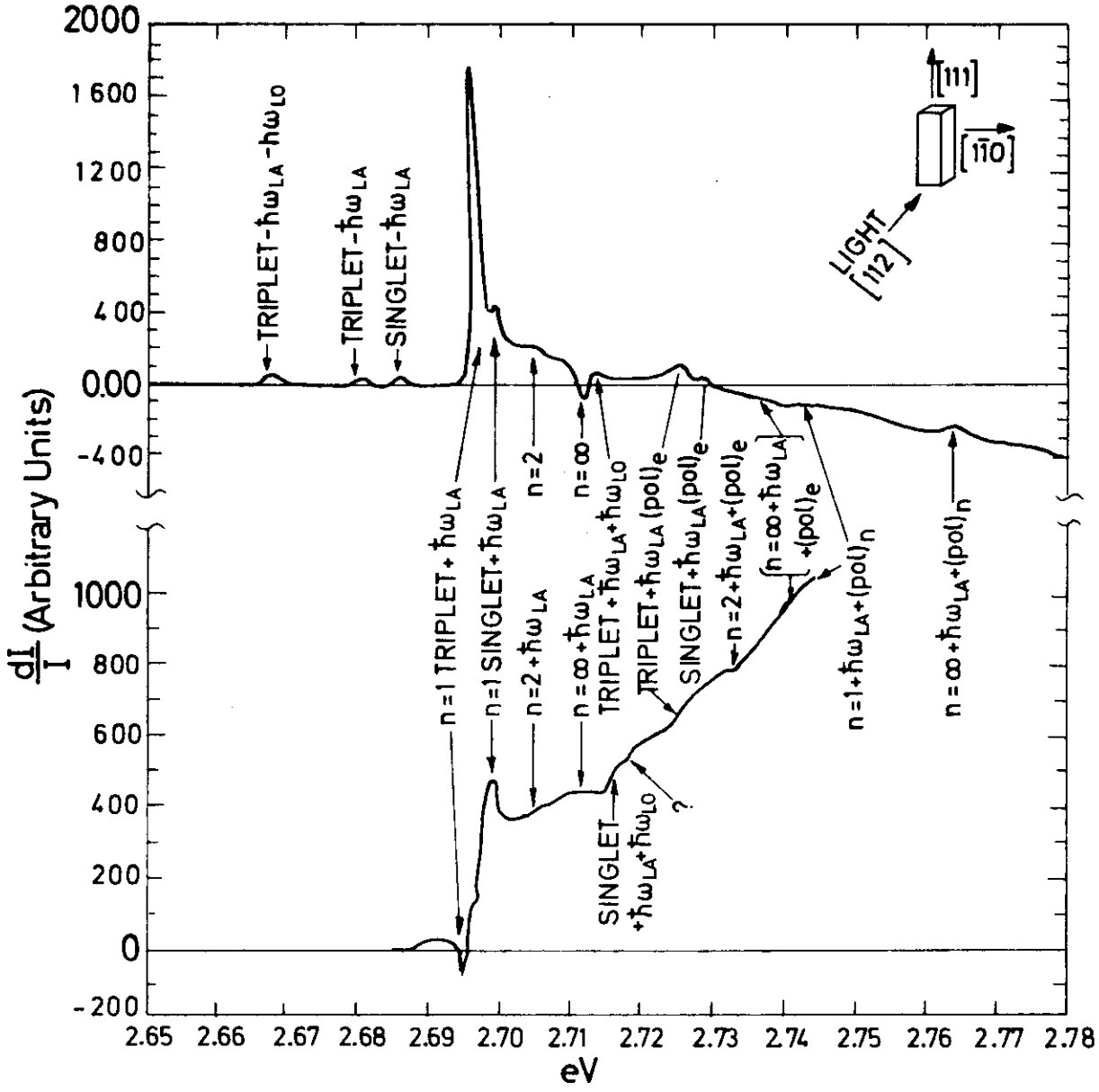
2000
1600
1200
800
400
0.00
-400
1000
800
600
400
200
0
-200
dI/I (Arbitrary Units)
2.65
2.66
2.67
2.68
2.69
2.70
2.71
2.72
2.73
2.74
2.75
2.76
2.77
2.78
eV
TRIPLET-ħω_LA-ħω_LO
TRIPLET-ħω_LA
SINGLET-ħω_LA
n=1 TRIPLET+ħω_LA
n=1 SINGLET+ħω_LA
n=2
n=∞
n=2+ħω_LA
n=∞+ħω_LA
TRIPLET+ħω_LA+ħω_LO
TRIPLET+ħω_LA(pol)_e
SINGLET+ħω_LA(pol)_e
n=2+ħω_LA+(pol)_e
(n=∞+ħω_LA
+(pol)_e
n=1+ħω_LA+(pol)_n
n=∞+ħω_LA+(pol)_n
SINGLET
+ħω_LA+ħω_LO
?
[111]
[1̄10]
LIGHT
[112]

Figure 24

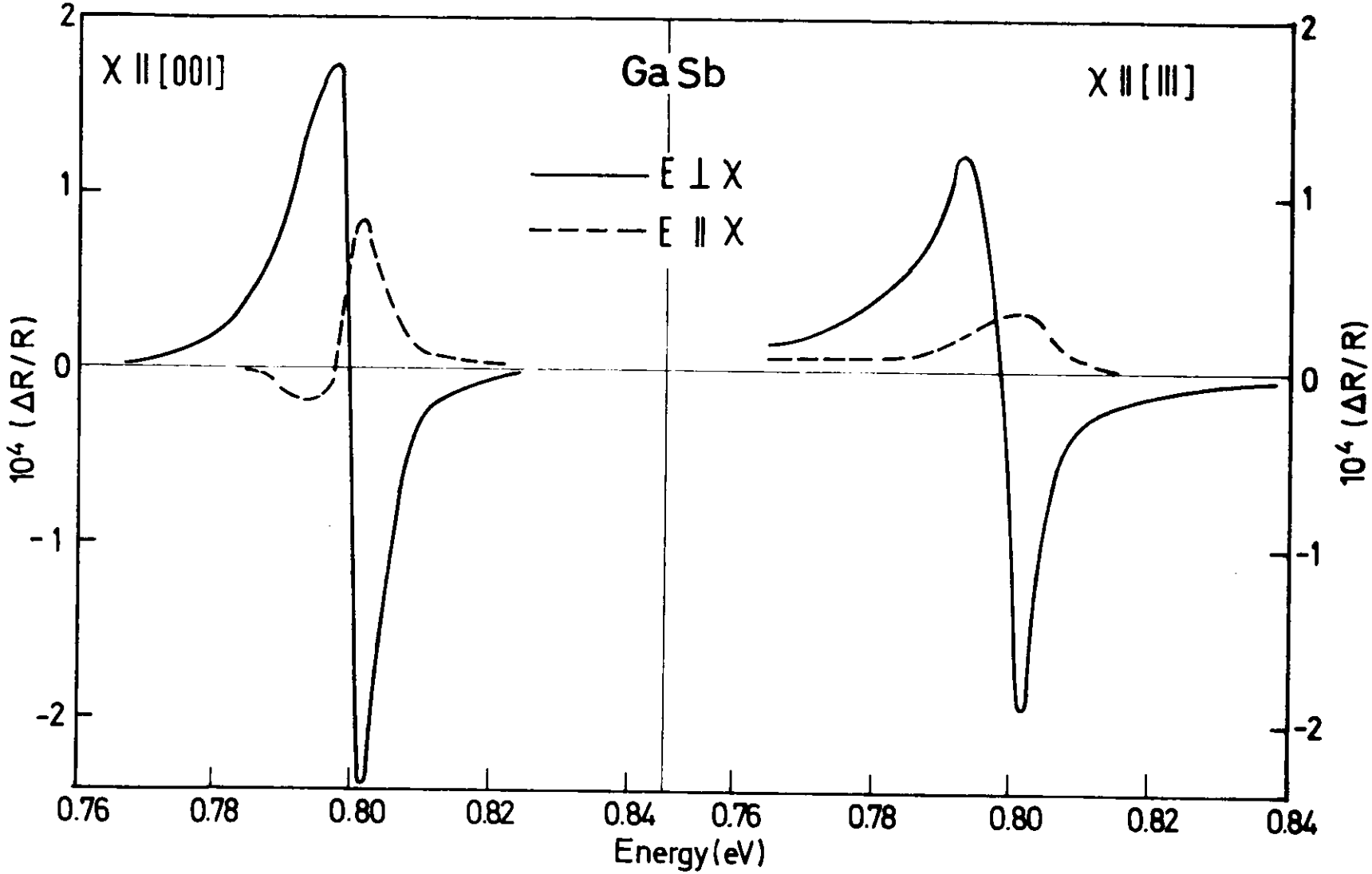
X ∥ [001]
Ga Sb
X ∥ [111]
E ⊥ X
E ∥ X
10⁴ (ΔR/R)
Energy (eV)
2
1
0
-1
-2
0.76
0.78
0.80
0.82
0.84

Figure 25

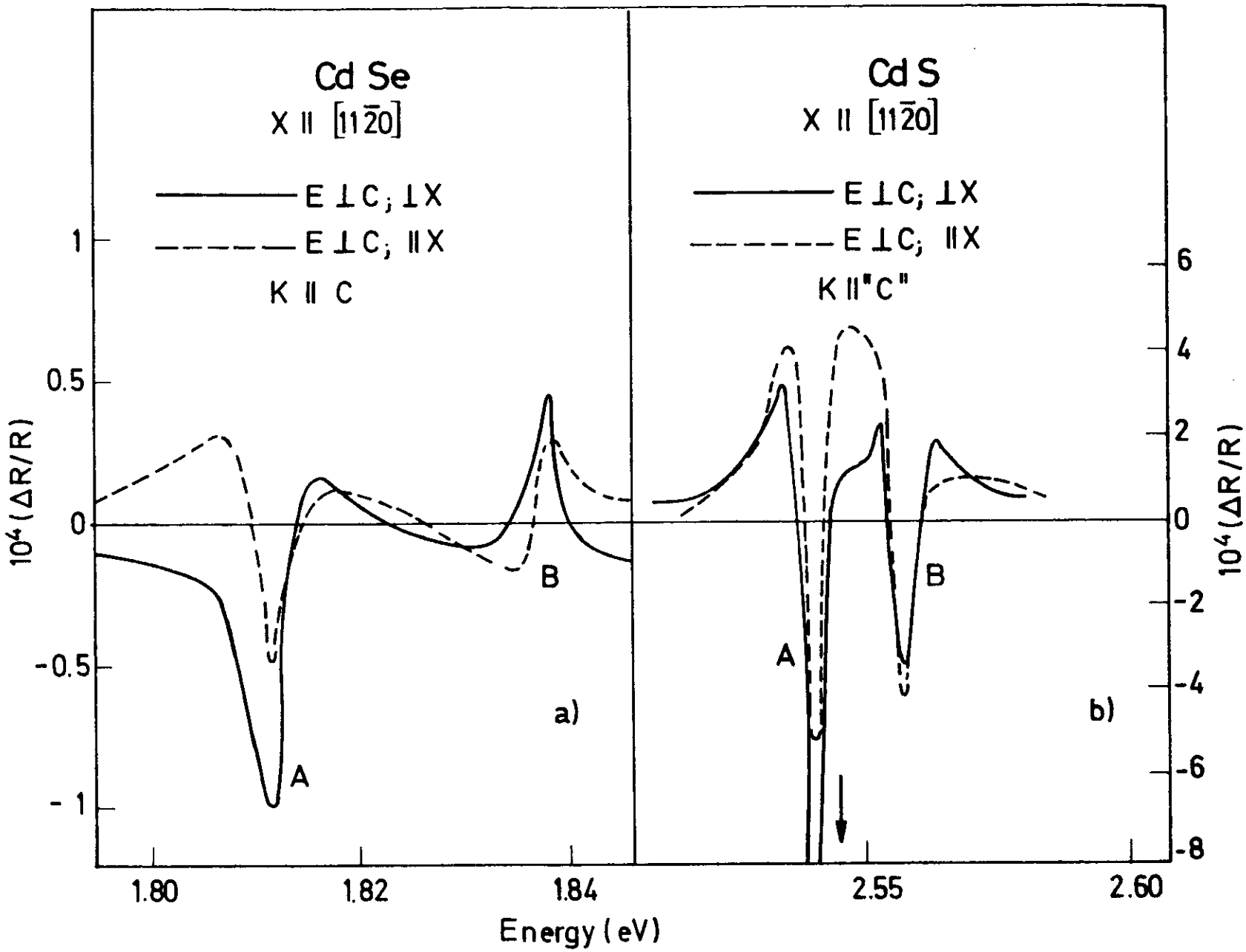
Cd Se
X ∥ [11$\bar{2}$0]
E ⊥ C ; ⊥ X
E ⊥ C ; ∥ X
K ∥ C
Cd S
X ∥ [11$\bar{2}$0]
E ⊥ C ; ⊥ X
E ⊥ C ; ∥ X
K ∥ "C"
$10^4(\Delta R/R)$
A
B
a)
b)
1.80
1.82
1.84
2.55
2.60
Energy (eV)

Figure 26

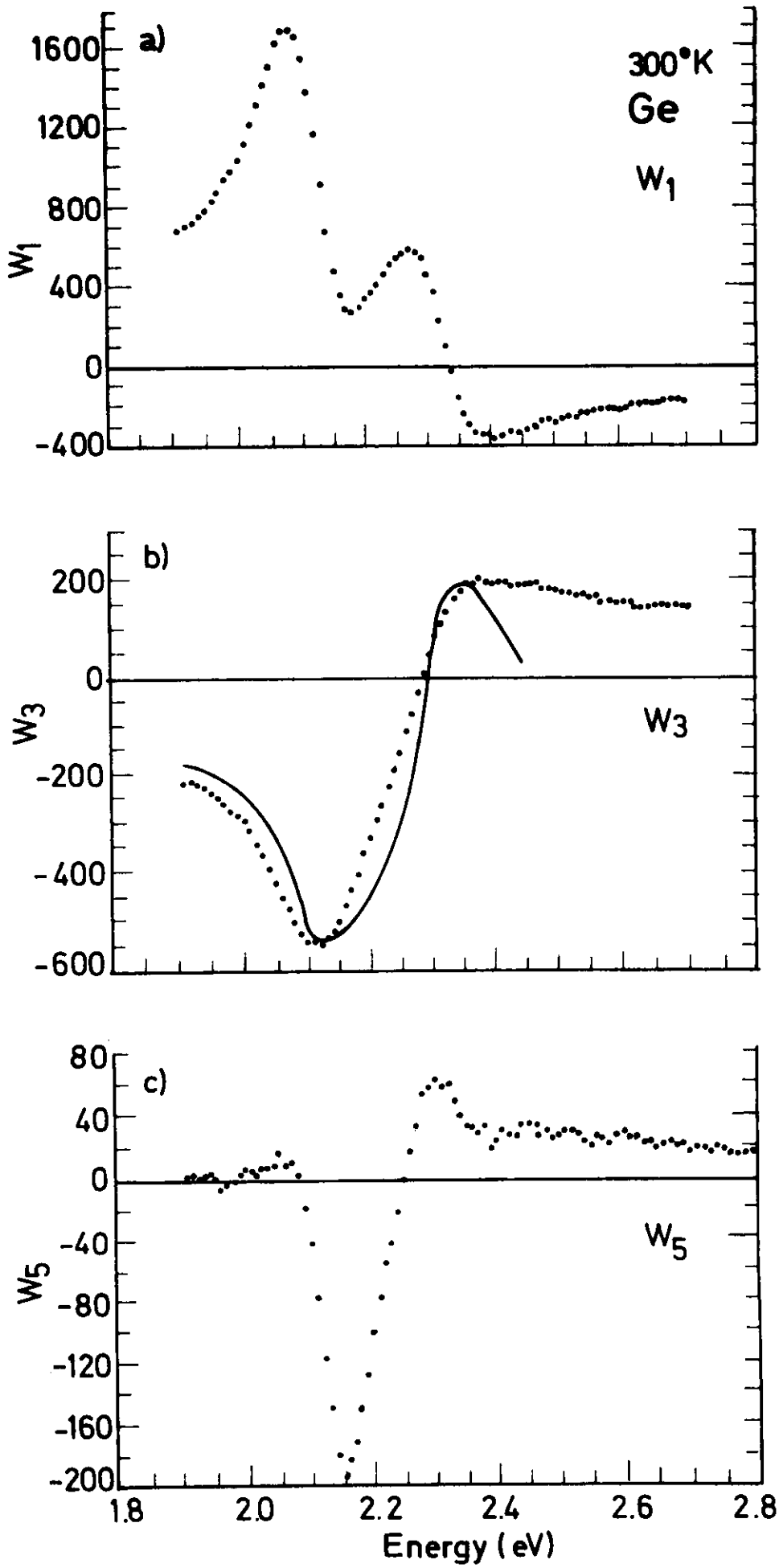
a)
300°K
Ge
W1
1600
1200
800
400
0
-400
W1
b)
W3
200
0
-200
-400
-600
W3
c)
W5
80
40
0
-40
-80
-120
-160
-200
W5
1.8
2.0
2.2
2.4
2.6
2.8
Energy (eV)

Figure 27

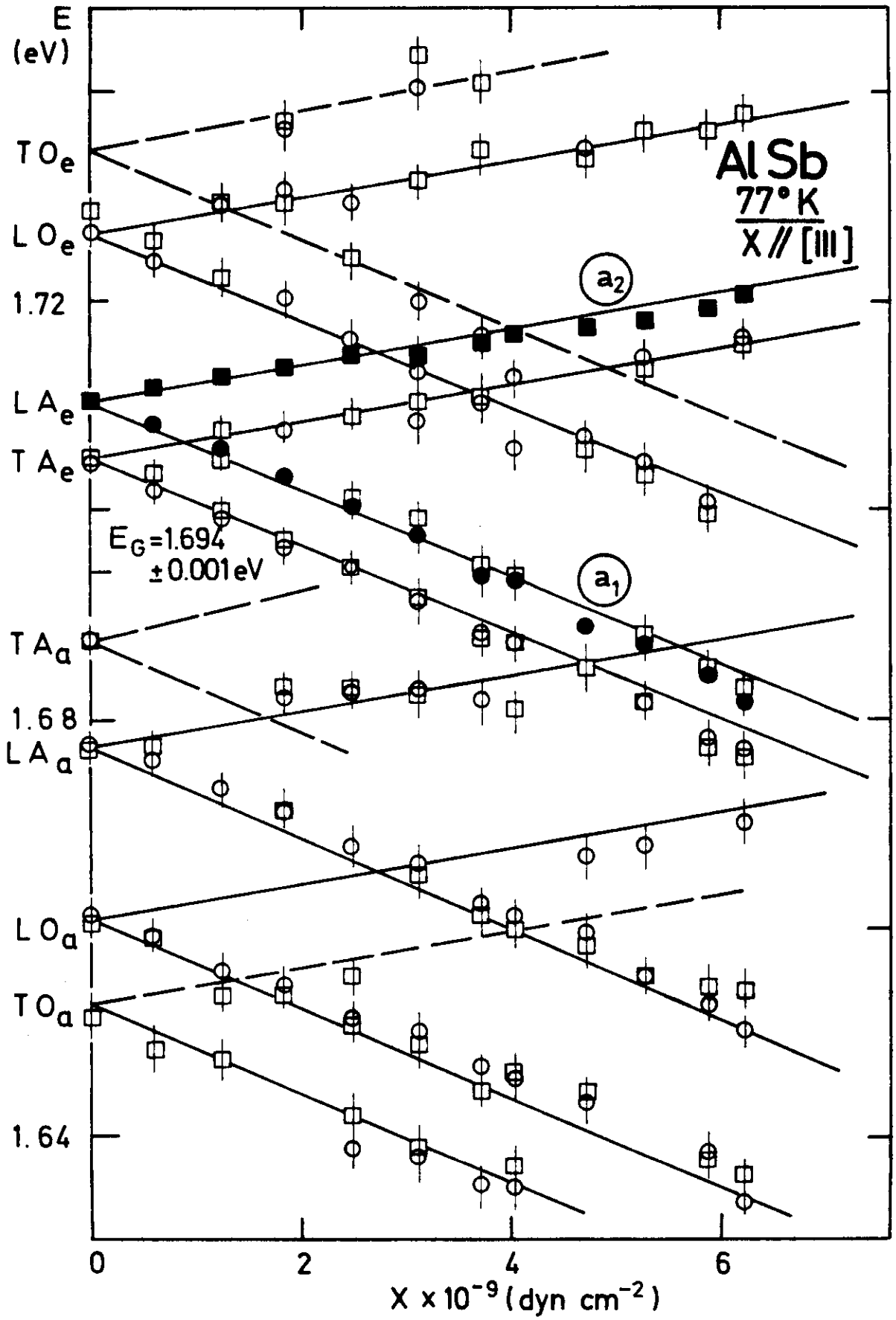
E
(eV)
TOe
LOe
1.72
LAe
TAe
EG=1.694
±0.001eV
TAa
1.68
LAa
LOa
TOa
1.64
AlSb
77°K
X // [111]
a2
a1
0
2
4
6
X x 10-9 (dyn cm-2)

Figure 28

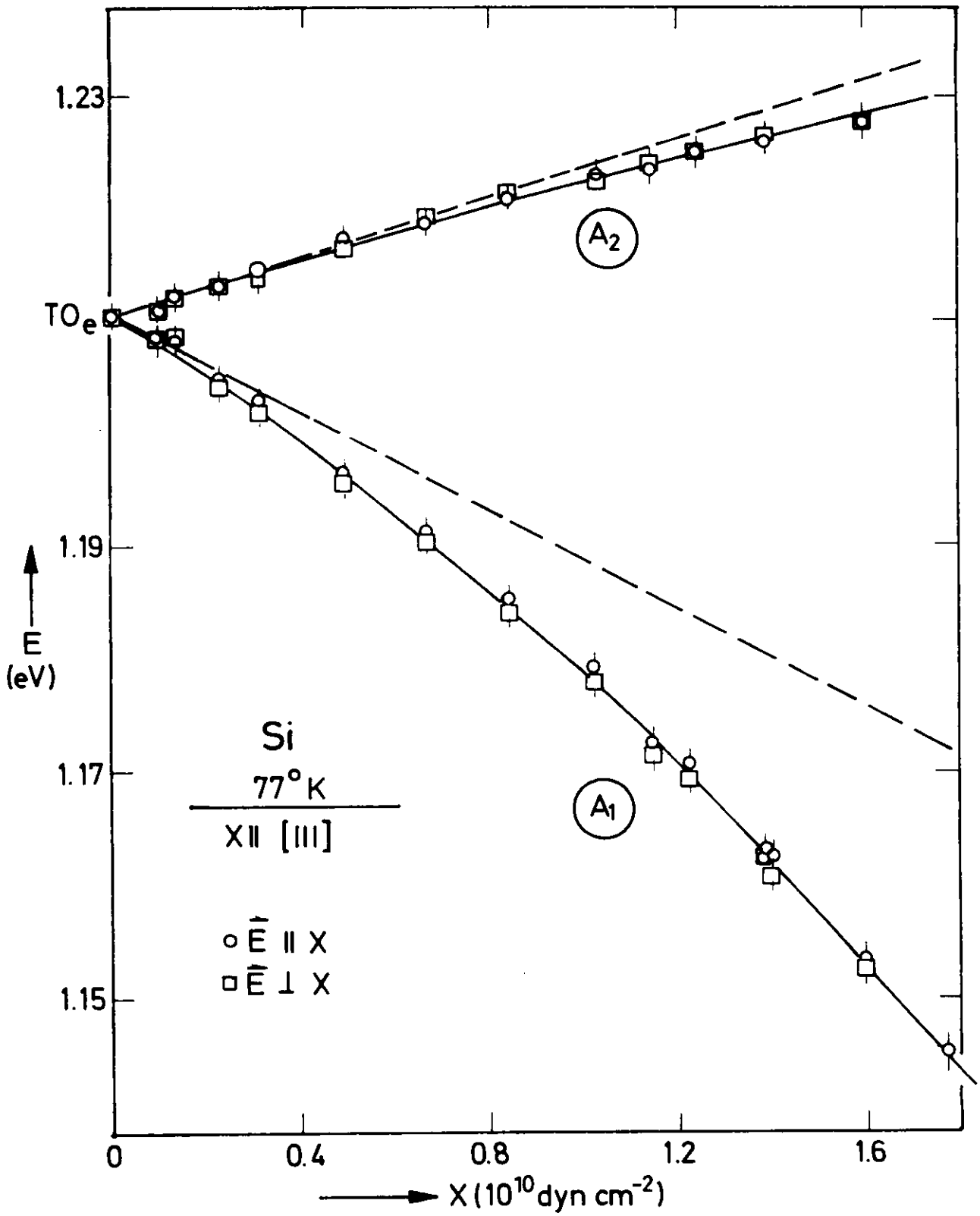
1.23
TO$_e$
1.19
1.17
1.15
E
(eV)
Si
77°K
X ∥ [111]
○ $\vec{E}$ ∥ X
□ $\vec{E}$ ⊥ X
A$_2$
A$_1$
0
0.4
0.8
1.2
1.6
X (10^{10} dyn cm^{-2})

Figure 29

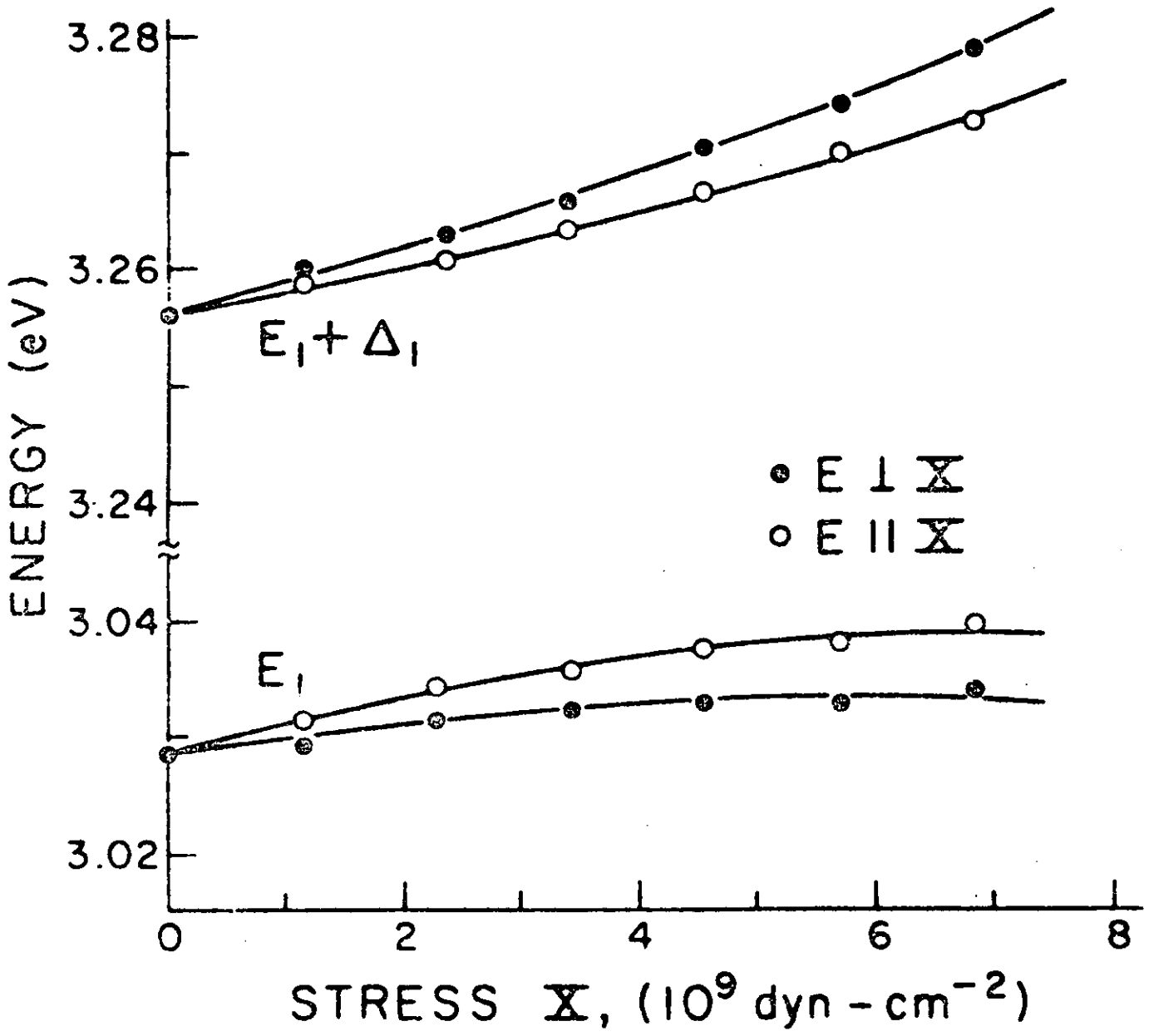
3.28
3.26
3.24
3.04
3.02
ENERGY (eV)
E1+Δ1
E1
• E ⊥ X
○ E ∥ X
0
2
4
6
8
STRESS X, (10^9 dyn - cm^-2)

Figure 30

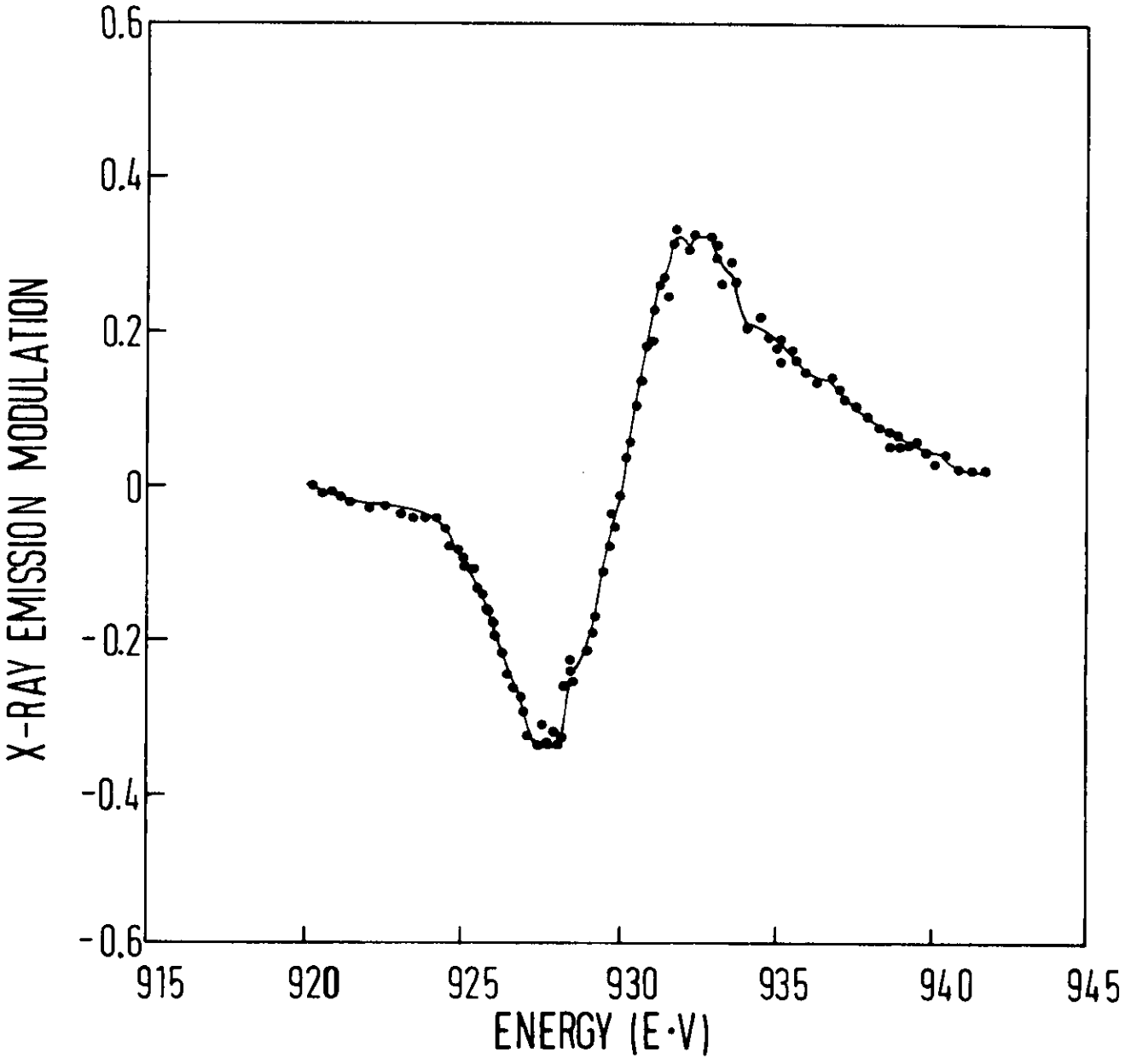
0.6
0.4
0.2
0
-0.2
-0.4
-0.6
X-RAY EMISSION MODULATION
915
920
925
930
935
940
945
ENERGY (E·V)

Figure 31

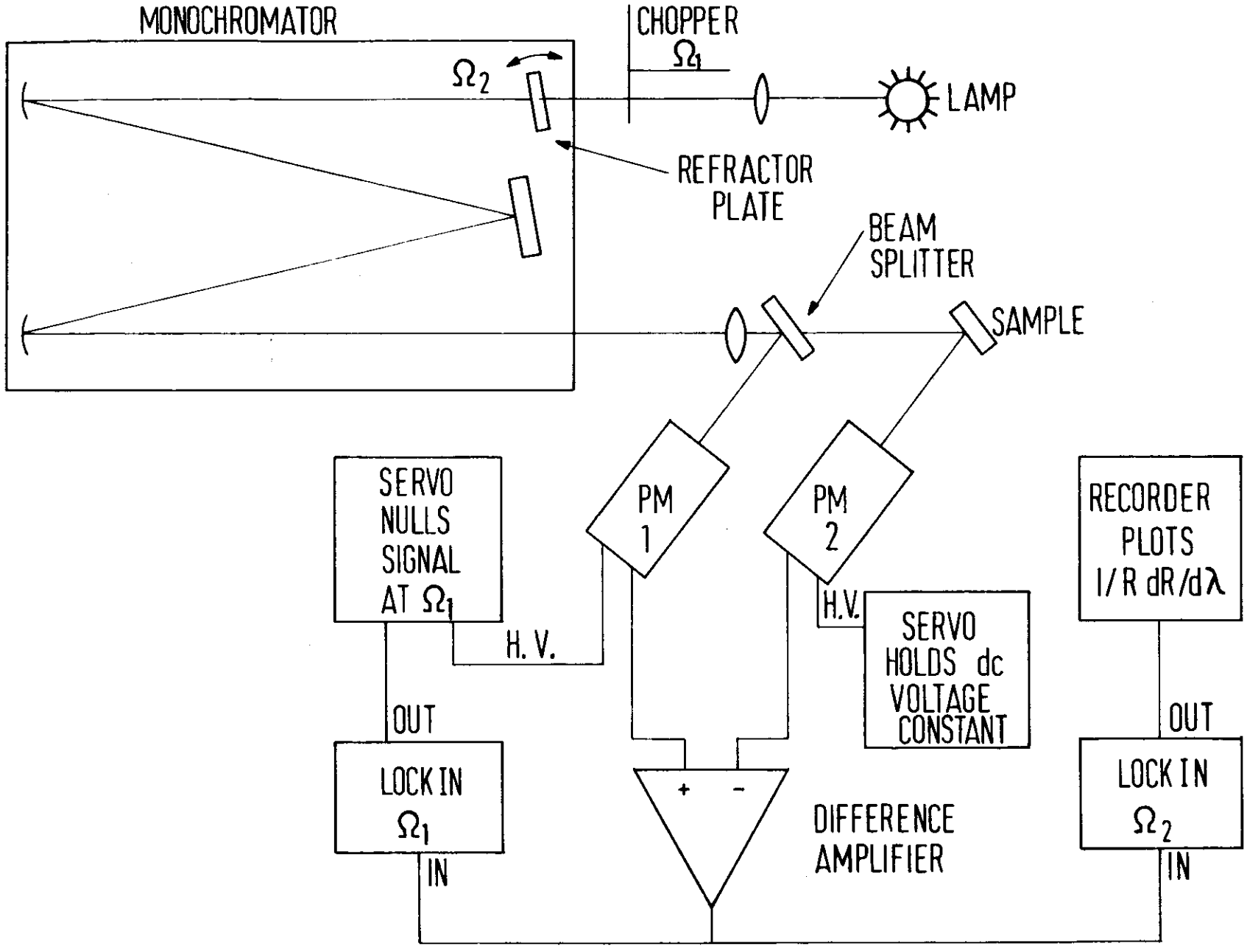
MONOCHROMATOR
CHOPPER
Ω_1
Ω_2
LAMP
REFRACTOR PLATE
BEAM SPLITTER
SAMPLE
SERVO NULLS SIGNAL AT Ω_1
PM 1
PM 2
RECORDER PLOTS I/R dR/dλ
H. V.
H.V.
SERVO HOLDS dc VOLTAGE CONSTANT
OUT
LOCK IN Ω_1
+ −
DIFFERENCE AMPLIFIER
OUT
LOCK IN Ω_2
IN
IN

Fig. 32

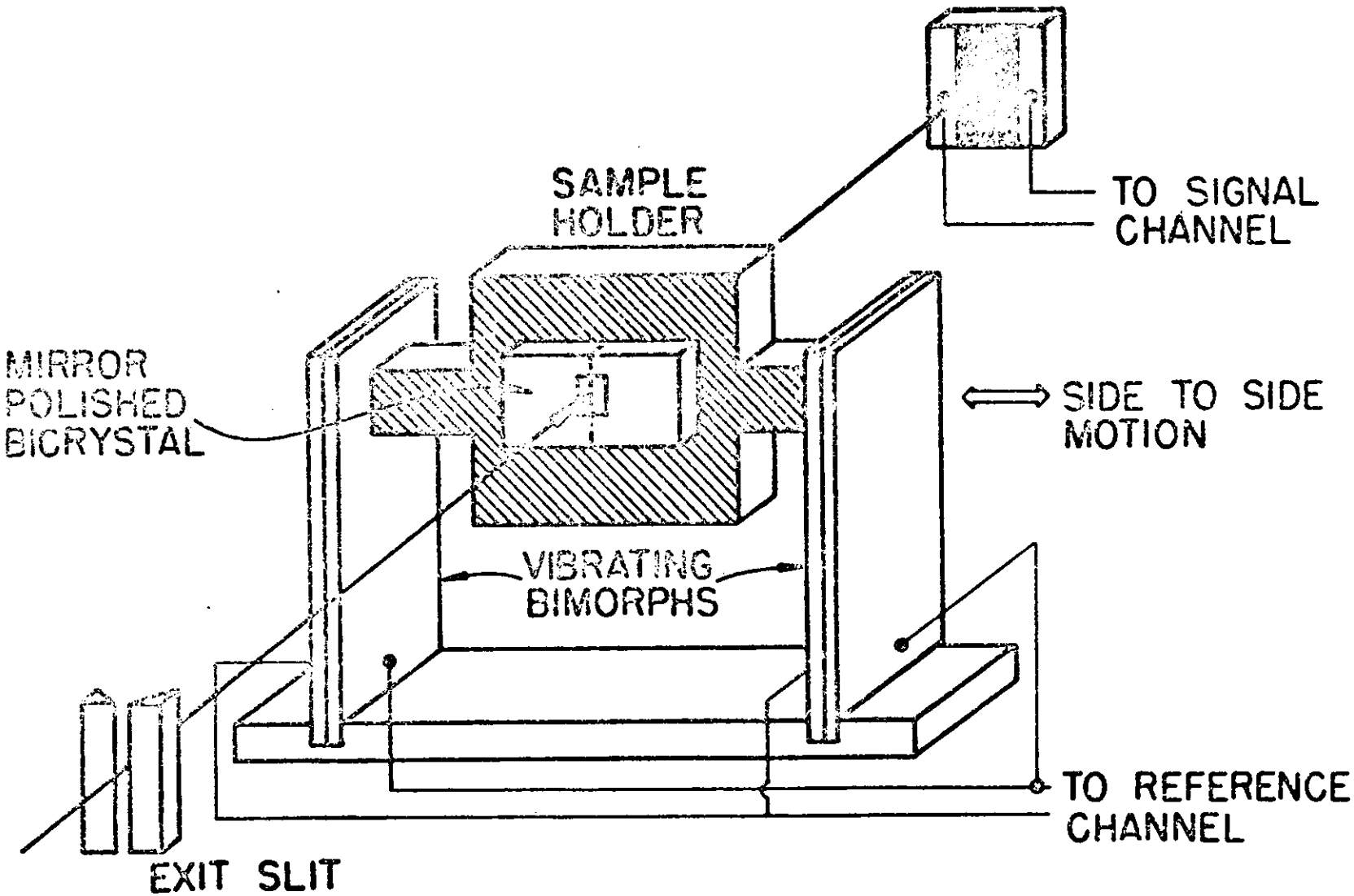
SAMPLE
HOLDER
TO SIGNAL
CHANNEL
MIRROR
POLISHED
BICRYSTAL
SIDE TO SIDE
MOTION
VIBRATING
BIMORPHS
TO REFERENCE
CHANNEL
EXIT SLIT

Figure 33

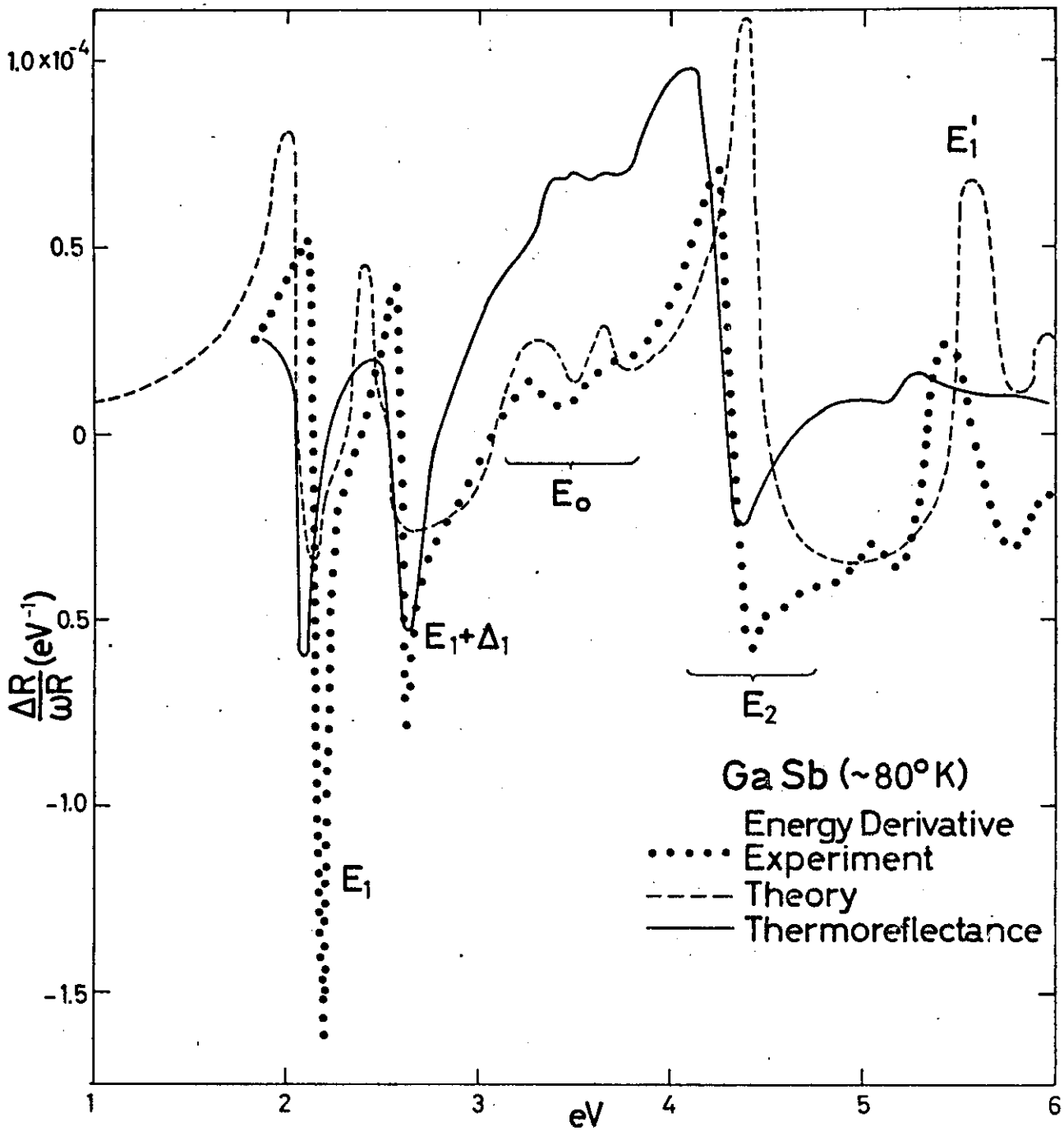
1.0x10⁻⁴
0.5
0
-0.5
-1.0
-1.5
ΔR/R (eV⁻¹)
E₁
E₁+Δ₁
E₀
E₂
E₁'
Ga Sb (~80° K)
Energy Derivative
Experiment
Theory
Thermoreflectance
1
2
3
4
5
6
eV

Figure 34

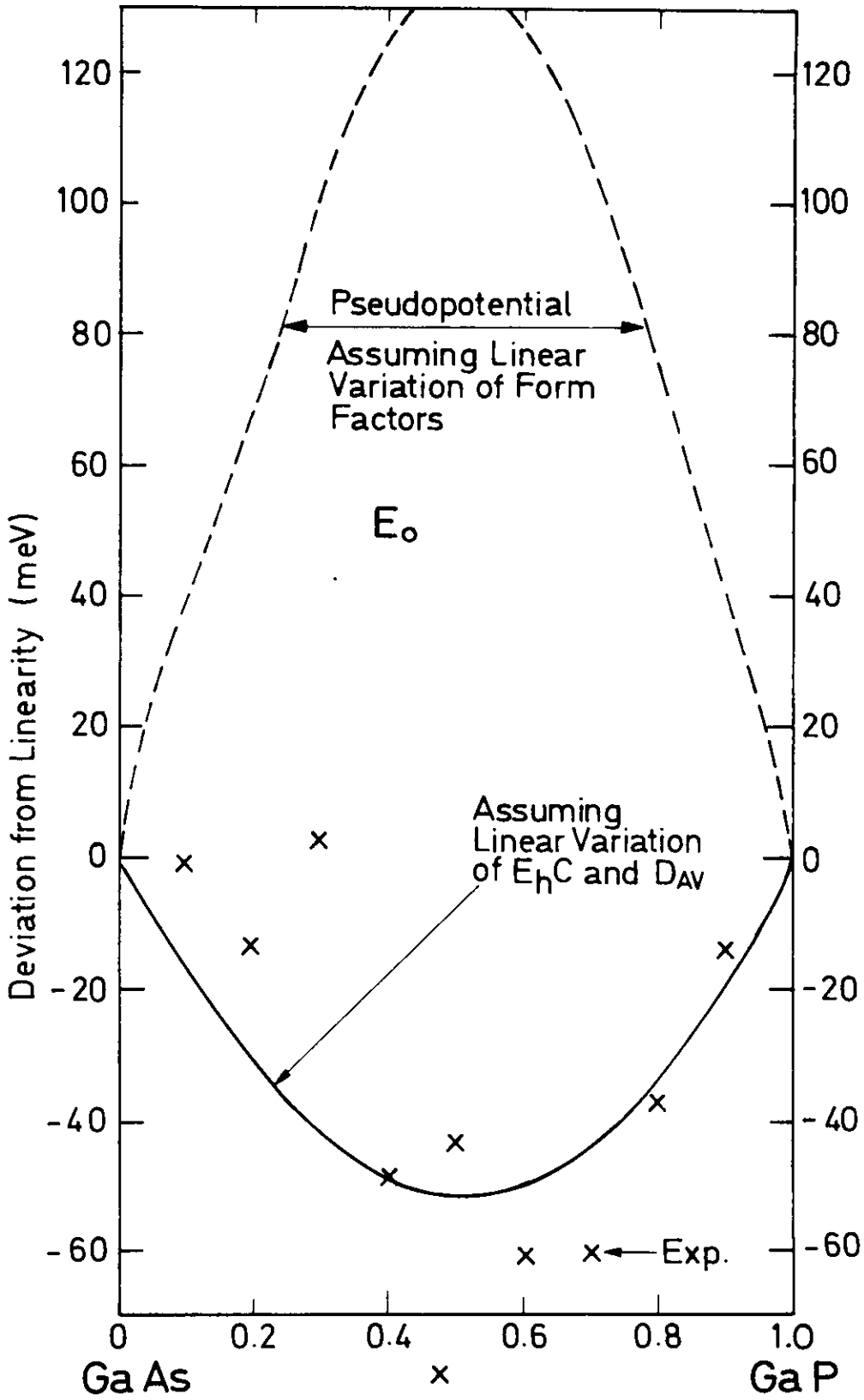
Deviation from Linearity (meV)
120
100
80
60
40
20
0
-20
-40
-60
Pseudopotential
Assuming Linear
Variation of Form
Factors
E_o
Assuming
Linear Variation
of E_hC and D_{AV}
Exp.
0
0.2
0.4
0.6
0.8
1.0
Ga As
Ga P

Figure 35